

# **Case History: Strain and Force Distribution in HDPE Reinforced Wall**

By

**DOV LESHCHINSKY  
CHRISTOPHER MEEHAN  
BARIS IMAMOGLU**

**Department of Civil and Environmental Engineering  
College of Engineering  
University of Delaware**

**July 2009**

**Delaware Center for Transportation  
University of Delaware  
355 DuPont Hall  
Newark, Delaware 19716  
(302) 831-1446**



The Delaware Center for Transportation is a university-wide multi-disciplinary research unit reporting to the Chair of the Department of Civil and Environmental Engineering, and is co-sponsored by the University of Delaware and the Delaware Department of Transportation.

### **DCT Staff**

Ardeshir Faghri  
*Director*

Jerome Lewis  
*Associate Director*

Ellen Pletz  
*Assistant to the Director*

Lawrence Klepner  
*T<sup>2</sup> Program Coordinator*

Matheu Carter  
*T<sup>2</sup> Engineer*

Sandra Wolfe  
*Senior Secretary*

### **DCT Policy Council**

Natalie Barnhart, Co-Chair  
*Chief Engineer, Delaware Department of Transportation*

Michael Chajes, Co-Chair  
*Dean, College of Engineering*

Delaware General Assembly Member  
*Chair, Senate Highways & Transportation Committee*

Delaware General Assembly Member  
*Chair, House of Representatives Transportation/Land Use & Infrastructure Committee*

Michael Gamel-McCormick  
*Dean, College of Education and Public Policy*

Harry Shenton  
*Chair, Civil and Environmental Engineering*

Ralph Reeb  
*Director of Planning, Delaware Department of Transportation*

Stephen Kingsberry  
*Director, Delaware Transit Corporation*

Shannon Marchman  
*Representative of the Director of the Delaware Development Office*

James Johnson  
*Executive Director, Delaware River & Bay Authority*

William Osborne  
*Executive Director, Transportation Management Association*

*Delaware Center for Transportation  
University of Delaware  
Newark, DE 19716  
(302) 831-1446*



## TABLE OF CONTENTS

LIST OF TABLES.....	vi
LIST OF FIGURES .....	vii
ABSTRACT .....	xiv
Chapter	
1 INTRODUCTION .....	15
2 BACKGROUND .....	17
2.1 The IRIB Project and Measured Field Data.....	17
2.1.1 Strain Gages.....	22
2.1.2 Settlement Plates .....	24
2.1.3 Piezometers .....	29
2.1.4 Inclinometers .....	31
2.1.5 Wall Targets .....	37
2.1.6 Settlement of the South Embankment .....	42
2.2 Instrumented Mechanically Stabilized Earth Walls .....	44
2.2.1 Application of Strain Gages and the Analysis of the Deformation Behavior of Geosynthetics .....	45
2.2.2 MSE Wall on I – 15 Salt Lake City Utah, USA .....	52
3 PROCEDURE TO ASSESS STRESS IN POLYMERIC REINFORCEMENT UTILIZING EXHUMED SPECIMENS .....	61
3.1 Exhumation Process at IRIB.....	61
3.2 Laboratory Measurement of Residual Strains .....	68
3.3 Simulating Field Loading History on Virgin Specimens to Establish the Relationships between Total Strain, Residual Strain & Tensile Load .....	78

3.3.1	Verification of Hypothesis Using Sacrificial Geogrid Specimens.....	80
3.3.2	Improved Sample Preparation for Creep-Relaxation Tests.....	84
3.3.3	Modified Simulation of Creep-Relaxation Tests Using Modified Samples.....	90
3.3.4	Refined Testing Approach Used to Simulate Field Loading History .....	93
4	RESULTS OF CREEP-RELAXATION TESTS.....	98
4.1	Testing Results of UX1400HS, UX1500HS & UX1600HS Geogrids.....	98
4.2	Summary of Test Results.....	110
5	INTERPRETATION OF MEASURED RESIDUAL STRAINS ON EXHUMED GEOGRIDS .....	113
5.1	Measured Residual Strains .....	113
5.1.1	Layer # 23 (UX1400HS) .....	116
5.1.2	Layer # 22 (UX1400HS) .....	118
5.1.3	Layer # 19 (UX1400HS) .....	120
5.1.4	Layer # 17 (UX1400HS) .....	122
5.1.5	Layer # 15 (UX1500HS) .....	124
5.1.6	Layer # 13 (UX1500HS) .....	126
5.1.7	Layer # 11 (UX1500HS) .....	128
5.1.8	Layer # 10 (UX1600HS) .....	130
5.1.9	Layer # 8 (UX1600HS) .....	132
5.1.10	Strain Gage Inspection.....	134
5.2	Interpretation of the Results .....	137
6	CONCLUSIONS AND RECOMMENDATIONS .....	145
6.1	Conclusions .....	146
6.2	Recommendations .....	147
	REFERENCES .....	148

## LIST OF TABLES

Table 2.1	Site Soil Strata Station 289+00 .....	18
Table 2.2	Settlement Plate Locations and Elevations (Berkheimer, 2007) .....	26
Table 2.3	Piezometer Installation Data (Berkheimer, 2007) .....	29
Table 2.4	Vertical Inclinator Installation Details (Berkheimer, 2007) .....	31
Table 2.5	Site Soil Strata (Bay et al., 2003) .....	53
Table 3.1	Aperture lengths ( $L_o$ ) of the virgin geogrids.....	78
Table 5.1	Strain gage observed condition (Layer #23).....	116
Table 5.2	Strain gage observed condition (Layer #22).....	118
Table 5.3	Strain gage observed condition (Layer #19).....	120
Table 5.4	Strain gage observed condition (Layer #17).....	122
Table 5.5	Strain gage observed condition (Layer #15).....	124
Table 5.6	Strain gage observed condition (Layer #13).....	126
Table 5.7	Strain gage observed condition (Layer #11).....	128
Table 5.8	Strain gage observed condition (Layer #10).....	130
Table 5.9	Strain gage observed condition (Layer #8).....	132
Table 5.10	Tensar structural geogrid product properties (product specification Tensar structural geogrid 2007).....	143
Table 5.11	Calculated Factor of safety on geogrid strength .....	144

## LIST OF FIGURES

Figure 2.1	Stationing and wall layout for south abutment, not scaled (Berkheimer, 2007). .....	19
Figure 2.2	Instrumentation locations at Station 289+00 (not to scale). .....	21
Figure 2.3	Instrumented geogrid layers at Wall 1 Station 289+00. ....	23
Figure 2.4	Wall 1 Station 289+00 (12/21/2007). .....	24
Figure 2.5	Settlement profile for Station 289+00 (modified after Berkheimer, 2007). .....	27
Figure 2.6	Magnitude of settlement at Station 289+00(modified after Berkheimer, 2007). .....	28
Figure 2.7	Change in pressure difference with time at Station 289+00 (modified after Berkheimer, 2007). .....	30
Figure 2.8	Inclinometer 289-55R data: 12/21/06 – 1/13/07. ....	32
Figure 2.9	Inclinometer 289-55A data: 04/19/2007 – 04/24/2008. ....	33
Figure 2.10	Inclinometer 289-75L data: 09/28/06 – 10/15/06. ....	35
Figure 2.11	Inclinometer 289-75B data: 01/02/2008 – 04/24/2008. ....	36
Figure 2.12	Wall target placement at Wall 1 Station 289+00 (not to scale). .....	38
Figure 2.13	Vertical movement versus time Wall 1 Station 289+00 (modified after Berkheimer, 2007). .....	40
Figure 2.14	Horizontal movement versus time Wall 1 Station 289+00 (modified after Berkheimer, 2007). .....	41
Figure 2.15	Horizontal movement rates versus time Wall 1 Station 289+00 (modified after Berkheimer, 2007). .....	42
Figure 2.16	Influence zone South Embankment Station 293+00– 12/21/2007. ....	43

Figure 2.17	Influence zone South Embankment Station 293+00- 05/28/2008.....	43
Figure 2.18	Influence zone South Embankment Station 293+00- 06/27/2008.....	44
Figure 2.19	Geogrid deformation on the GRS wall (Won & Kim 2006). .....	47
Figure 2.20	Nonwoven geotextile deformation on the GRS wall (Won & Kim 2006).....	47
Figure 2.21	Woven geotextile deformation on the GRS wall (Won & Kim 2006).....	48
Figure 2.22	Geosynthetics Deformation in Section I (Won & Kim, 2006). .....	50
Figure 2.23	Geosynthetics Deformation in Section II (Won & Kim, 2006). .....	51
Figure 2.24	Elevation View of Wall Section with Instrumented Primary Reinforcement (Bay et al., 2003).....	55
Figure 2.25	Elevation View of Wall Section with Instrumented Primary and Intermediate Reinforcement (Bay et al., 2003) .....	57
Figure 2.26	Measured Bar Forces for Primary Reinforcement Only Layer 2 (Bay et al., 2003). .....	58
Figure 2.27	Tension Distribution in Bar Mats in the Primary and Intermediate Reinforced Wall Section (Bay et al., 2003).....	59
Figure 3.1	Removal process of backfill (5/23/2008). .....	62
Figure 3.2	Removal process often damaged the embedded geogrids, mainly at locations different than Wall 1, Station 289+00 (6/2/2008).....	63
Figure 3.3	Exposed geogrids, some damaged, and backfill loaded into a truck (6/2/2008). .....	63
Figure 3.4	Collection of recovered (not at Wall 1, Station 289+00) geogrid for recycling (5/23/2008).....	64
Figure 3.5	Mechanical removal of approximately 0.38 m (15 inches) sand cover below the previous geogrid layer (5/28/2008). .....	65
Figure 3.6	Manual removal of the remaining 0.06 m (3 inches) of soil cover (5/28/2008). .....	66

Figure 3.7	Careful recovery of exhumed geogrid (5/28/2008).	66
Figure 3.8	Labeling a recovered strain gage instrumented geogrid panel (5/28/2008).	67
Figure 3.9	View of site after the removal of the south embankment (6/27/2008).	67
Figure 3.10	View of site after the removal of the south embankment (6/27/2008).	68
Figure 3.11	Recovered geogrid placed flat on concrete floor to measure the post-construction aperture sizes (5/25/2008).	69
Figure 3.12	Geogrid panel is stretched by hanging it from a series of steel hooks (7/7/2008).	71
Figure 3.13	Application of a 0.41 kN/m (28 lb/ft) force via a wooden beam and hooks (7/7/2008).	71
Figure 3.14	General view of stretching process with the wooden beams (7/7/2008).	72
Figure 3.15	The geogrid held and stretched by clamping its top between the wooden beam and the steel girder (7/10/2008).	73
Figure 3.16	Modified system to apply load to the panel (7/10/2008).	73
Figure 3.17	Iron bar threaded through the geogrid apertures used to hang the geogrid at the top (7/11/2008).	74
Figure 3.18	Iron bar threaded through the geogrid apertures to apply load (7/11/2008).	74
Figure 3.19	Flexible cable attaching the geogrid panel to a fixed iron bar (7/17/2008).	75
Figure 3.20	Flexible cable attaching the geogrid panel to an iron bar having attached hanging weights (7/17/2008).	76
Figure 3.21	Overview of flexible cable attachment of the geogrid panel (7/17/2008).	76
Figure 3.22	Tested sample after quick loading, during relaxation	81

Figure 3.23	Loading frame and clamped sample.....	82
Figure 3.24	Results of Test A & Test B attempting to simulate relaxation after inducing a history of rapid loading and unloading. ....	83
Figure 3.25	Geogrid sample and perforated sheet metals plates before gluing. ....	85
Figure 3.26	The geogrid sample and the sheet metal plates sanded and cleaned before gluing.....	85
Figure 3.27	Nearly all the parts of the clamps are in place before placing epoxy. ....	86
Figure 3.28	The glued specimen clamped with epoxy and screws.....	86
Figure 3.29	Fixture to connect the sheet metal clamp to the loading frame.....	87
Figure 3.30	The bottom part of the clamping fixture connected to the loading frame.....	88
Figure 3.31	Sample during loading – note that outer geogrids have been cut. ....	88
Figure 3.32	Post-test examination of the clamping fixture to verify whether slippage occurred.....	89
Figure 3.33	Tests attempting to establish the relationship between total strain, residual strain and load.....	92
Figure 3.34	Loaded and unloaded samples for creep and relaxation tests.....	95
Figure 3.35	Loaded specimen (note the gap between the two parts of the cut strands; it signify the elongation of the specimen after being subjected to load).....	96
Figure 3.36	Measurement of length using a digital caliper. ....	97
Figure 4.1	Total strain due to various sustained load increments (UX1400HS). ....	99
Figure 4.2	Total strain due to various sustained load increments (UX1500HS). ....	100
Figure 4.3	Total strain due to various sustained load increments (UX1600HS). ....	100

Figure 4.4	Residual strain developments during relaxation (UX1400HS).....	101
Figure 4.5	Residual strain developments during relaxation (UX1500HS).....	102
Figure 4.6	Residual strain developments during relaxation (UX1600HS).....	102
Figure 4.7	Sustained force versus total strain and residual strain after relaxation (UX1400HS). .....	104
Figure 4.8	Sustained force versus total strain and residual strain after relaxation (UX1500HS). .....	104
Figure 4.9	Sustained force versus total strain and residual strain after relaxation (UX1600HS). .....	105
Figure 4.10	Curve-fitted second order polynomial relating the measured residual strain to the in situ geogrid total strain (UX1400HS).....	106
Figure 4.11	Curve-fitted second order polynomial relating the measured residual strain to the in situ geogrid total strain (UX1500HS).....	107
Figure 4.12	Curve-fitted third order polynomial relating the measured residual strain to the insitu geogrid total strain (UX1600HS). .....	107
Figure 4.13	Load versus total strain (UX1400HS).....	109
Figure 4.14	Load versus total strain (UX1500HS).....	109
Figure 4.15	Load versus total strain (UX1600HS).....	110
Figure 4.16	Summary chart of total strain versus residual strain. ....	111
Figure 4.17	Summary chart of load versus total strain. ....	112
Figure 5.1	Strain distribution of the exhumed geogrid (Layer #23). .....	116
Figure 5.2	Field strain gage measurements from the installation date to the removal date (end of construction coincides with installation of this final layer 12/01/2006) (modified after Berkheimer, 2007) (Layer #23). .....	117
Figure 5.3	Tensile force distribution based on total strain values (Layer #23).....	117
Figure 5.4	Strain distribution of the exhumed geogrid (Layer #22). .....	118

Figure 5.5	Field strain gage measurements from the installation date to the removal date (modified after Berkheimer, 2007) (Layer #22). .....	119
Figure 5.6	Tensile force distribution based on total strain values (Layer #22).....	119
Figure 5.7	Strain distribution of the exhumed geogrid (Layer #19). .....	120
Figure 5.8	Field strain gage measurements from the installation date to the removal date (modified after Berkheimer, 2007) (Layer #19). .....	121
Figure 5.9	Tensile force distribution based on total strain values (Layer #19).....	121
Figure 5.10	Strain distribution of the exhumed geogrid (Layer #17). .....	122
Figure 5.11	Field strain gage measurements from the installation date to the removal date (modified after Berkheimer, 2007) (Layer #17). .....	123
Figure 5.12	Tensile force distribution based on total strain values (Layer #17).....	123
Figure 5.13	Strain distribution of the exhumed geogrid (Layer #15). .....	124
Figure 5.14	Field strain gage measurements from the installation date to the removal date (modified after Berkheimer, 2007) (Layer #15). .....	125
Figure 5.15	Tensile force distribution based on total strain values (Layer #15).....	125
Figure 5.16	Strain distribution of the exhumed geogrid (Layer #13). .....	126
Figure 5.17	Field strain gage measurements from the installation date to the removal date (modified after Berkheimer, 2007) (Layer #13). .....	127
Figure 5.18	Tensile force distribution based on total strain values (Layer #13).....	127
Figure 5.19	Strain distribution of the exhumed geogrid (Layer #11). .....	128
Figure 5.20	Field strain gage measurements from the installation date to the removal date (modified after Berkheimer, 2007) (Layer #11). .....	129
Figure 5.21	Tensile force distribution based on total strain values (Layer #11).....	129
Figure 5.22	Strain distribution of the exhumed geogrid (Layer #10). .....	130
Figure 5.23	Field strain gage measurements from the installation date to the removal date (modified after Berkheimer, 2007) (Layer #10). .....	131

Figure 5.24	Tensile force distribution based on total strain values (Layer #10).....	131
Figure 5.25	Strain distribution of the exhumed geogrid (Layer #8). .....	132
Figure 5.26	Field strain gage measurements from the installation date to the removal date (modified after Berkheimer, 2007) (Layer #8). .....	133
Figure 5.27	Tensile force distribution based on total strain values (Layer #8).....	133
Figure 5.28	Poorly-bonded strain gage completely debonded from the geogrid (layer #8, gage #3). .....	135
Figure 5.29	Well-bonded strain gages (layer #10, gage #2). .....	136
Figure 5.30	Cable connection failure (layer #15, gage #2). .....	136
Figure 5.31	Back-calculated total strain distributions on the instrumented geogrid layers. .....	138
Figure 5.32	Tensile force distributions of the instrumented geogrid layers. ....	139
Figure 5.33	Measured normalized $T_{\max}$ for each layer. ....	141
Figure 5.34	Distribution of the measured data and the approximated linear distribution. ....	142

## **ABSTRACT**

Geogrid reinforced mechanically stabilized earth (MSE) walls have been constructed to support new bridge approach embankments at the Indian River Inlet in Sussex County, Delaware. A large magnitude of settlement was expected since these embankments were constructed over poor foundation soil, a layer of soft clay about 16 m (52 ft) thick. Therefore, the embankments were monitored with settlement plates, piezometers, inclinometers and wall targets. Along with this instrumentation, at the south abutment MSE Wall 1 Station 289+00 was instrumented with strain gages. The use of strain gages was necessary to verify that the geogrid reinforcement was not overstressed, as MSE wall design does not account for large foundation settlement.

Fifteen months after the completion of construction, due to significantly higher settlements than expected, it was decided to remove the embankments. Presented are the assessments of strain and force distribution of the strain gage instrumented section of the MSE Wall, which were determined using laboratory tests conducted on both the exhumed and the virgin geogrids. Residual strain values were determined by length measurements of the exhumed geogrids. Then, calibration relationships between residual strains and field strains were developed using creep relaxation tests conducted on virgin geogrid specimens. These calibration relationships allowed residual strain values to be converted into the total strain and force values which were applied in the field before deconstruction of the embankment.

## **Chapter 1**

### **INTRODUCTION**

The Delaware Department of Transportation (DelDOT) planned to replace the existing bridge along Delaware Route 1 over the Indian River Inlet in Sussex County, Delaware. The construction of two new approach embankments was necessary for the new bridge, and the associated embankment fill for each abutment was planned to be contained on each side by geogrid reinforced mechanically stabilized earth (MSE) walls. The embankments were constructed on poor foundation soils consisting of a 16 m (52 ft) thick normally consolidated clay layer, which was located approximately 17.5 m (58 ft) below the top of the embankment. It was anticipated that the construction of the approach embankments over this soft clay layer would result in large settlements. Therefore, to monitor the embankment performance during and after construction, an extensive geotechnical instrumentation program was utilized at the site, comprised of inclinometers, settlement plates, piezometers and wall targets. In addition, MSE Wall 1 at Station 289+00 was instrumented with strain gages to verify that the geogrid reinforcement was not overstressed at this location.

Construction at Station 289+00 began on 02/20/2006 and was completed on 12/01/2006. Due to significantly higher settlements than expected, the embankments were removed. The deconstruction process started on 04/20/2008 and was completed in three months. This removal created the opportunity to exhume specimens of geogrid reinforcement, particularly those with strain gages attached. These specimens could then be examined in the lab to assess their residual or plastic

strain. Techniques for proper interpretation of plastic strain were developed as part of this study to infer the load induced in the geogrids while in-service. The exhumation also provided an opportunity for unobstructed examination of the strain gages glued to the geogrids. These observations provided an explanation for the relatively poor strain gage performance that was observed at the site, without a need for speculation.

The length changes of the exhumed geogrids were measured and converted to the corresponding strain values. These strains are the residual strains, as measured after relaxation. A test method which simulates field conditions was developed to enable correlation between the measured residual strains on exhumed specimens with the in-situ total strains and loads. Using correlation charts, the residual strain values were converted to strain and load values existing in the various geogrid layers while in-service.

It was found that the maximum in-situ strain in the various layers of geogrids ranged from 3% to 5%. Maximum strains in the various layers were approximately uniform with height. The maximum force in the geogrid was about 1.3 to 1.6 times smaller than the long-term strength of the geogrid. Most of the strain gages were debonded, each to a different degree, thus providing an explanation as to why these gages generally produced lower strains than those assessed after exhumation.

## **Chapter 2**

### **BACKGROUND**

#### **2.1 The IRIB Project and Measured Field Data**

Geogrid reinforced mechanically stabilized earth (MSE) walls were constructed to support new bridge approach embankments at the Indian River Inlet in Sussex County, Delaware. The embankment fill was supported on each side by geogrid reinforced mechanically stabilized earth (MSE) walls. The fill material used in the IRIB project was classified as A-1-b ( $C_u=3.6$  and  $C_c=1.07$ ) according to AASHTO soil classification standards and was a poorly graded medium to coarse sand according to the ASTM D2487-06 standard. The embankments were constructed on poor foundation soils. Table 2.1 presents the site soil strata as of May 2007 (the embankment construction was finalized on 12/01/2006) in the instrumented section, at the south embankment at Station 289+00. A 16 m (52 ft) thick normally consolidated clay layer was located approximately 17.5 m (58 ft) below the top of the embankment. It was anticipated that the construction of the large approach embankments over this soft clay layer would result in a large amount of settlement. Therefore, the embankments were instrumented with settlement plates, piezometers, inclinometers and wall targets to monitor the behavior of the embankments during and after construction. Along with this instrumentation, at the south abutment, the geogrid reinforcement in a 10.5 m (34.5 ft) high section of MSE wall 1 at station 289+00 was instrumented with strain gages. The use of strain gages was necessary to verify that

the geogrid reinforcement was not overstressed, as MSE wall design does not account for large foundation settlement (Berkheimer, 2007).

**Table 2.1 Site Soil Strata Station 289+00**

Stratum	Material Description	Approximate Depth, m (ft)
I	Embankment Fill: Medium dense brown fine to coarse SAND	Top of Embankment to 8 m (Top of Embankment to 26 ft)
II	Loose to medium dense light grey fine to medium SAND with traces of organic matter	8 m to 17.5 m (26 ft to 58 ft)
III	Soft grey slightly sandy CLAY	17.5 m to 21 m (58 ft to 68 ft)
IV	Medium stiff dark grey CLAY	21 m to 33.5 m (68 ft to 110 ft)
V	Medium to dense SAND	33.5 m to 47.5 m (110 ft to 156 ft)
VI	Medium stiff dark grey/blue sandy CLAY	47.5 m to 52 m (156 ft to 170 ft)
VII	Medium to dense SAND	52 m to 53.5 m (170 ft to 175 ft)

Strain gages were installed on geogrid panels and monitored by Scott A. Berkheimer (2007) at the Indian River Inlet site south abutment, mechanically stabilized earth (MSE) Wall 1. The gages were monitored by Berkheimer through 04/28/2007; after his graduation, the Author continued this monitoring through removal of the embankment (04/28/2007- 04/10/2008). Construction at Station 289+00 was started on 02/20/2006 and it was completed on 12/01/2006. Due to significantly higher settlements than expected, it was decided to remove the embankments. The deconstruction process started on 04/20/2008 and was completed

in three months. Figure 2.1 shows the stations for the south abutment, as well as the MSE walls that were planned to support the approach slab and the abutment of the new Indian River Inlet Bridge.

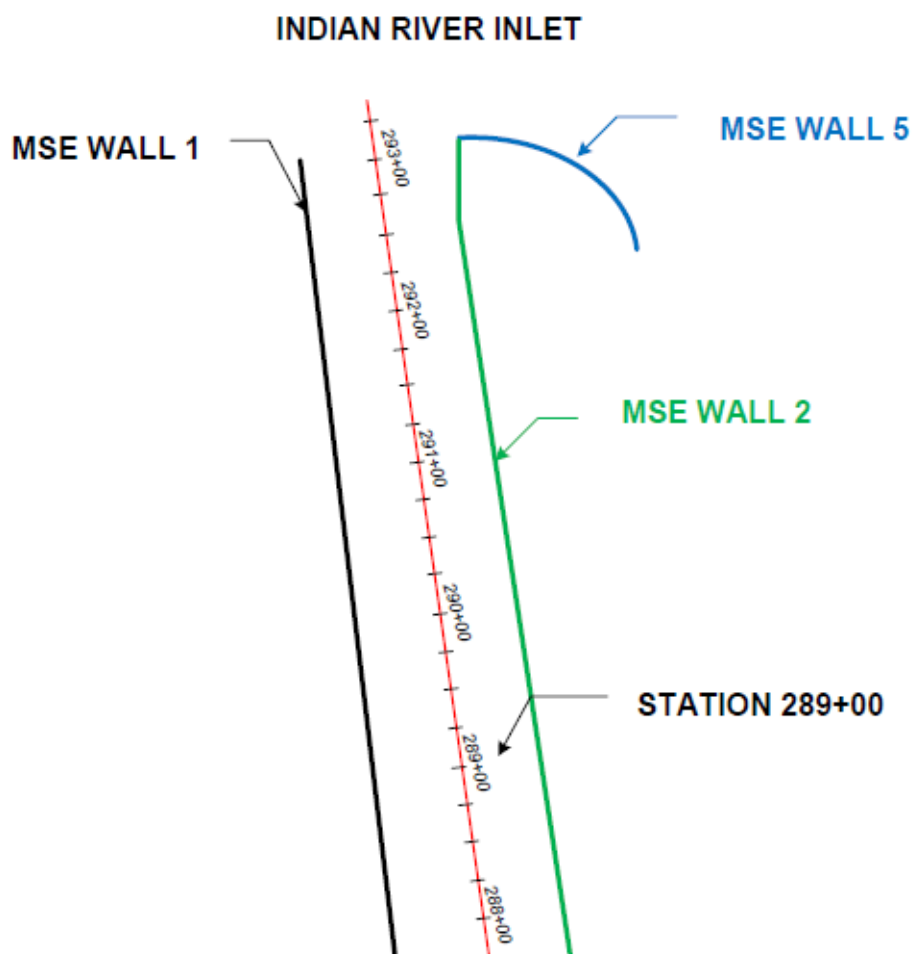


**Figure 2.1** Stationing and wall layout for south abutment, not to scale (Berkheimer, 2007).

Wall 1 at station 289+00 had been monitored with settlement plates, piezometers, inclinometers and wall targets until deconstruction of the embankment. The Delaware Department of Transportation (DelDOT) was responsible for this monitoring. DelDOT collected data, and shared it with the University of Delaware to compliment the data obtained by the monitored strain gages. Figure 2.2 represents the instrumentation locations at station 289+00.

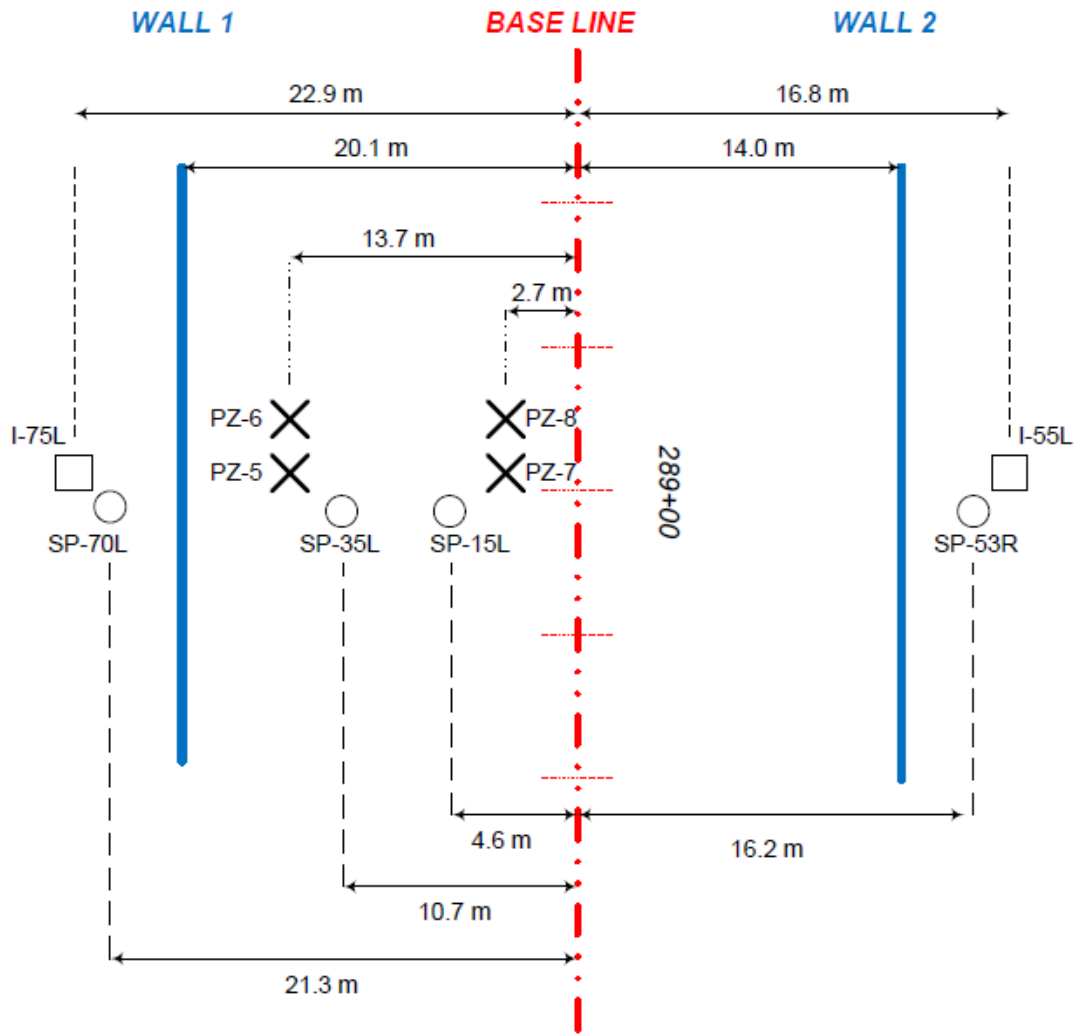


**Figure 2.2 Instrumentation locations at Station 289+00 (not to scale).**

### **2.1.1 Strain Gages**

Starting from the front end of each (1.33 m X 6.71 m (4.36 ft X 22.00 ft)) geogrid panel, five strain gages were installed by Berkheimer (2007) on 13 of the 23 geogrid layers that were used to construct Wall 1 at Station 289+00. On each panel, the first strain gage was installed at 0.46 m (1.5 ft) from the face and the rest were placed at 1.37 m (4.5 ft) intervals, which correspond to total distances from the front of 1.83 m (6 ft), 3.20 m (10.5 ft), 4.57 m (15 ft) and 5.94 m (19.5 ft), respectively. All five gages were installed in the center of each geogrid panel.

After gage installation, the instrumented geogrid panels were transported from the University of Delaware in Newark to the Indian River Inlet construction site to be installed. Geogrid layers were vertically placed every eighteen inches in the mechanically stabilized earth wall, starting at the base of the wall (elevation zero). The cross-section of the reinforced wall at station 289+00 and instrumented panels are shown in Figure 2.3. Figure 2.4 presents the view of the face of the wall at the strain gage instrumented station for Wall 1 at Station 289+00, before deconstruction of the embankment. The contractor installed the instrumented geogrid panels in the same manner as the non-instrumented panels. During installation of the instrumented panels, the strain gages were protected by small sand bags which were placed directly above the gages to protect them during and after placement of the fill material.

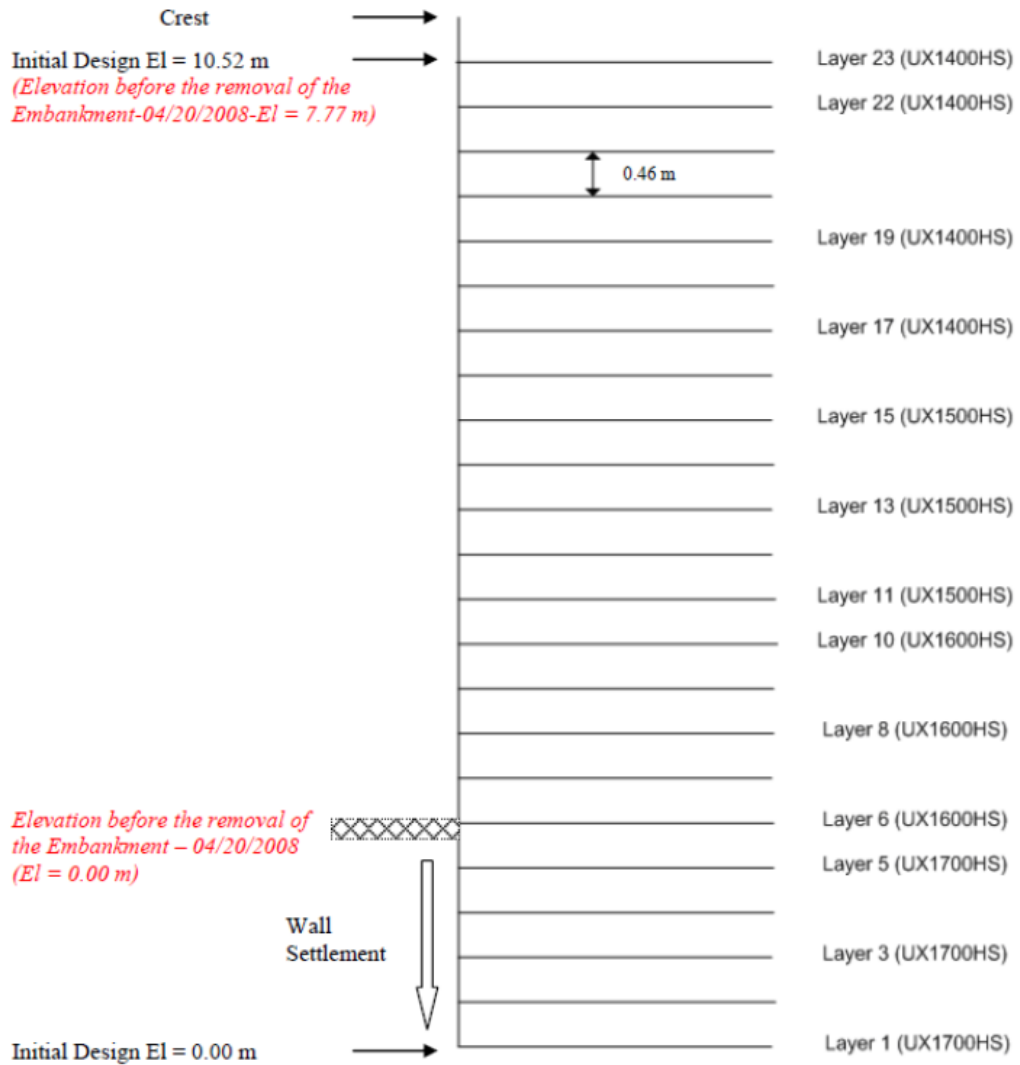


**Figure 2.3 Instrumented geogrid layers at Wall 1 Station 289+00.**



**Figure 2.4 Wall 1 Station 289+00 (12/21/2007)**

Due to the weight of the soil overburden and the associated large settlements the wall was undergoing, the geogrid deformed. Thus, the bonded strain gages deformed as well. This deformation caused changes in measured gage resistance. These changes in resistance over time were monitored using an ohmmeter, and were later converted to tensile strain and tensile load based on calibration tests conducted by Berkheimer (2007). Measured data is provided in more detail in Chapter 5.

### **2.1.2 Settlement Plates**

The contractor was responsible for the fabrication, installation, protection, and maintenance of settlement plates used in this project. The system of settlement

plates was designed to enable the engineer to observe and determine the magnitude and rate of embankment settlement. A stiff 1.22 m (4 ft)-square steel plate was set at the top of natural ground and extended upward with steel pipe lengths. The elevation change (i.e., due to the construction of the embankment) of the plate was tracked and was assumed to be equal to the settlement of the underlying ground. It was important to ensure that the riser pipes were plumb and the settlement plates and the steel pipe lengths were protected against disturbance. The steel pipe lengths were protected by an outer pipe which was held in place by the soil. Approximately 1.22 m (4 ft) 4 feet long sections of steel pipe lengths and the outer cover pipe were added for taking continuous readings as the height of the embankment increased. The change in elevation of each steel riser pipe was monitored by the surveyor.

Four settlement plates were installed at different offsets at Station 289+00. The initial reading for three of these settlement plates was taken on March 1, 2006. For settlement plate 289-53R, the initial reading was not taken until May 16, 2006. The locations of the settlement plates can be seen in Figure 2.2, denoted by circles. Table 2.2 shows the offsets and elevations of the settlement plates.

**Table 2.2 Settlement Plate Locations and Elevations (Berkheimer, 2007)**

Plate Number	Location	Distance from Wall Face (m)	Original Ground Elevation (m)	Original Plate Elevation (m)
289-15L	In Embankment	15.54	1.22	0.52
289-35L	In Embankment	9.45	1.07	0.45
289-53R	Outside Embankment	36.27	3.12	2.46
289-70L	Outside Embankment	1.22	0.46	-0.06

DelDOT obtained and recorded all measurements and elevations necessary for accurate determinations of settlement data during and after the construction of the embankment. Figure 2.5 represents the settlement profile of station 289+00. It must be noted that the settlement plate 289-53R present smaller settlement than the actual one, since the data for this plate was recorded with a delay of 10 weeks.

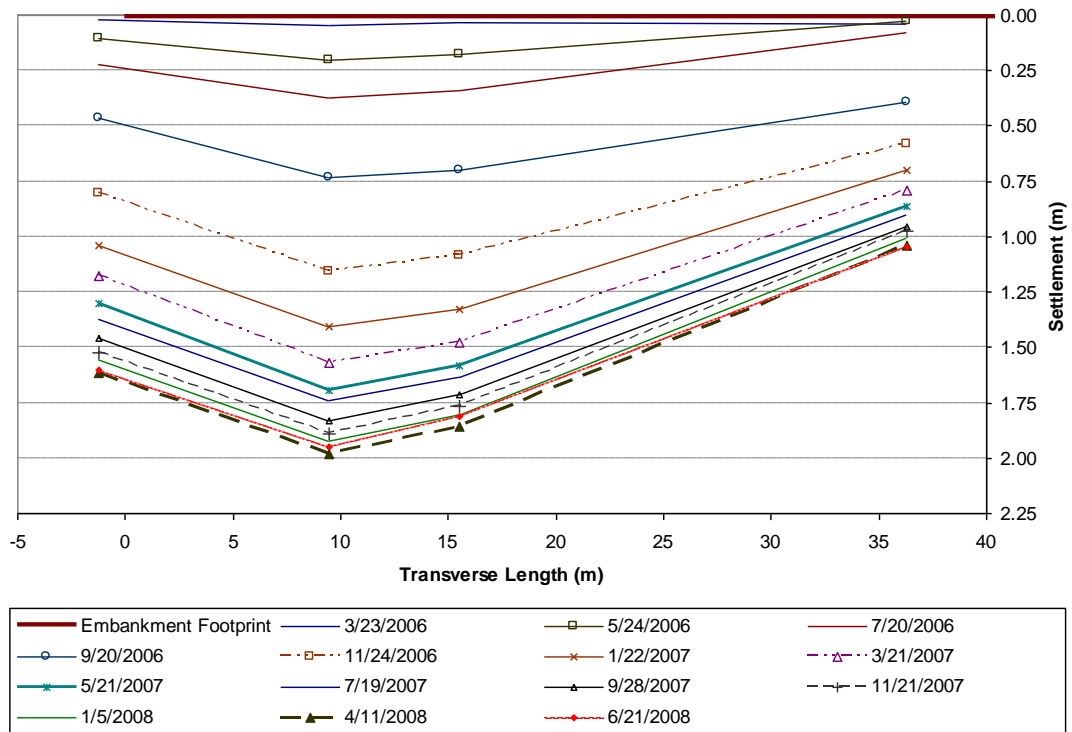


**Figure 2.5 Settlement profile for Station 289+00 (modified after Berkheimer, 2007).**

In Figure 2.5, three month recording intervals of settlement plate data were presented to summarize the settlement process. 04/11/2008 presents the last recorded data before the deconstruction of the embankment. At that time, the settlement plate 289-35L indicates 1.98 m (6.51 ft) of settlement. Later settlement data recorded on 06/21/2008 indicates less settlement than earlier readings, as this date corresponds to movement data recorded after removal of the embankment.

Figure 2.6 presents development of settlement with time. This data indicates that the soil had not completed consolidation at the time of embankment

removal, and that more settlement would have likely occurred. However, the asymptotic portions of the curves demonstrate that the soil was likely nearing the end of consolidation at the time of embankment removal.

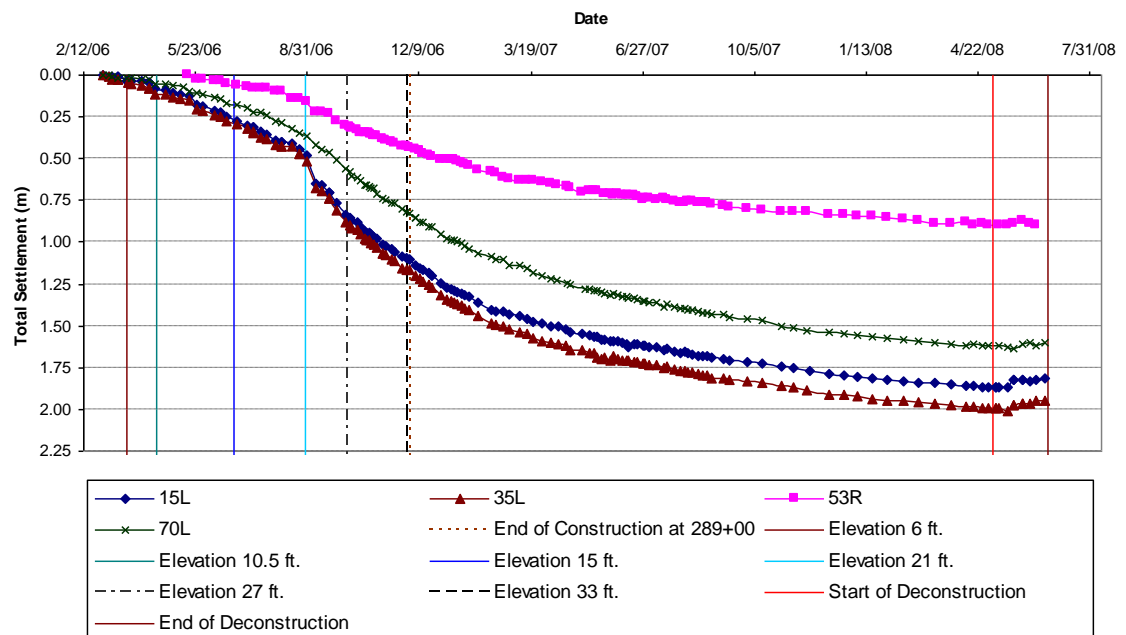


**Figure 2.6 Magnitude of settlement at Station 289+00(modified after Berkheimer, 2007).**

### 2.1.3 Piezometers

Piezometers were installed by the contractor to measure pore-water pressures in order to determine safe rates of fill and to monitor the performance of the embankment. The piezometers used in this project were vibrating wire piezometers, which convert applied water pressures to a frequency signal via a diaphragm and a tensioned steel wire. The vibrating wire readout device processes the signal and displays a reading. Calibration factors, which establish a relationship between pressure applied to the diaphragm and the frequency signal returned to the readout device, were used to convert *Hz* readings to engineering units (Slope Indicator 2006b).

Figure 2.2 shows the location of the four piezometers, each marked by an “X”, which were installed at Station 289+00. The piezometer data was collected weekly by DeIDOT. Figure 2.7 shows the change in pore water pressure with time (note that hydrostatic pore water pressures prior to the start of construction are not reflected in this graph, as it is  $\Delta u$  that is plotted). Details concerning the installation of these piezometers are shown in Table 2.3.

**Table 2.3 Piezometer Installation Data (Berkheimer, 2007)**

Piez. #	Sta.	Offset (m)	GS El. (m)	Installation			Dist. to Wall (m)	Cable Length (m)	Serial #	Install Date
				Depth (m)	Tip El. (m)	Drilled (m)				
5	289+00	13.72	0.82	22.25	-21.43	23.47	6.10	39.62	85011	1/5/2006
6	289+00	13.72	0.82	16.15	-15.33	17.37	6.10	30.48	85003	1/10/2006
7	289+00	2.74	0.88	22.25	-21.37	23.47	19.81	54.86	85021	1/9/2006
8	289+00	2.74	0.88	16.15	-15.27	17.37	19.81	48.77	85016	1/10/2006

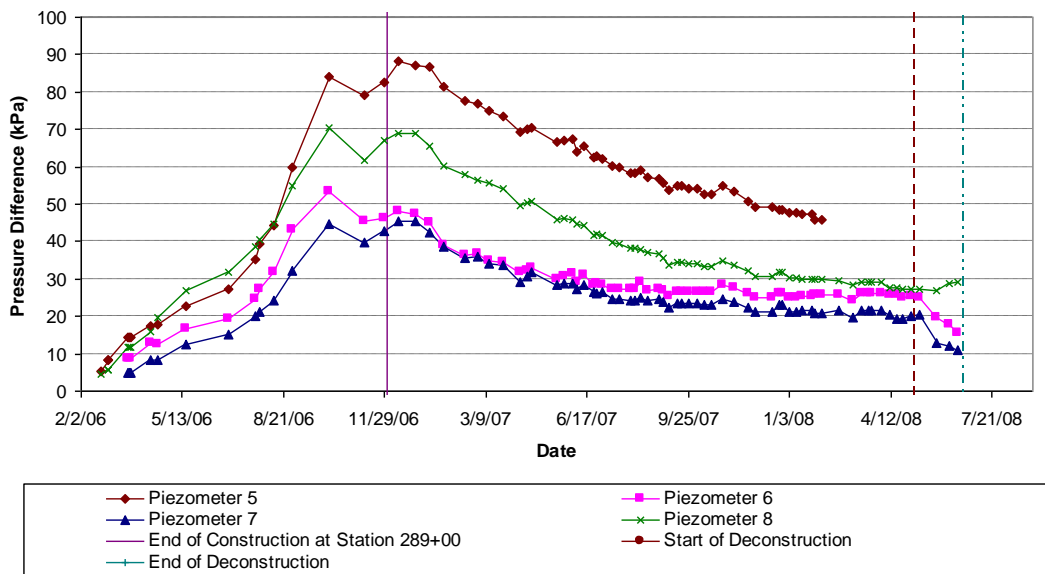


**Figure 2.7 Change in pressure difference with time at Station 289+00 (modified after Berkheimer, 2007).**

Figure 2.7 shows that the excess pore water pressure in the foundation soil increased due to construction of the embankment and dissipated at a slow rate after completion of embankment construction. Piezometer 5 stopped working on 02/04/2008. After embankment removal, there was a rapid decrease in excess pore water pressure due to unloading that was observed, which is expected. Interestingly, this behavior was not reflected in the pore pressure response recorded by piezometer 8. This observation, coupled with the significantly higher increases in pore water pressure that was observed for piezometer 8 (as compared with piezometer 7, which is at the same elevation) at the start of excavation might be an indication that the piezometer 8 readings might not be entirely reliable.

### 2.1.4 Inclinometers

Vertical inclinometers installed by the contractor were used for early detection of any lateral ground displacement caused by foundation movements.

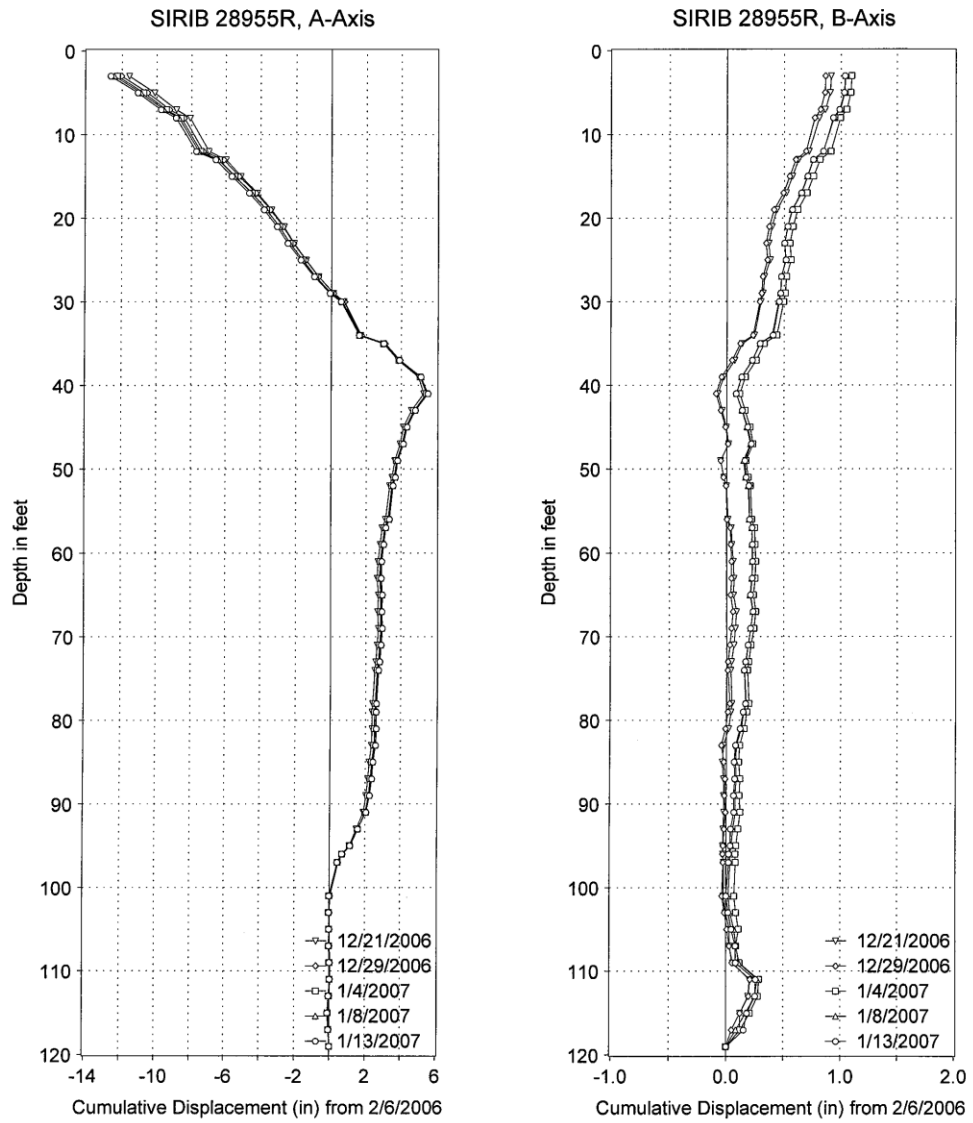
Vertical inclinometers are instruments for measuring relative horizontal displacements affecting the shape of a guide casing embedded in the ground or structure.

Inclinometer probes measure displacement in two perpendicular planes; therefore, displacement magnitudes and directions (vectors) can be calculated. The bottom end of the guide casing serves as a stable reference (datum) and must be embedded beyond the displacement zone. Relative displacements over time are determined by repeating measurements at the same depths and comparing data sets (Slope Indicator 2006b).

Two inclinometers; 289-75L and 289-55R were installed at Station 289+00 (Figure 2.2). The installation details for the inclinometers are shown in Table 2.4. Readings of the installed inclinometers were taken by DeIDOT. The data was processed using the program which was provided by the manufacturer of the inclinometers. The data was expressed in graphs, as presented in Figures 2.8 through 2.11.

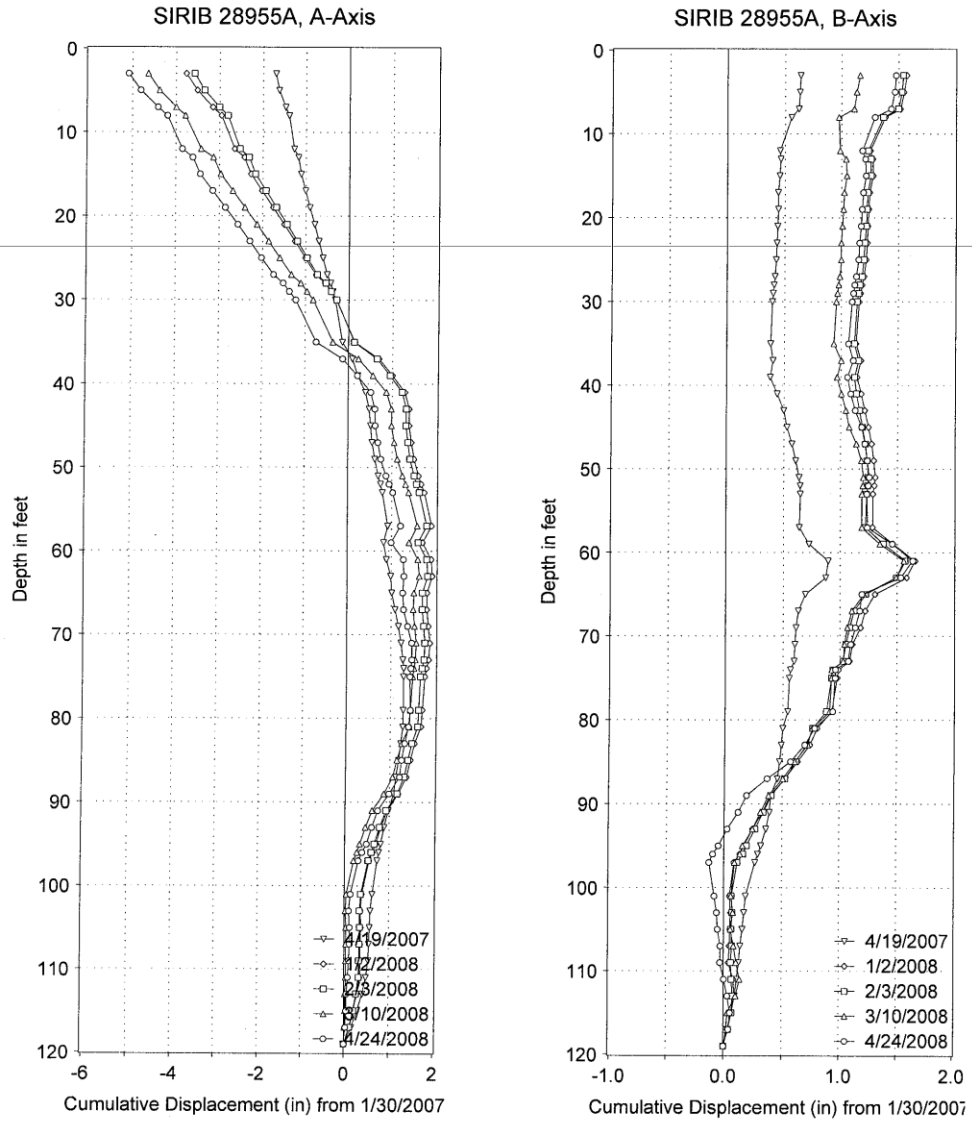
**Table 2.4 Vertical Inclinometer Installation Details (Berkheimer, 2007)**

Design Station	Design O/S (m)	Ground El. (m)	Top Pipe El. (m)	Approx. Tip El. (m)	AB Station	AB Offset (m)	Status
289+00	-22.86	0.91	1.71	-32.00	289+00.98	-23.15	Abandoned
289+10	-22.86	0.39	1.25	-32.92	289+08.81	-22.82	Replacement
289+00	16.76	3.13	3.83	-32.00	288+99.62	16.63	Abandoned
289+00	16.76	2.97	3.71	-32.00	289+09.00	16.29	Replacement



Greenman-Pedersen Inc. 10977 Guilford Road Annapolis Junction, Maryland 20701 Tel (410) 880-3055 Fax (301) 490-2649	Indian River Inlet Bridge Del-Dot Contract # 23-073-03 Sussex County, Delaware Field Office (302) 226-1251
--	---

**Figure 2.8 Inclinometer 289-55R data: 12/21/06 – 1/13/07.**



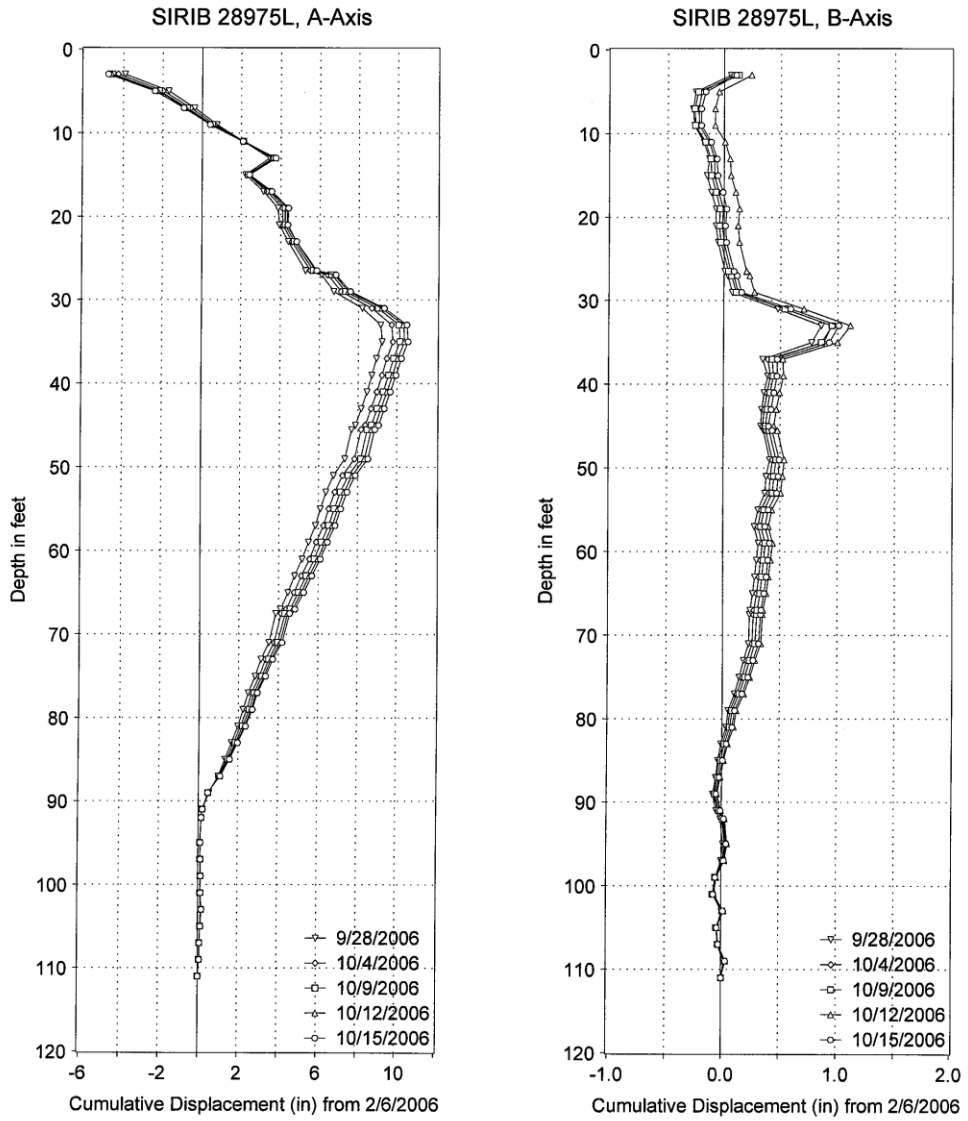
Greenman-Pedersen Inc.  
10977 Guilford Road  
Annapolis Junction, Maryland 20701  
Tel (410) 880-3055 Fax (301) 490-2649

Indian River Inlet Bridge  
Del-Dot Contract # 23-073-03  
Sussex County, Delaware  
Field Office (302) 226-1251

**Figure 2.9 Inclinometer 289-55A data: 04/19/2007 – 04/24/2008.**

Due to the large horizontal and vertical movements that were observed, the inclinometers became inoperable over time and they were replaced. As a reminder, construction of the embankment was completed on 12/01/2006 and removal of the embankment began on 04/20/2008. Inclinometer 289-55R became inoperable on 01/29/2007 due to large horizontal displacements (i.e., the horizontal displacement exceeded 0.2 m (8 in) at about 3 m (10 ft) depth and exceeded 0.1 m (4 in) at about 12.2 m (40 ft) depth (Figure 2.8, A-Axis). It was replaced on 01/29/2007 and labeled as 289-55A afterward. Figure 2.9 presents the measured cumulative horizontal movement of the inclinometer 289-55A from 04/19/2007 to 04/24/2008. The data indicates that the horizontal movement of the foundation of the embankment was still in progress but at a slower rate than what had previously been observed. For instance, in Figure 2.9, A-Axis, the displacement difference developed in one year time is about 0.1 m (4 in) in the region of 3.1 m (10 ft) depth and less than 0.05 m (2 in) around 18.29 m (60 ft) depth, indicating that the horizontal movement was likely stabilizing.

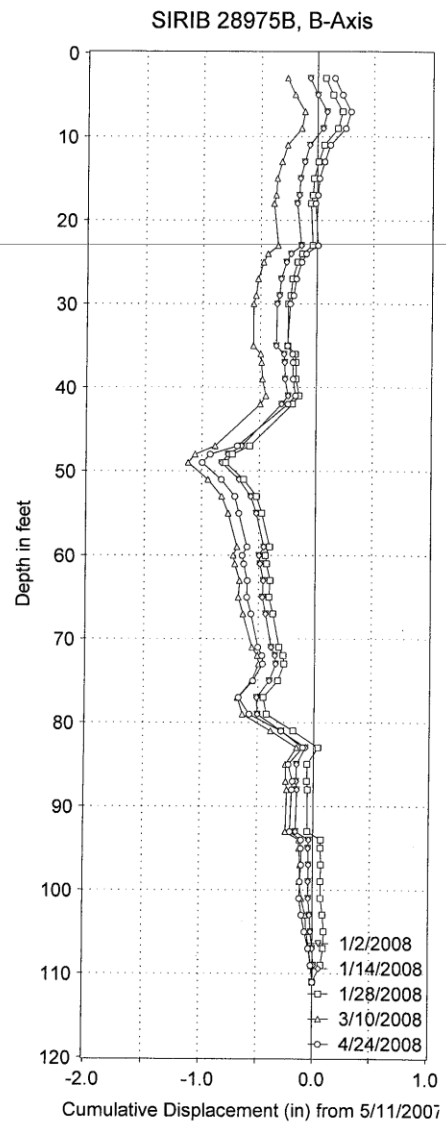
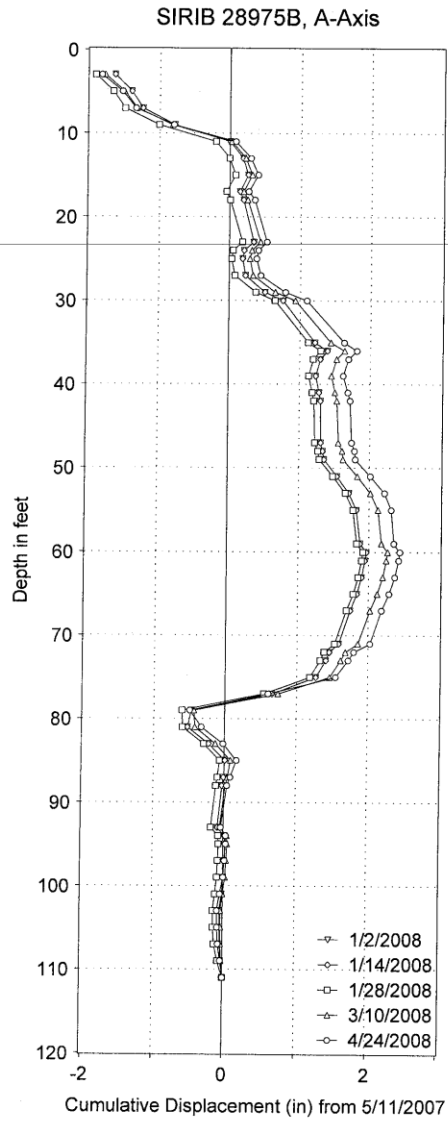
On 10/24/2006 inclinometer 289-75L was replaced and named as 289-75A, again necessitated by excessive horizontal embankment movements (i.e., Figure 2.10, A-Axis, the horizontal displacement exceeds 0.25 m (10 inches) in the region of 11 m (35 feet) depth, about one month before the completion of the embankment construction). This inclinometer (189-75A) was replaced again on 05/11/2007 and named as 289-75B. Figure 2.11 presents the measured cumulative horizontal movement of the inclinometer 289-75B from 01/02/2008 to 04/24/2008. In Figure 2.11 the data (i.e., the displacement difference developed in four months is about 0.05 m (2 in) around 18.3 m (60 ft) depth) indicates that the horizontal movement of the foundation had not stopped yet but was likely stabilizing.



Greenman-Pedersen Inc.  
10977 Guilford Road  
Annapolis Junction, Maryland 20701  
Tel (410) 880-3055 Fax (301) 490-2649

Indian River Inlet Bridge  
Del-Dot Contract # 23-073-03  
Sussex County, Delaware  
Field Office (302) 226-1251

**Figure 2.10 Inclinometer 289-75L data: 09/28/06 – 10/15/06.**



Greenman-Pedersen Inc. 10977 Guilford Road Annapolis Junction, Maryland 20701 Tel (410) 880-3055 Fax (301) 490-2649	Indian River Inlet Bridge Del-Dot Contract # 23-073-03 Sussex County, Delaware Field Office (302) 226-1251
--	---

**Figure 2.11 Inclinometer 289-75B data: 01/02/2008 – 04/24/2008.**

### **2.1.5 Wall Targets**

Wall targets were used to collect data about both the vertical and the horizontal movement of the embankment. The targets were installed (placed) on the wall and the vertical and horizontal movements were measured using a laser surveying technique which tracked the movements of the targets from a stable location away from the embankment.

Readings of the installed wall targets were taken by DeIDOT. Figure 2.12 presents the placement of the wall targets at Wall 1 Station 289+00. Wall target 1-26 was installed on layer 9 at 4.1 m (13.5 ft) elevation on 07/10/2006 and wall target 1-73 was installed on layer 20 at 9.1 m (30 ft) elevation on 10/19/2006. It should be noted that these elevations changed over time due to the high degrees of settlement that were observed. Wall target 1-25 was installed on 07/10/2006 and became inoperable on 11/05/2006 due to the significantly large amount of settlement that was observed; consequently, it is not presented in the figures. Figures 2.13 through 2.15 present the wall target data.

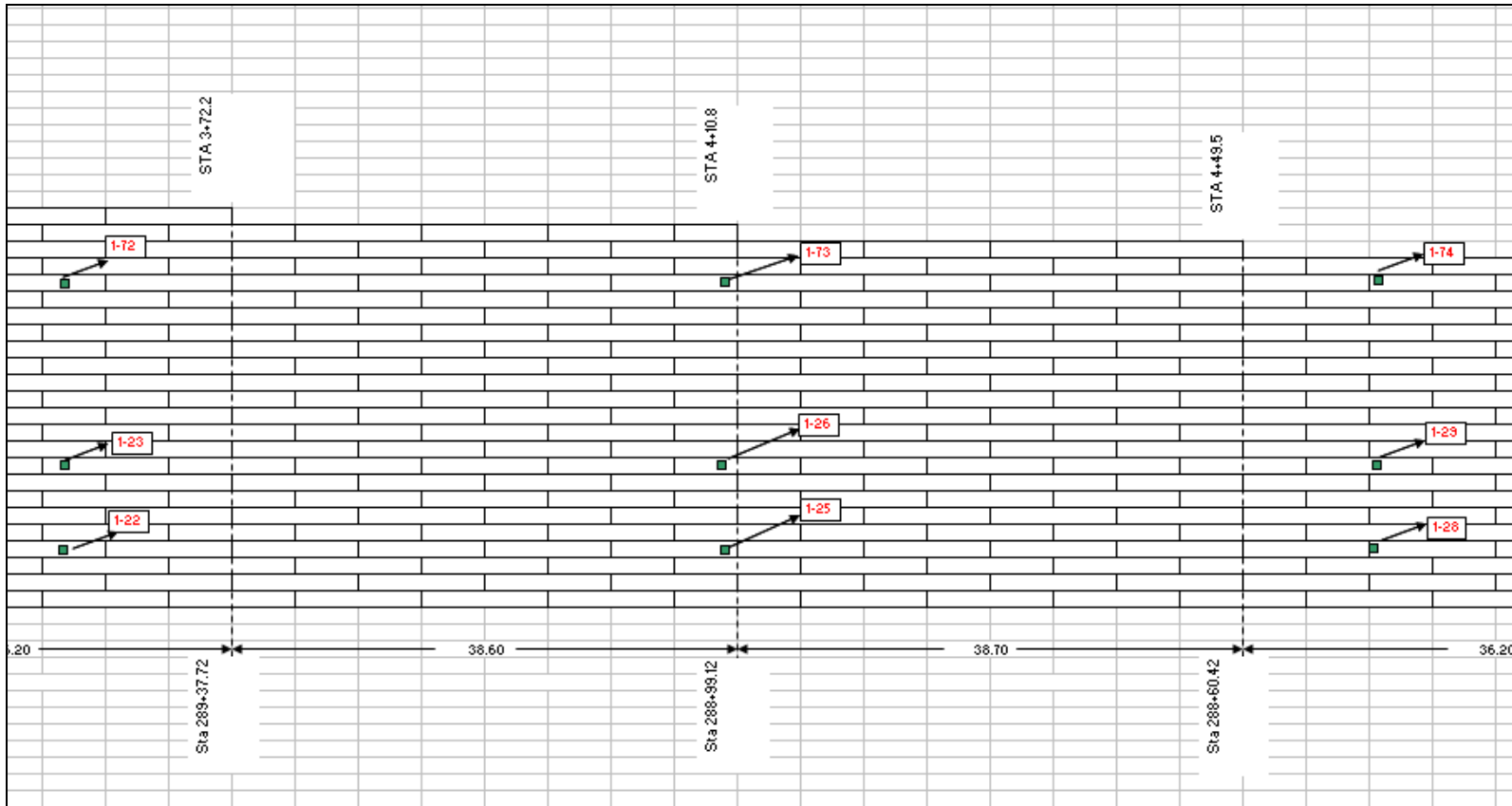
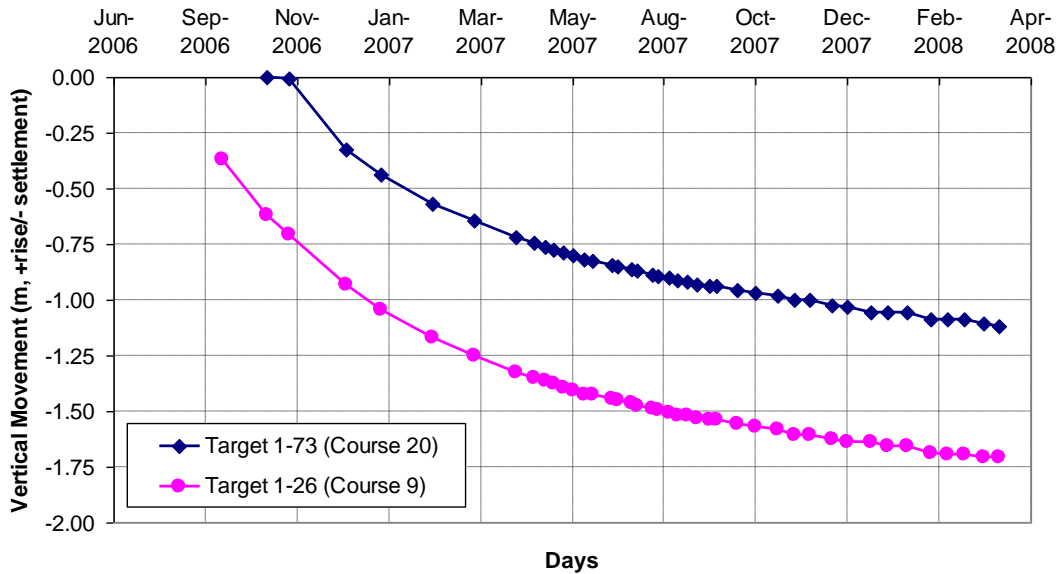


Figure 2.12 Wall target placement at Wall 1 Station 289+00 (not to scale).

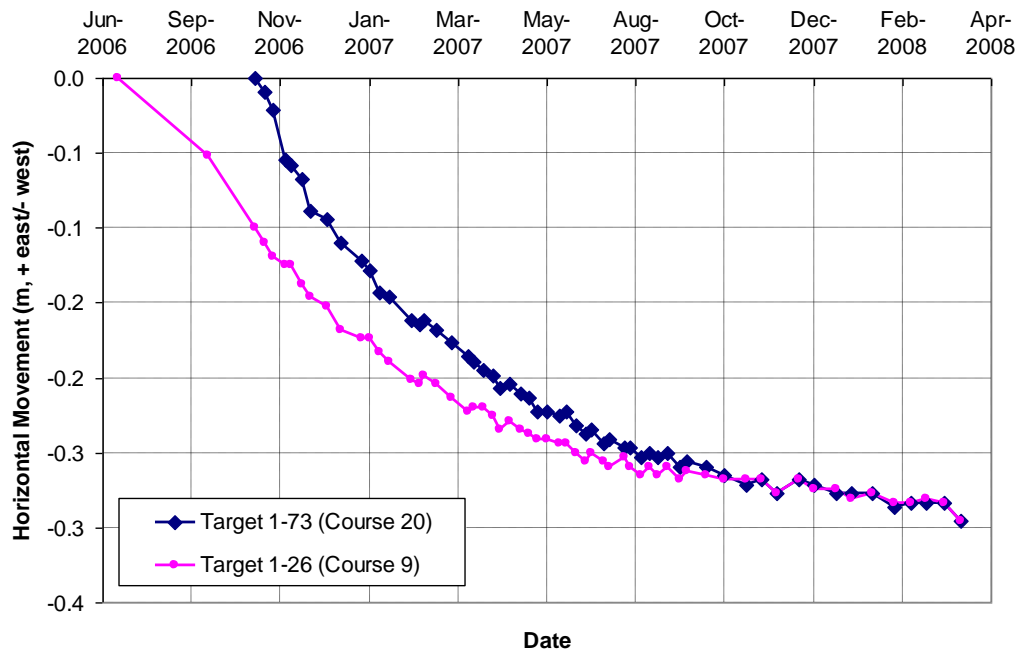
Figure 2.13 shows the vertical movement of Wall 1 at Station 289+00, as recorded by the surface-mounted wall targets. It should be noted that this figure does not present a complete vertical displacement record, since the targets were installed at dates after the construction started. For instance, wall target 1-26, which was installed five months after the start of construction, indicates almost 1.8 m (6 ft) consolidation. However, it is also essential to consider the settlements that occurred during the first 5 months, which means that the vertical movements in Wall 1 Station 289+00 probably significantly exceeded 1.8 m (6 ft). In addition, it can be observed in Figure 2.13 that although the vertical movement was still in progress, the vertical movement was nearing a more stable situation at the time of embankment removal (as evidenced by the asymptotic portions of the curves). Displacements obtained from settlement plates (Section 2.1.2) and inferred from wall target measurements showed good agreement.



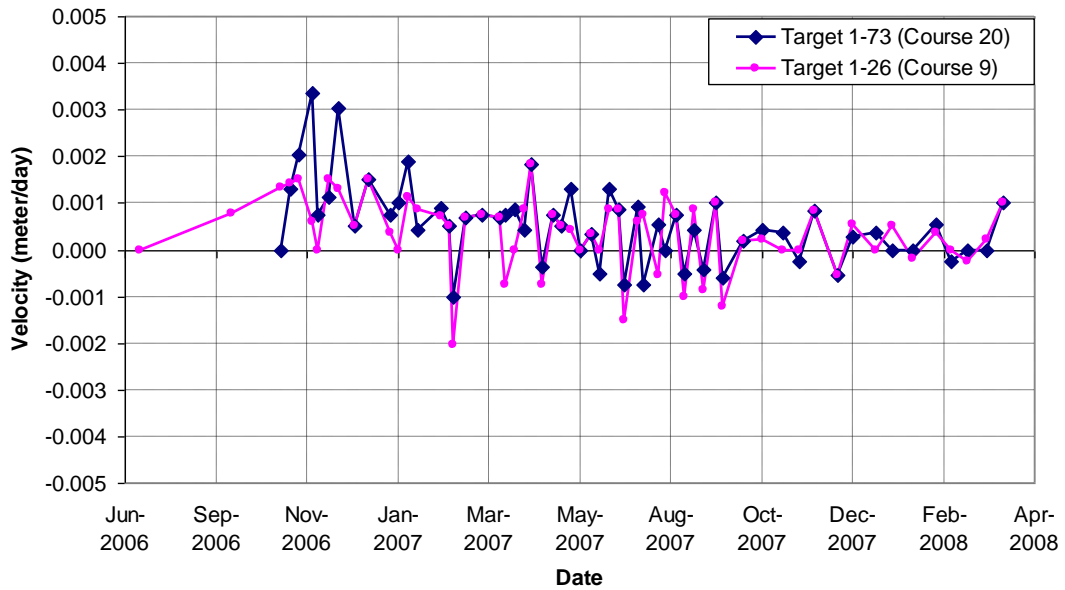
**Figure 2.13 Vertical movement versus time Wall 1 Station 289+00 (modified after Berkheimer, 2007).**

Figure 2.14 presents the horizontal movements of Wall 1 Station 289+00. Again, it should be noted that this figure does not present a complete horizontal displacement record, since the targets were installed at dates well beyond the commencement of construction. The data in Figure 2.14 indicates that the embankment moved about 0.3 m (1 ft) towards the west. To track the rate of horizontal movement, the measured change in horizontal movement between measurements was divided by the interval time between the measurements to determine the movement velocity in meter per day (Figure 2.15). As construction of the embankment continued, the horizontal movement rates tended to increase due to the additional load application over time, which triggered a movement response in the

underlying soil. Over time, the movement rates decreased, which indicates that that the system was likely becoming more stable.



**Figure 2.14** Horizontal movement versus time Wall 1 Station 289+00 (modified after Berkheimer, 2007).



**Figure 2.15 Horizontal movement rates versus time Wall 1 Station 289+00 (modified after Berkheimer, 2007).**

### 2.1.6 Settlement of the South Embankment

Figures 2.16 through 2.18 show the high degrees of settlements at the north edge of the south embankment (Station 293+00) at three different dates. By examining the crooked chain link metal fence adjacent to the wall, the influence zone can be determined easily. Figure 2.16 was taken on 12/21/2007; one year after the construction of the embankment was completed. Figure 2.17 was taken on 05/28/2008 during the removal process of the embankment. Figure 2.18 was taken on 06/27/2008 after the deconstruction of the embankment.



**Figure 2.16 Influence zone South Embankment Station 293+00– 12/21/2007.**



**Figure 2.17 Influence zone South Embankment Station 293+00- 05/28/2008.**



**Figure 2.18 Influence zone South Embankment Station 293+00– 06/27/2008.**

## **2.2 Instrumented Mechanically Stabilized Earth Walls**

Geogrid reinforced mechanically stabilized earth (MSE) walls were constructed over highly compressible cohesive soils to support the construction of new bridge approach embankments at the Indian River Inlet project. Wall 1 at Station 289+00 had been instrumented and monitored with strain gages to verify that the geogrid reinforcement was not overstressed. The following case studies provide information about previous projects that utilized strain gages to monitor reinforcement in mechanically stabilized earth walls which were constructed on soft foundation.

### **2.2.1 Application of Strain Gages and the Analysis of the Deformation Behavior of Geosynthetics**

To analyze the deformation behavior of various types of geosynthetic reinforcement, load-elongation properties and local deformation measurement data are needed. Strain gages were considered to be a possible solution for making field deformation measurements, with research on this topic beginning in the 1980s. Attachment of strain gages to geosynthetics is not an established process yet. There are no accepted standard procedures for such a process. The variety of geosynthetics does not make possible for a unique procedure to emerge. Considering the environment in which it needs to operate, the process is even more challenging. There are a number of unique and creative methods suggested by researchers for strain gage installation. As one example, Sluimer and Risseeuw (1982) and Leshchinsky and Fowler (1990) have suggested using silicon (as a flexible adhesive) to attach strain gauges to woven geotextiles. Installation methods are typically modified for different types of projects and geosynthetics. A detailed procedure is recommended by Soong and Koerner (1998) for attachment of strain gages to geotextile:

- Use a degreaser or solvent to degrease the surface.
- The surface should be abraded using a dry powdered cleaner that lightly scratches the surface, creating more surface area for bonding.
- The surface should next be cleaned using a cotton swab and rubbing alcohol.
- A strain gage should be placed bonding side down on a clean glass plate.
- A piece of cellophane tape is placed over the gage, and then lifted to act as a carrier for the gage.
- A thin layer of adhesive is placed on the prepared area of the geogrid, and the tape with the gage is placed over the glued surface.

- A piece of gauze should be used to wipe over the area, pressing the gage into the glue.
- Next, a glass slide and a Neoprene backup pad are placed over the installed gage, followed by deadweight for curing.
- The weight, rubber, and glass should be removed after the adhesive is cured.
- The tape is then removed by slowly pulling it back over itself. Wires are soldered to the terminal points of the gage, with slack left in the leads to prevent tensile force from being transferred to the terminal.
- Finally, the entire gage assembly should be coated with RTV silicone.

Won and Kim (2006) present a case where they analyze the deformation behavior of reinforcements within GRS walls. In this case, two GRS walls were constructed in the field, each standing 5 m, on a shallow-layered weak foundation. These walls were constructed using a compound arrangement of nonwoven geotextiles, woven geotextiles, and geogrids. The deformation behavior of the geosynthetics inside the GRS walls was analyzed using the data collected from 124 strain gauges attached to the non-woven geotextiles, woven geotextiles and geogrid reinforcement for about 1.5 years (Won & Kim, 2006). The GRS walls were divided into SECTION I (nonwoven and woven geotextile) and SECTION II (nonwoven and geogrid), then subdivided into sections A, B, C, and D.

Figures 2.19 through 2.21 present typical strain values measured in the strain gage instrumented geogrid reinforced section (i.e. Section D, 4<sup>th</sup> layer), in the nonwoven geotextile reinforced section (i.e. Section C, 3<sup>rd</sup> layer) and in the woven geotextile reinforced section (i.e. Section A, 4<sup>th</sup> layer), respectively.

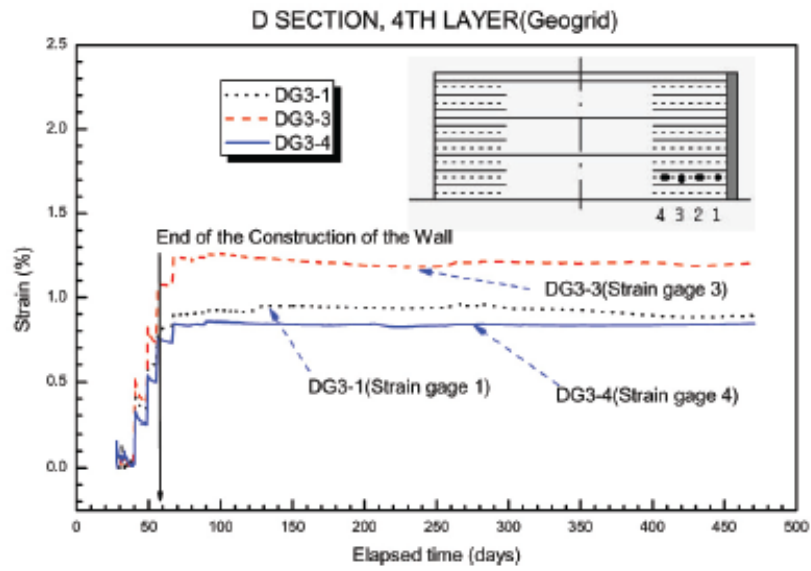


Figure 2.19 Geogrid deformation on the GRS wall (Won & Kim 2006).

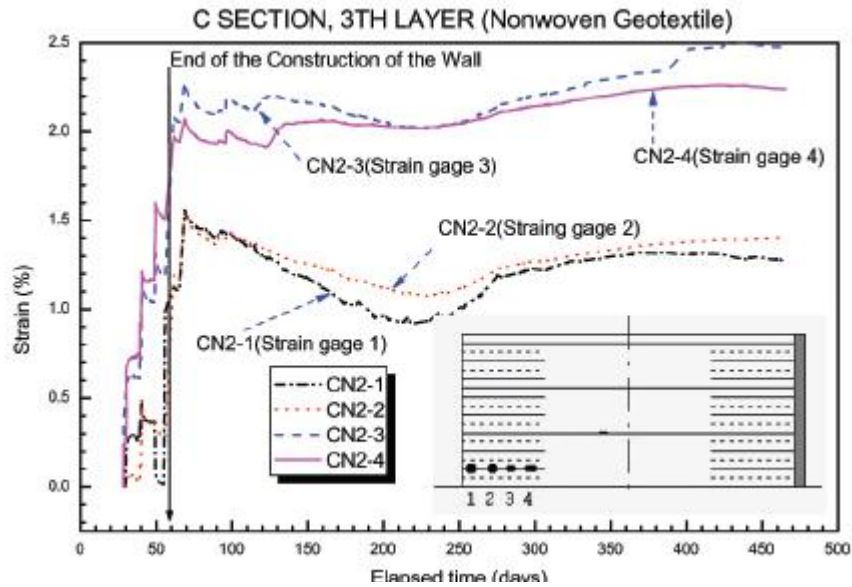
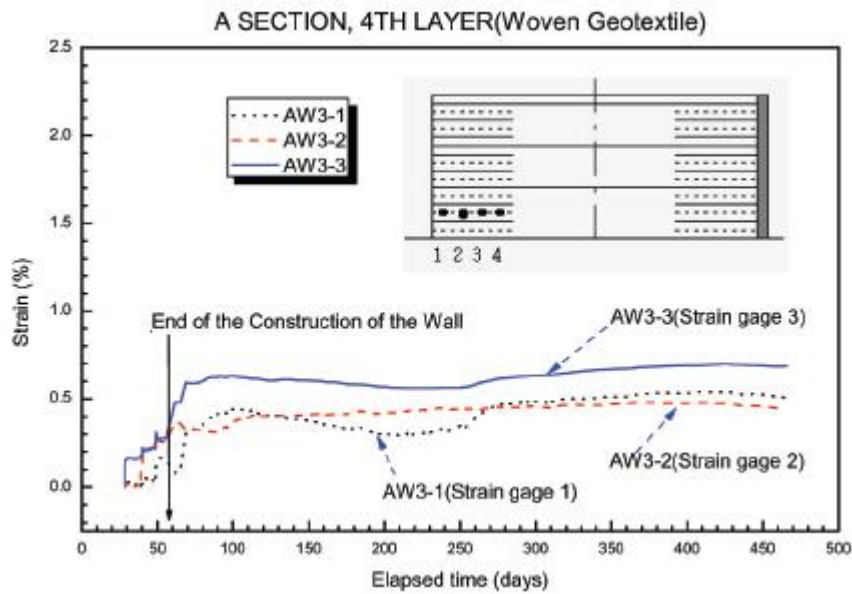


Figure 2.20 Nonwoven geotextile deformation on the GRS wall (Won & Kim 2006).



**Figure 2.21 Woven geotextile deformation on the GRS wall (Won & Kim 2006).**

Figure 2.22 and 2.23 presents the deformation behavior of geosynthetics in SECTION I and SECTION II respectively, along the wall height with elapsed time. The maximum deformation measured during construction to 10 days after the completion of the walls was as follows: nonwoven, 2.94%; woven, 0.65%; and geogrid, 1.07%. The maximum deformation measured for 16 months was as follows: nonwoven, 6.05%; woven, 2.92%; and geogrid, 2.33%. Won and Kim (2006) concluded that, for GRS wall construction using nonwoven geotextiles, woven geotextiles, and geogrids, most internal deformations occurred within 25 days after the installation of the walls. The maximum deformations that were recorded over the next 16 months ranged from 2.3% to 6.1%. Thus, the geosynthetics installed within the GRS wall appear to be safe. From this research, it was concluded that in GRS walls,

nonwoven geotextiles show larger deformation ranges than woven geotextiles or geogrids; however, the deformation patterns of these three reinforcement materials are similar, and the strain gauges attached to the geosynthetics functioned normally over a 16-month time frame (Won & Kim, 2006).

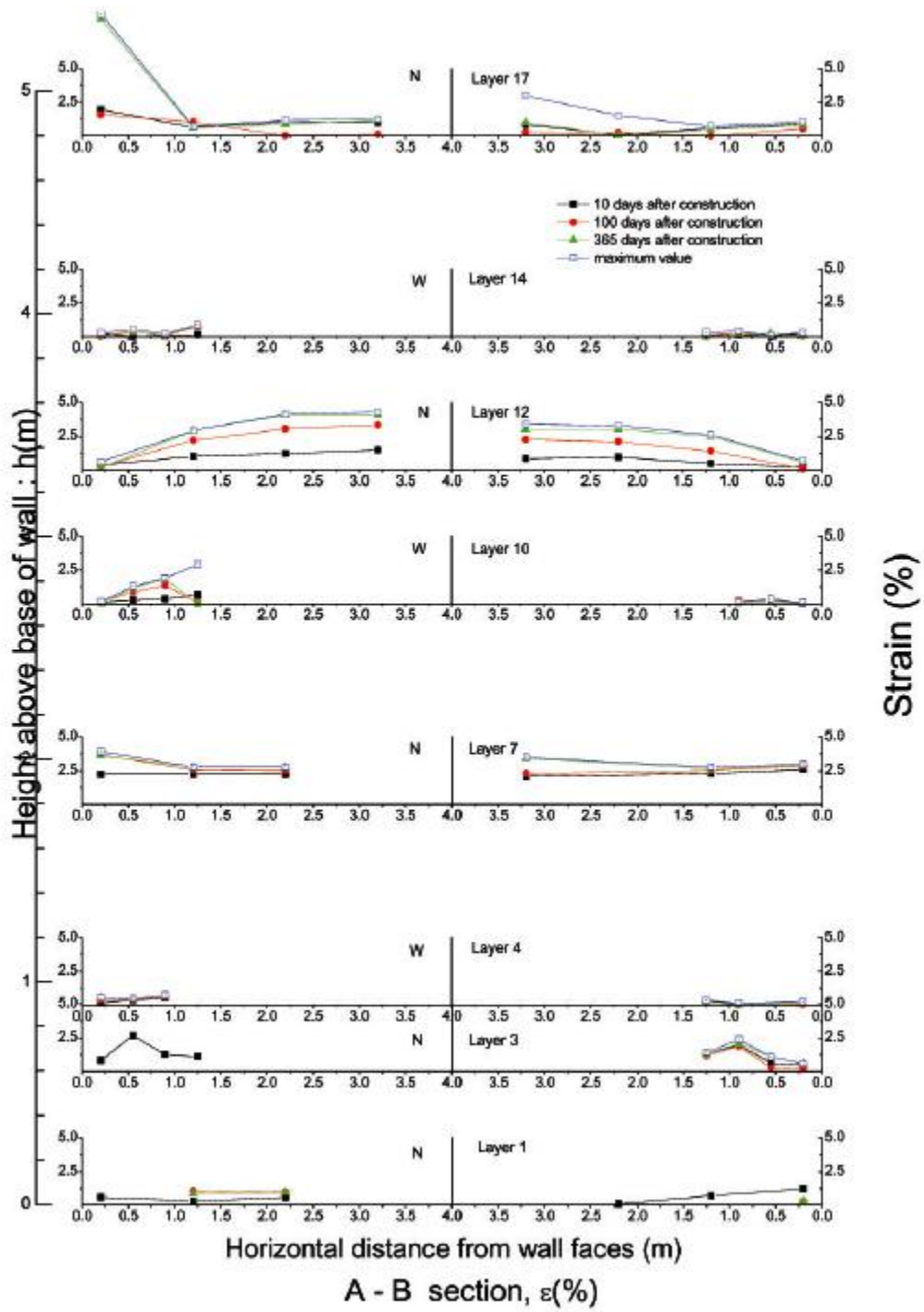


Figure 2.22 Geosynthetics Deformation in Section I (Won & Kim, 2006).

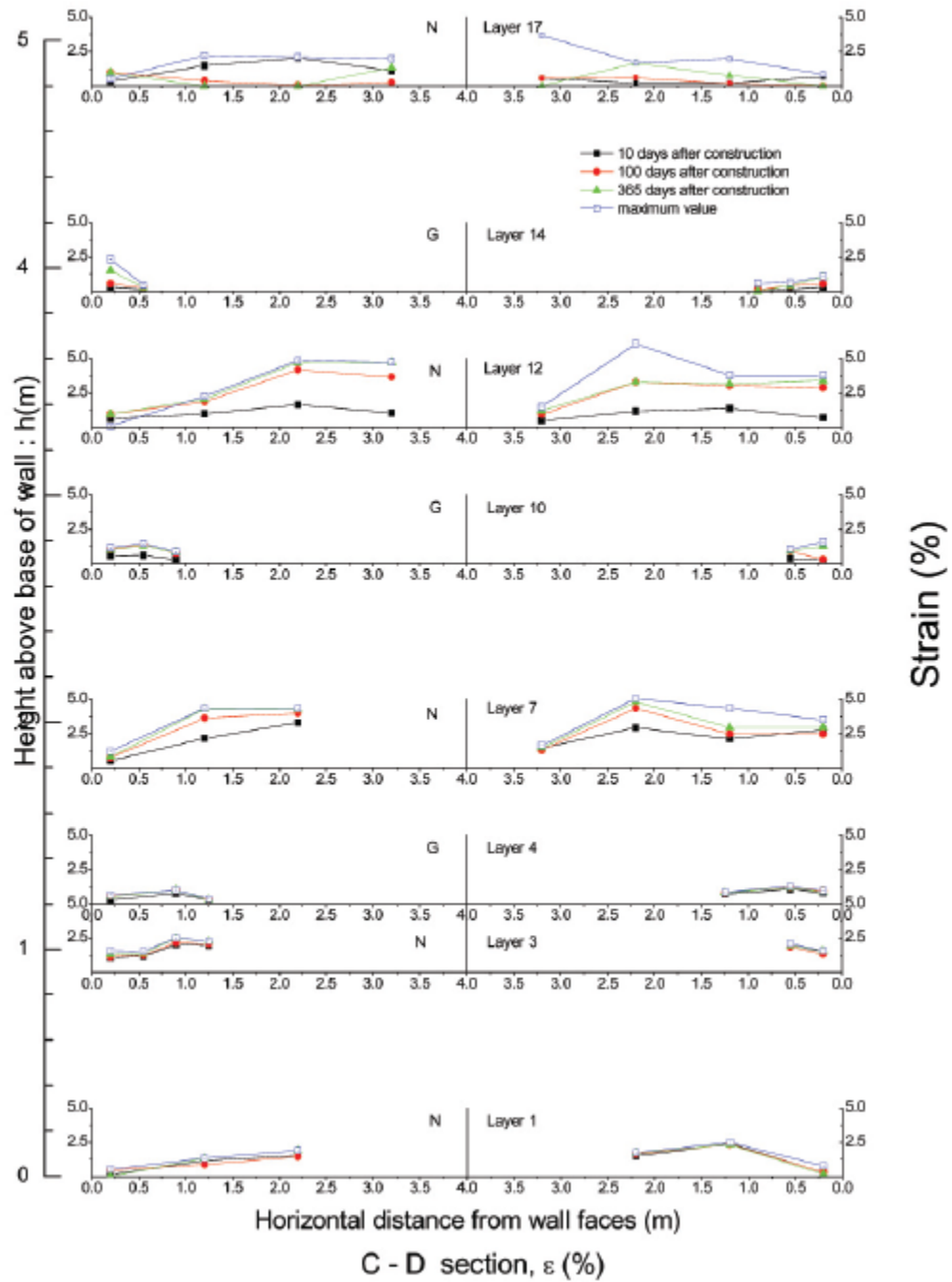


Figure 2.23 Geosynthetics Deformation in Section II (Won & Kim, 2006).

### **2.2.2 MSE Wall on I – 15 Salt Lake City Utah, USA**

A large MSE wall with metallic reinforcement has been constructed over soft soils as part of the I-15 reconstruction project in Salt Lake City, Utah. The foundation soil profile in the instrumented section is summarized in Table 2.5. Wall height is about 9.14 m (30 ft) tall at the area of instrumentation (i.e. instrumented wall Wall R-346-1C). Due to the soft soil strata and relatively tall wall being constructed, settlements around 1 meter (3 ft) anticipated near the face of the wall. Therefore, these wire-faced walls exhibit large deformations particularly around the wall foundation. These deformations include bulging, sagging, and negative batter. Because of the deformations observed in walls constructed early in the project, design modifications have been implemented. These modifications include shorter, intermediate bar mats between the lower primary reinforcement mats. These intermediate bar mats are placed from the bottom of the wall up to a height 4.57 m (15 ft) below the top of the wall. Wall R-346-1C was instrumented to monitor stresses and deformations in the wall and deformations in the foundation soils throughout construction, primary consolidation, and secondary consolidation (Bay et al., 2003).

The instrumentation in Wall R-346-1C includes the following: (a) strain gages on the bar mats to monitor tension in the longitudinal members, (b) pressure cells in the wall backfill to monitor vertical pressure, (c) horizontal and vertical inclinometers in the foundation and wall backfill to monitor the sub-surface movement, (d) horizontal extensometers in the wall backfill to monitor the horizontal movement of the wall, (e) Sondex systems in the wall backfill and foundation to monitor settlement, and (f) survey monuments at the ground surface outside the wall backfill to measure settlement (Bay et al., 2003). Only strain gage instrumentation will be overviewed in this section.

**Table 2.5 Site Soil Strata (Bay et al., 2003)**

<b>Stratum</b>	<b>Material Description</b>	<b>Approximate Depth, ft</b>
I	Fill: Course Sand and Concrete Rubble	Surface to 8
II	Soft Clay	8 to 19
III	Soft Silty Clay	19 to 30
IV	Stiff to Hard Sandy Clay	30 to 85
V	Very Stiff to Hard Clay	85 to 90

Since the wall had a design change, it was decided to monitor two different sections of wall that consisted of the old design and new design. The older design section (Figure 2.24) of wall only utilized 7.32 m (24 ft) primary mats spaced in lifts of 0.76 m (2.5 ft). The newer design section (Figure 2.25) utilized both the long primary mats and the 3.05 m (10 ft) intermediate mats. It must be noted that the older design is referred to as the primary reinforcement only section and the newer design is referred to as the intermediate and primary reinforcement section. The two locations of instrumented wall included 14 layers of primary reinforcement, three layers of intermediate reinforcement, 14 fascia panels, approximately 500 strain gages, and about 7,000 m (23,000 ft) of cabling (Bay et al., 2003).

The layout and location of the strain gage measurement points were decided based on the anticipated behavior in the field as well as on previous experiences with other instrumented walls (Sampaco et al., 1994). The

instrumentation was designed in order to obtain sufficient information on the following relevant parameters:

(a) Determining the spatial variation in tension in the longitudinal wires, noting the variation as a function of the position with respect to the top of the wall as well as tension variation with respect to the distance from the face of the wall.

(b) Magnitude of axial tension in the longitudinal members of the fascia panel and tensile variation with respect to distance below the top of the wall.

(c) To determine the locus of maximum tension for the entire height of the wall.

(d) To maintain some redundancy in case of damage to gages or wiring during the course of the construction process (Bay et al., 2003).

The instrumented section of Wall R-346-1C containing only primary reinforcement consists of 13 primary reinforcing bar mat layers with no intermediate bar mats present. Figure 2.24 shows an elevation of this particular section of instrumented wall, which was the original design. Only a relatively small section of this wall was constructed using only primary reinforcement. The two instrumented mats for each instrumented layer had two sections also constructed with only primary reinforcement on either side, such that boundary effects due to the intermediate reinforcement would be minimal. Thus, a section of the wall approximately 10.1 m (33 ft) long had only primary reinforcement, while the remainder of the wall had both primary and secondary reinforcement (Bay et al., 2003).

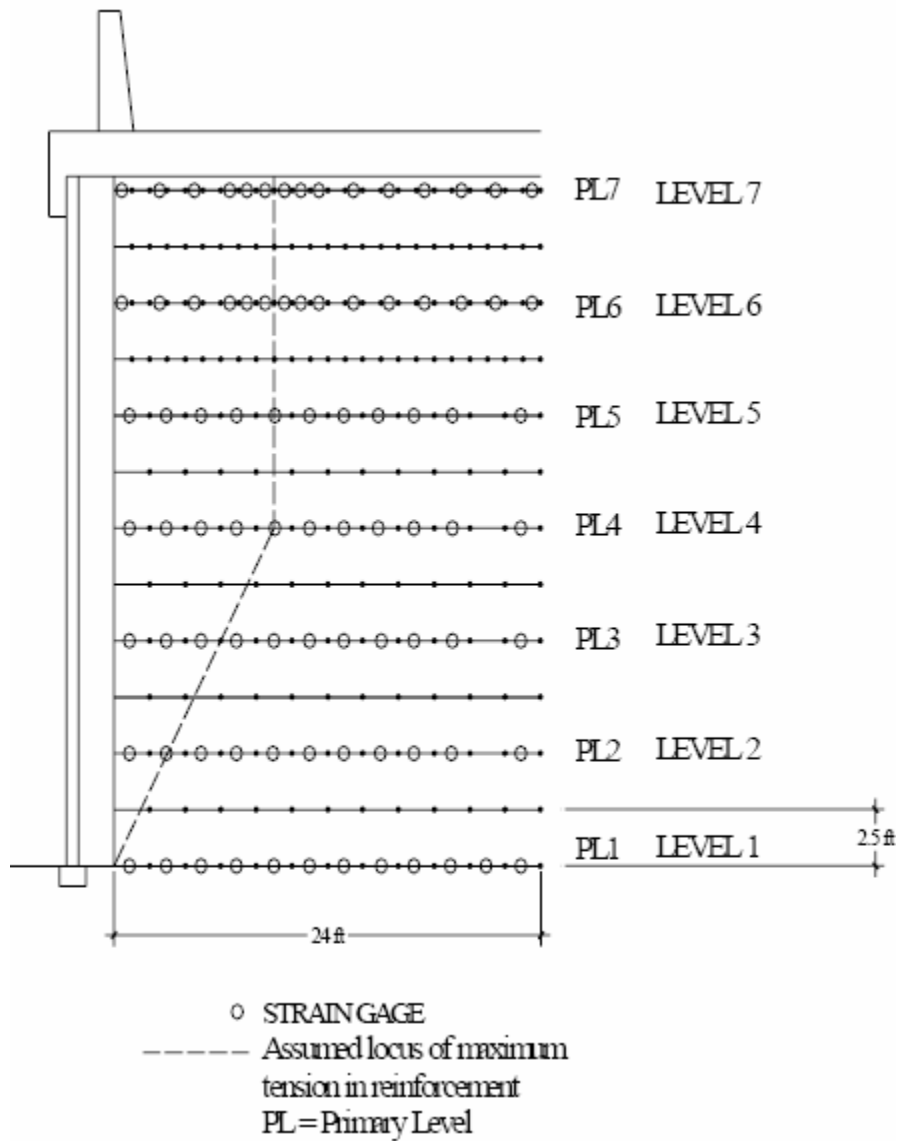


**Figure 2.24 Elevation View of Wall Section with Instrumented Primary Reinforcement (Bay et al., 2003).**

The instrumented section of Wall R-346-1C containing both primary and intermediate reinforcement consists of 13 primary reinforcing wire mat layers and six

layers of intermediate reinforcing wire mats as shown in Figure 2.25. A typical primary reinforcement layer of wall consists of two wire mesh straps that range from 0.46 m (1.5 ft) to 0.76 m (2.5 ft) wide by 7.32 m (24 ft) long with a 1.68 m (5.5 ft) center-to-center lateral spacing. A typical intermediate layer consists of two 0.46 m (1.5 ft) wide by 3.05 m (10 ft) long wire mesh straps with the same lateral center-to-center spacing as the primary mats (Bay et al., 2003).

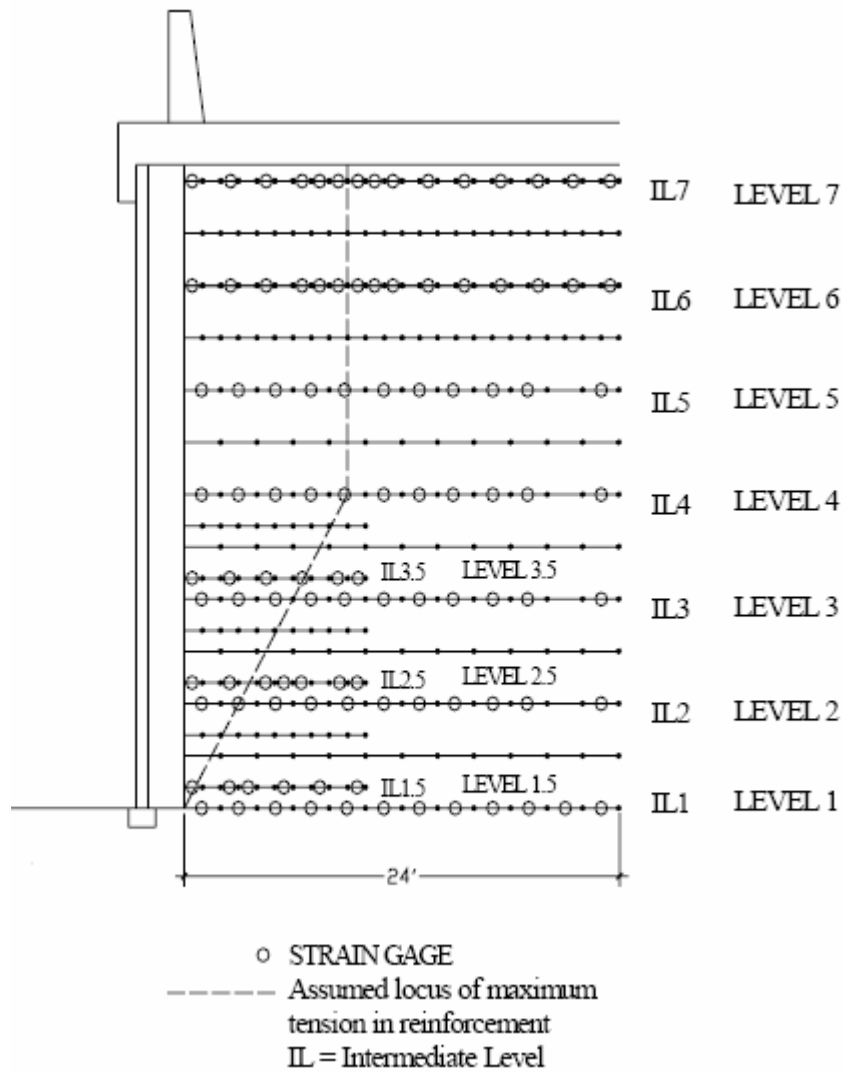


**Figure 2.25 Elevation View of Wall Section with Instrumented Primary and Intermediate Reinforcement (Bay et al., 2003)**

Horizontal stress distributions in the wall were measured with strain gages attached to the welded wire bar mats. The force induced in the bar mats by the backfill placed above the mat at the time of readings is obtained from the difference between

the initial and subsequent readings. The difference in readings was converted to a force,  $F$ , by using a calibration factor that was determined for this specific project (Bay et al., 2003). Figure 2.26 shows an example of the measured bar forces for instrumented mats in “primary layer 2”. The plots show the bar forces versus height of fill above the mat level.

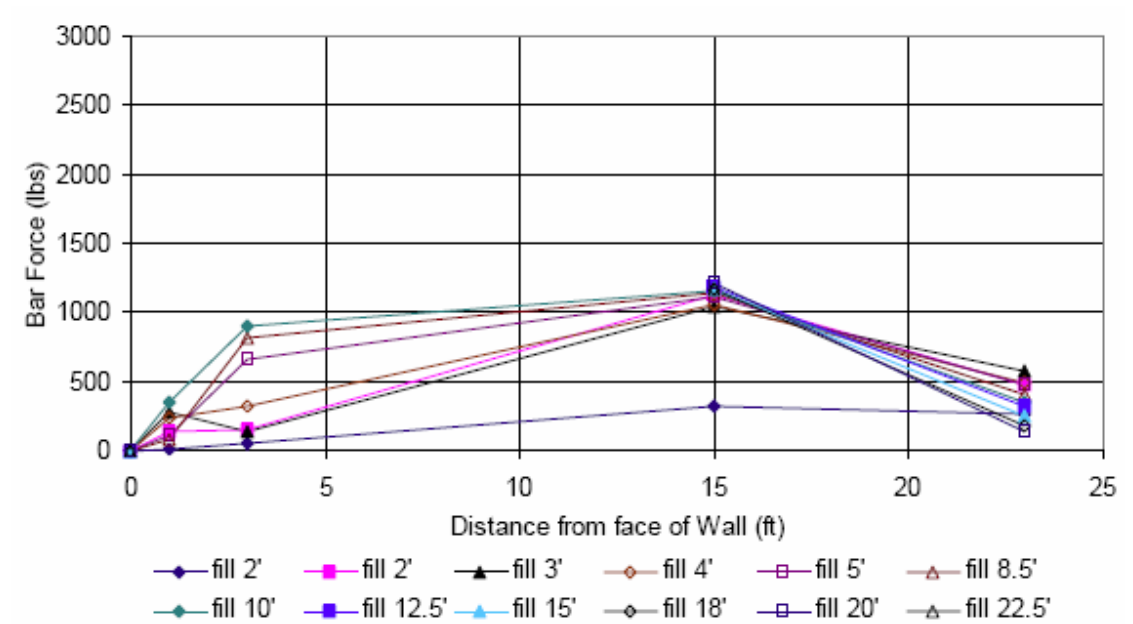


**Figure 2.26 Measured Bar Forces for Primary Reinforcement Only Layer 2 (Bay et al., 2003).**

Using the measured bar forces, the force distribution is also illustrated along the wall height and maximum tension force is compared with the assumptions

for the bilinear potential failure line and Coulomb potential failure line. Figure 2.27 is an example of the tension distribution measured before the completion of construction in the section of wall containing both primary and intermediate reinforcement.

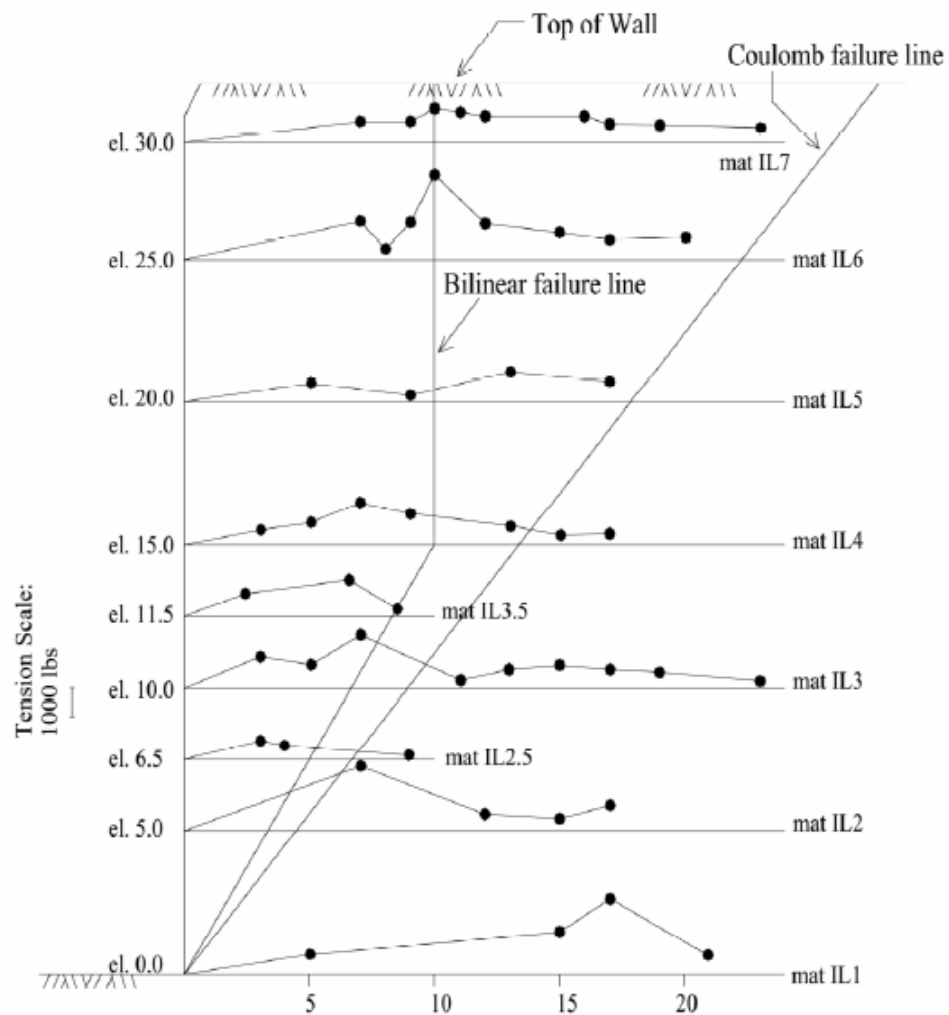


**Figure 2.27 Tension Distribution in Bar Mats in the Primary and Intermediate Reinforced Wall Section (Bay et al., 2003)**

From the measured strain data, Bay et al. (2003) concluded that the maximum tension in the bar mats was much less than the allowable tension to which the bar mats could be subjected. The minimum ratio of the allowable yield stress to the tensile stress existing in the longitudinal bars of the reinforcement is 2.5 for one strain gage position, with only four gage positions having ratios less than 5.0 (out of more than 90 functional positions). Thus, the vast majority of the bar mats are subjected to tensile forces less than 20 percent of the yield strength of the material. The allowable stresses used in calculating these ratios considered the entire cross section of the longitudinal bar, not taking into account corrosion of the steel over time, which decreases the cross sectional area (Bay et al., 2003).

## Chapter 3

### PROCEDURE TO ASSESS STRESS IN POLYMERIC REINFORCEMENT UTILIZING EXHUMED SPECIMENS

#### 3.1 Exhumation Process at IRIB

The embankments accessing the planned Indian River Inlet Bridge (IRIB) were removed as a result of the excessive movements that were observed during and after construction (Chapter 2). The deconstruction process started on 04/21/2008 and was completed in three months. This removal created the opportunity to exhume specimens of geogrid reinforcement, most notably those with strain gages. These specimens could then be examined in the lab to assess their residual or plastic strain. Proper interpretation of plastic strain can be used to infer the load induced in the geogrids while in-service. The exhumation also provided an opportunity to examine the strain gages that were attached to the geogrids, presenting an opportunity for further examination of the relatively poor performance of most of the gages. The nature of the recorded strain data measured prior to embankment excavation is discussed in more detail in Berkheimer (2007).

The removal of the embankments was planned to take three months. The backfill was excavated, and hauled by trucks to a remote dumping site. The geogrid specimens were exhumed during excavation. Figures 3.1 through 3.4 depict the exhumation process that was generally used across most of the site (though not at the instrumented section). At the request of the Delaware DOT (DeIDOT), exhumation of

the geogrids in Wall 1, Station 289+00 (i.e., location where strain gages were attached) was performed more carefully than at other wall sections. That is, the exhumation technique that was used resulted in only minor damage to the geogrids at the instrumented location.



**Figure 3.1** Removal process of backfill (5/23/2008).



**Figure 3.2** Removal process often damaged the embedded geogrids, mainly at locations different than Wall 1, Station 289+00 (6/2/2008).



**Figure 3.3** Exposed geogrids, some damaged, and backfill loaded into a truck (6/2/2008).



**Figure 3.4 Collection of recovered (not at Wall 1, Station 289+00) geogrid for recycling (5/23/2008).**

The last strain gage reading was taken on 4/10/2008, before deconstruction of the wall began. The exhumation process started on 4/21/2008. Due to the excavation schedule, first the south embankment and then the north embankment were removed. DeIDOT provided essential assistance in coordinating the exhumation of the instrumented geogrids with the contractor. During exhumation, approximately 0.38 m (15 inches) of the 0.46 m (18 inches) of fill which was covering each geogrid was removed using an excavator. The remaining 0.06 m (3 inches) cover was then carefully removed using shovels in order not to damage the geogrid or strain gages - see Figures 3.5 through 3.8. That is, special care was taken at station 289+00 to exhume the geogrid layers without causing the damage to the geogrid that was observed at other locations due to the mechanized deconstruction process.

After recovery, the geogrids were labeled and transported to the Geotechnical Lab at the University of Delaware. Figures 3.9 and 3.10 show the site conditions after the removal of the south embankment. Due to the high consolidation settlement that occurred beneath the embankment (i.e., about 2.7 m (9 feet)), reinforcement layers 1 through 6, which were about 9 feet below grade, were not recovered as excavation stopped at elevation zero.



**Figure 3.5 Mechanical removal of approximately 0.38 m (15 inches) sand cover below the previous geogrid layer (5/28/2008).**



**Figure 3.6** Manual removal of the remaining 0.06 m (3 inches) of soil cover (5/28/2008).



**Figure 3.7** Careful recovery of exhumed geogrid (5/28/2008).



**Figure 3.8** Labeling a recovered strain gage instrumented geogrid panel (5/28/2008).



**Figure 3.9** View of site after the removal of the south embankment (6/27/2008).



**Figure 3.10 View of site after the removal of the south embankment (6/27/2008).**

### **3.2 Laboratory Measurement of Residual Strains**

The exhumed geogrids were transported to the University of Delaware Geotechnical Laboratory, where they were carefully examined and tested to learn more about the performance of the wall in the field. During this examination process, the change in length of the geogrids between two adjacent ribs was measured, and used to calculate the residual strain, as follows:

$$\epsilon_r = [(L_c - L_o) / L_o] * 100 \quad (1)$$

$L_c$  = Length measured after exhumation

$L_o$  = Nominal initial length as measured on virgin geogrid from the same lot as the one installed in the field.

$\epsilon_r$  = Residual Strain

To measure  $L_c$ , each geogrid panel was placed flat on a concrete floor as shown in Figure 3.11. The distance between transverse ribs in undamaged sections was measured using a 600 millimeters long digital caliper with an accuracy of 0.01 mm. There are about 70 apertures per panel between two adjacent ribs. About 10 measurements of each aperture were taken and the average value was used to define the representative  $L_c$  along the length of the panel. In this initial process, the readings were inconsistent, potentially implying that the measurement procedure is deficient.



**Figure 3.11** Recovered geogrid placed flat on concrete floor to measure the post-construction aperture sizes (5/25/2008).

Upon examination of the data from multiple panels, it was realized that stretching the aperture with the tips of the digital caliper to measure its length is an approach that does not yield consistent results. Also, the exhumed geogrid placed on the floor was sometimes curved rather than perfectly flat, potentially leading to measurement errors. To address these problems, the exhumed geogrid panels were hung from a frame and subjected to a small tension load, in an attempt to achieve more consistent aperture spacing. Each geogrid panel was hung vertically, with each aperture supported at either end of the panel. A load of approximately 0.41 kN/m (28 lb/ft) was applied to slightly stretch the geogrid. The aperture lengths were then measured, while the panel was subjected to the small tension load.

At first glance, this process appeared simple; however, it was discovered that the tensioning process had to be refined at each aperture so as to evenly distribute the hanging load. For instance, at first, two 1.8 m (6 foot long) wooden beams with 9 steel hooks in each beam were prepared. As shown in Figure 3.12, one of these wooden beams was placed on top of a steel frame and tightly secured with clamps. The geogrid was then placed over the steel hooks. As shown in Figure 3.13, a force of 0.41 kN/m (28 lb/ft) was applied by hooking the second wooden beam to the lower portion of the geogrid, and then hanging weights on either side of the lower wooden beam to apply a small tensioning load. Examination of the resulting data indicated that this setup did not work well, because the load was not distributed uniformly throughout the geogrid, and because there was the potential for damage to occur to the geogrid due to stress concentrations from the unevenly distributed hanging load.



**Figure 3.12** Geogrid panel is stretched by hanging it from a series of steel hooks (7/7/2008).



**Figure 3.13** Application of a 0.41 kN/m (28 lb/ft) force via a wooden beam and hooks (7/7/2008).



**Figure 3.14 General view of stretching process with the wooden beams (7/7/2008).**

Attempted refinement of this approach led to the use of directly clamped wooden beams on either side of the geogrid, in an attempt to “grab” and evenly hold the geogrid without applying the potentially damaging stress concentrations that were observed with the “hooking” method (Figures 3.15 and 3.16). This technique did not work efficiently. The geogrids were damaged at the top and at the bottom section of the panel. Also, it was difficult to hang weights on the bottom. Further refinement was attempted by using iron bars threaded through the geogrid apertures to hang the geogrid (Figures 3.17 and 3.18). As shown in Figures 3.17 and 3.18, this approach did not work well either, as it damaged the geogrid and did not allow for an accurate aperture length measurement with the caliper.



**Figure 3.15** The geogrid held and stretched by clamping its top between the wooden beam and the steel girder (7/10/2008).



**Figure 3.16** Modified system to apply load to the panel (7/10/2008).



**Figure 3.17** Iron bar threaded through the geogrid apertures used to hang the geogrid at the top (7/11/2008).



**Figure 3.18** Iron bar threaded through the geogrid apertures to apply load (7/11/2008).

In the final refinement, a flexible cable was used to attach the geogrid panel to the iron bar. This modification led to a tension load that was distributed uniformly across each geogrid panel. This type of connection did not damage the geogrid as did other techniques.



**Figure 3.19 Flexible cable attaching the geogrid panel to a fixed iron bar (7/17/2008).**



**Figure 3.20 Flexible cable attaching the geogrid panel to an iron bar having attached hanging weights (7/17/2008).**



**Figure 3.21 Overview of flexible cable attachment of the geogrid panel (7/17/2008).**

Using the flexible cable attachment approach, all exhumed geogrid panels with attached strain gages were measured for permanent deformation. A tension load of 0.41 kN/m (28 lb/ft) was used to induce an initial stretch and the resulting length ( $L_c$ ) between two adjacent ribs was measured using the aforementioned digital calipers.

Using the same approach, lengths ( $L_o$ ) between adjacent ribs of the virgin geogrid panels were also measured. Additionally, the geogrid manufacturer, Tensar International Corporation, Inc (Tensar), provided virgin nominal aperture lengths for the same model number geogrids; however, their values are not from the same lot of geogrids that were installed at IRIB. Table 3.1 shows both the virgin aperture lengths which were measured in the laboratory at UD and those that were obtained from Tensar. The data measured in the UD lab was used since the virgin geogrid panels that were tested were from the same lot as the ones installed at IRIB. Hence, such panels provide more relevant data for assessing the plastic strains.

**Table 3.1 Aperture lengths ( $L_o$ ) of the virgin geogrids**

		<b>UX1400HS</b>	<b>UX1500HS</b>	<b>UX1600HS</b>
LAB	avg	18.025	18.590	18.833
	min	17.951	18.474	18.741
	max	18.169	18.709	18.887
	percent difference min (%)	-0.41	-0.62	-0.49
	percent difference max (%)	0.80	0.64	0.29
Tensar	avg	18.134	18.380	18.495
	min	17.937	17.986	17.905
	max	18.370	18.891	19.164
	percent difference min (%)	-1.09	-2.14	-3.19
	percent difference max (%)	1.30	2.78	3.62

### **3.3 Simulating Field Loading History on Virgin Specimens to Establish the Relationships between Total Strain, Residual Strain & Tensile Load**

Upon initial analysis, the measured residual strain values ( $\epsilon_r$ ) were found to be much smaller than the strain values that were measured by strain gages in the field. This is a reasonable observation, as after exhumation the geogrid had undergone relaxation, thus not reflecting the strains in the geogrid in their in-service position (under load applied by the MSE wall).

The effects of thermal expansion due to temperature change between in-situ and lab conditions were considered. The formulation for thermal expansion/contraction is:

$$\lambda = L_o * C * \Delta t \tag{2}$$

$\lambda$  = change in length

$L_o$  = initial length (original length)

C = coefficient of linear thermal expansion (100 to 200 divided by 1,000,000 in/in/Celsius degrees),  
([http://www.stormcable.com/uploads/Thermal\\_expansion\\_data\\_table\\_tb06.pdf](http://www.stormcable.com/uploads/Thermal_expansion_data_table_tb06.pdf) & Thomas et al., 1990)

$\Delta t$  = change in temperature (Celsius- $C^\circ$ )

The maximum change in length ( $\lambda$ ) due to temperature change is calculated to range between 0.4572 mm (0.018 inches) to 0.9144 mm (0.036 inches) for a 457.2 mm (18 inches) geogrid strip, considering a maximum temperature change of 10  $C^\circ$  between the field and the lab. Consequently, since the change in length due to temperature changes between the field and the lab was negligible relative to measured field values, no temperature correction was applied to the data.

A testing procedure which simulates the history of construction at IRIB and considers both creep and relaxation was developed. The IRIB project followed a staged construction process and therefore, the field installed geogrid panels were loaded gradually as the construction continued for about 10 months. After removal of the embankment, the load was removed from the exhumed panels, meaning that stress relaxation occurred. Hence, it was necessary to simulate field conditions by loading the specimens, letting them undergo creep at each load increment, and when reaching a prescribed total strain value, unloading the geogrid specimens to allow relaxation to take place. Such simulation replicates the field history of staged loading, thus enabling one to calculate the relationship between total strain occurring in the field under load, the measured residual strain on the exhumed panels rendered, and the in-service load in the field. That is, this technique provides a “Rosetta Stone” to translate

the residual strains on exhumed specimens to the state of strain and stress in the embedded geogrids during in-service loading in the field.

### **3.3.1 Verification of Hypothesis Using Sacrificial Geogrid Specimens**

To verify whether the creep and stress relaxation values can be determined with confidence so as to simulate field conditions, testing of sacrificial specimens was conducted in the lab at the University of Delaware. To simulate loading (including creep) and relaxation, virgin specimens of Tensar UX1800HS were used. This type of geogrid was not installed in the section where specimens were retrieved and there were plenty of such specimens available to study in the lab. First, samples were prepared for testing – see Figure 3.22. The original lengths ( $L_o$ ) of the samples were measured. Each specimen was loaded in a tensile machine (Figure 3.23) and stretched up to 1%, 2%, 3% and 4% strain (Test Series A) with a speed of 1.27 mm/min. (0.05 in./min.). Once clamped in the loading machine, the specimens were loaded lightly (approximately 0.0018 kN) and the two outside strands of the geogrid were then cut, leaving the central strip to carry the tension load. Also, the same series of tests were repeated (Test Series B) to verify the consistency of the tests. After the target strain was achieved, the load was released. When relaxation was complete (about 14 days), each specimen's final length was measured. Figure 3.24 shows the results of these two test series (Test A & Test B).



**Figure 3.22** Tested sample after quick loading, during relaxation



**Figure 3.23 Loading frame and clamped sample.**

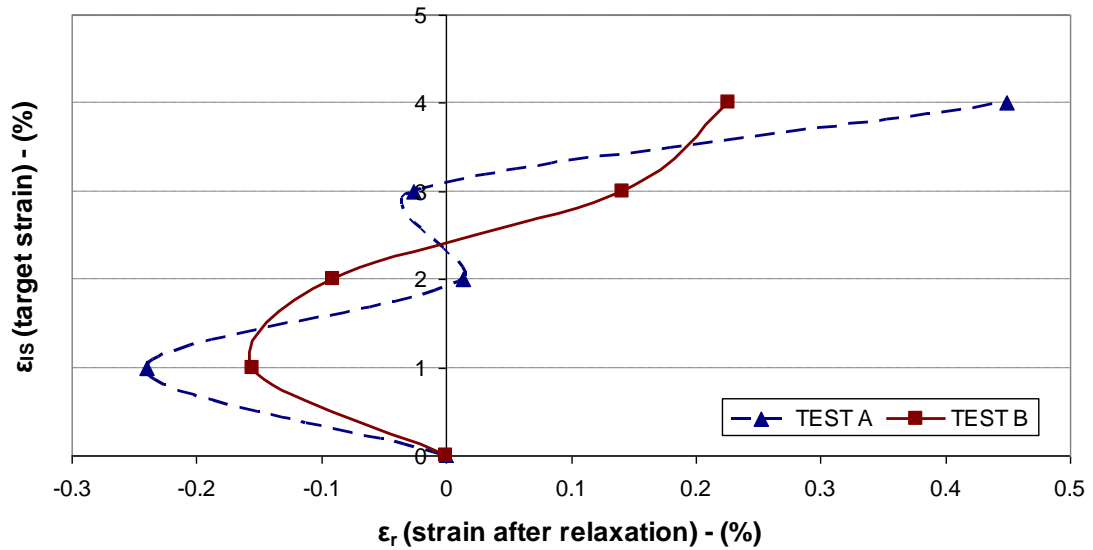


**Figure 3.24 Results of Test A & Test B attempting to simulate relaxation after inducing a history of rapid loading and unloading.**

These results were inconsistent, rendering implausible negative strain values, which indicated that the test procedure that was used was inadequate. The measured test results implied that the samples could have slipped at the machine grips during straining, causing the length measurements to be deficient. Hence, the simulation of field conditions was incomplete, potentially leading to paradoxical results (negative strains), as shown in Figure 3.24. Clearly, further refinement of the testing was needed.

### **3.3.2 Improved Sample Preparation for Creep-Relaxation Tests**

To reduce the potential for slippage of specimens when clamped in the loading frame jaws, and to develop a method for defining the length change more accurately, the sample preparation procedure was improved. Two small plates (130 mm by 90 mm) made of metal sheets were cut, sanded, and cleaned with acetone. Also, the tips of the geogrid samples were sanded to roughen its surface to ensure better bonding with epoxy glue. The ends of the geogrid sample were placed between the two metal sheets, coated with epoxy, and clamped tightly to each other with screws. In addition to sanding, extra holes were drilled in the sheet metal for better bonding with the geogrid specimen as Epoxy squeezed through these holes – see Figure 3.28. To keep the epoxy at its liquid state between the metal sheets, the edges of the two metal sheets were covered with tape.

The screws connecting the two sheet metals plates also served as a consistent benchmark for the length measurement of the tested specimen. That is, a clear and stable point for length measurements (i.e., a consistent benchmark), enabled one to measure changes in the length of the specimens accurately between the designated screws. This process is shown in detail in Figures 3.25 through 3.28.



Figure 3.25 Geogrid sample and perforated sheet metals plates before gluing.



Figure 3.26 The geogrid sample and the sheet metal plates sanded and cleaned before gluing.



**Figure 3.27** Nearly all the parts of the clamps are in place before placing epoxy.



**Figure 3.28** The glued specimen clamped with epoxy and screws.

The clamps made of glued sheet metal plates on either side of the geogrid sample were attached to the loading frame using the components shown in Figure 3.29. This fixture was then connected to the loading frame and the plate via separate pins. The modification to the test setup and the resulting test procedure are shown in Figures 3.29 through 3.31.



**Figure 3.29** Fixture to connect the sheet metal clamp to the loading frame.



**Figure 3.30** The bottom part of the clamping fixture connected to the loading frame.



**Figure 3.31** Sample during loading – note that outer geogrids have been cut.

In order to check if there was slippage at the specimen boundaries, some of the samples were taken apart after testing. It was concluded that the bonding of this technique prevented slippage of the specimen from its clamping fixtures. Figure 3.32 shows that the grid and the epoxy were not damaged within the clamping area and that there were no signs of slippage.



**Figure 3.32** Post-test examination of the clamping fixture to verify whether slippage occurred.

### **3.3.3 Modified Simulation of Creep-Relaxation Tests Using Modified Samples**

Using sacrificial (UX1800HS) geogrid samples prepared using the modified approach described in 3.3.2; several loading-unloading tests were conducted. Some of the results of these trial tests are represented in Figure 3.33. Test #4 was performed at a speed of 0.254 mm/min. (0.01 in/min.) using the loading frame, and was stretched up to 3% and then left for relaxation. The measured residual strain (strain after relaxation) of this test was about 0.9%.

Tests #2, #3 and #5 were performed at different rates of loading to investigate the material response to applied load rate using the loading frame. The three specimens were each stretched to around 6% strain. It is apparent that the maximum load applied was different for different loading rates; this indicates that the history of loading and rate of load application is important. The load at 6% strain in these three tests changed between 78.81 kN/m (5400 lb/ft) to 95.59 kN/m (6550 lb/ft), very close to the value specified in Tensar's product specifications for UX1800HS. Tensar's specified tensile strength at 5% strain with a loading speed of 10% strain per minute is 95.01 kN/m (6510 lb/ft).

The strain after relaxation (residual strain) was different for the three specimens (tests #2, #3 & #5) that were stretched to same percent strain (6%) at different rates of loading (Figure 3.33). These three tests implied that the loading rate is an important factor which affects the total strain, residual strain, and the associated load relationship. This is not surprising, considering that polymeric materials such as geogrids tend to creep under constant applied load. The lowest possible loading rate for the loading machine used at the University of Delaware was 0.254 mm/min (0.01 in/min.) and the loading machine was not capable to let the sample creep freely with

the final load. These limitations in loading rate capability were unacceptable when trying to simulate the field loading rate and its effects on the residual strain.

It can be concluded that the stress history of loading of polymeric materials is very important; e.g., loading rate and creep play a major role. It appears that rapid loading (as was performed for Tests #2, #3, #4 and #5) does not allow the specimens to undergo creep. These tests indicated that the performance of the samples with the metal clamps was okay but the testing method was deficient to simulate the IRIB project loading-unloading sequence. Hence, an alternative approach to generate the “Rosetta Stone” was needed so as to be able to correlate the residual strains on exhumed specimens with the in-situ total strains and loads.

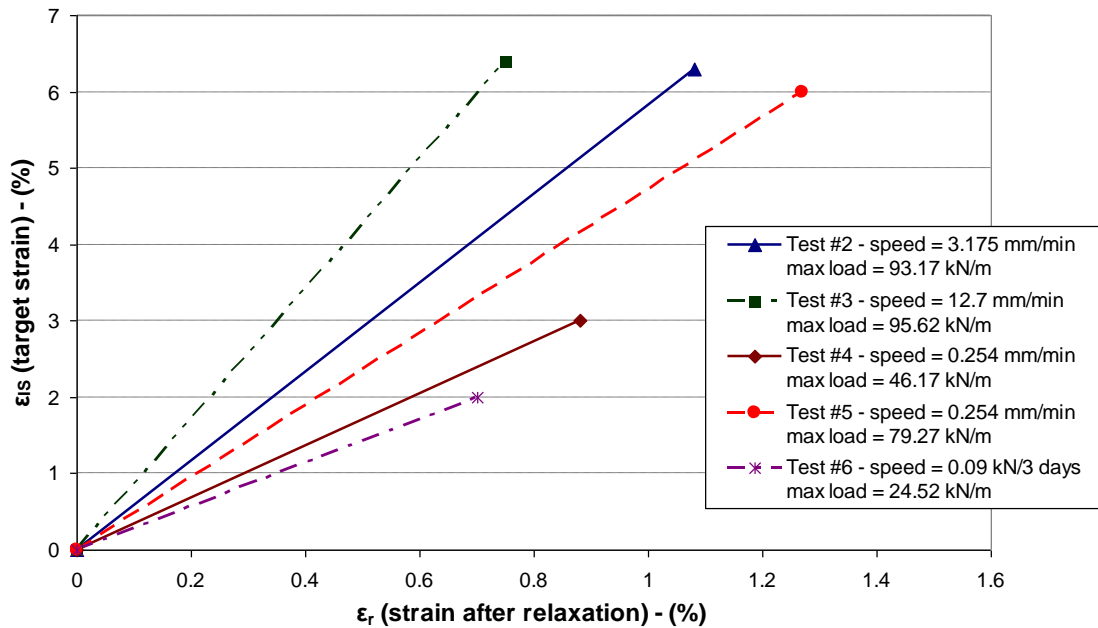


**Figure 3.33 Tests attempting to establish the relationship between total strain, residual strain and load.**

The inadequacy of the loading frame necessitated that the tests be set up outside the loading machine, using manual methods. As a first try (Test #6) one sample was prepared as described in part 3.3.2. The sample was then hung on a steel frame and loaded manually using dead weights. This type of manual stress-controlled testing procedure provides excellent control of the incremental loading process, thus providing a better simulation of field loading conditions. Also, for each load increment, creep was allowed to develop, similar to field conditions. Finally, the manual loading and unloading process that was used enables easy measurement of accurate creep and relaxation. This method is described in more detail in Section 3.3.4

The result of Test #6 is also shown in Figure 3.33, and is an example of a manually loaded test where stress was controlled to achieve full creep and relaxation. The load was applied in increments of 0.09 kN (20 lb) per 3 days, in order to simulate the staged construction process. Also, during Test 6, when the specimen had reached the target strain value of 2%, the load was sustained so as to allow creep to develop. When creep practically ceased, the load was released and the relaxation took place. It took about 14 days for creep to terminate and about 10 days for relaxation to terminate. For such duration of tests it is clear that usage of a mechanical loading frame is not feasible.

### **3.3.4 Refined Testing Approach Used to Simulate Field Loading History**

At station 289+00, layers 7 through 23 were exhumed and layers 1 through 6 were left in place, as they are below grade. The exhumed geogrid panels indicate that layers 16 through 23 were UX1400HS, layers 11 through 15 were UX1500HS, and layers 7 through 10 were UX1600HS. Hence, characterizing only three types of geogrids was needed: UX1400HS, UX1500HS and UX1600HS.

Four samples of each different type of geogrid (12 samples in total) were prepared as described in section 3.3.2. Each specimen was hung on a steel frame with a loading hanger being attached to the steel clamp at the bottom part of the samples as shown in Figures 3.34 through 3.36 (the loading hanger used is the same as what is commonly used to hang dead weights for use in incremental consolidation tests). Once each specimen was hung on the steel frame and the loading arm was attached, the specimens were loaded with 0.09 kN (20 lb) which corresponds to (i.e. 14 strips in 1 foot) 4.1 kN/m (280 lb/ft) (first step loading) and two outside strands of the geogrid were then cut, leaving the central strip to carry the tension load. Each specimen was

loaded up to about 1%, 2%, 3% or 4% by hanging weights on to the loading arm to gradually simulate the field loading conditions. The average loading increments were 20 lb (280 lb/ft) (4.1 kN/m) every 3 days. When it was observed that a specimen had approximately reached the target strain value, it was subjected to sustained load for about 14 days so as to allow for full creep development (this is an approximate indicator value of “full creep” development, as creep is often an asymptotic time-dependent process that may never be fully “complete”). A creep period of 20 days was used for samples which were loaded to the higher loads (i.e., those rendering 4% strain). When it was observed that creep was completed (i.e. all observable/recordable movements had ceased), the specimen was unloaded (in one step, not in stages) for the relaxation process. Such unloading approximately replicated the field process: first approximately full creep was allowed to develop and then relatively rapid unloading occurred due to removal of backfill. The samples were allowed to complete the relaxation process over the course of approximately 10 days. During the relaxation process, a load of 2 lbs, which was equal to 28 lb/ft (0.41 kN/m) – the same stretching load which was used to stretch the exhumed geogrid panels, was applied to keep the specimens straight and thus enable accurate length measurements.

During these tests, length measurements were performed using a 600 mm long digital caliper and data were recorded daily. The creep and relaxation test results are presented in detail in Chapter 4. In Figure 3.34, the loaded specimens on the right are UX1600HS geogrids loaded to strains of 3% and 4%. The ones on the left are UX1500HS geogrids undergoing relaxation after being unloaded to a prescribed total strain.



**Figure 3.34** Loaded and unloaded samples for creep and relaxation tests.

Compared with the cut strands shown in Figure 3.35, the elongation of the loaded strand is apparent. Figure 3.36 shows the measurement of length using the digital caliper. In each case, length measurements were taken between the tips of the screws, which served as reliable and consistent benchmarks.



**Figure 3.35** Loaded specimen (note the gap between the two parts of the cut strands; it signify the elongation of the specimen after being subjected to load)



**Figure 3.36** Measurement of length using a digital caliper.

## Chapter 4

### RESULTS OF CREEP-RELAXATION TESTS

For each of the three types of geogrids exhumed from Wall 1 at Station 289+00 (type UX1400HS, UX1500HS and UX1600HS), four samples were prepared using virgin geogrids and tested using the “refined testing approach” described in Chapter 3. The prepared samples were tested using a methodology that simulated the field loading history, in order to establish relationships between total strain, residual strain and tension load. The results of these tests are presented below.

#### 4.1 Testing Results of UX1400HS, UX1500HS & UX1600HS Geogrids

Five sets of graphs were constructed for each type of geogrid that was tested. The first two sets of graphs were constructed while conducting the tests to ascertain that total strain measurements had stabilized in response to each applied load step, and to examine the relationship between different test results. The first set of graphs (Figures 4.1 through 4.3) shows the percent changes in total strain ( $\epsilon_t$ ) versus time in days, in response to the applied load increments. Total strain here indicates the summation of developed strain due to the applied load superimposed by the creep strain occurring under that sustained load. For each geogrid, the graphs include four different curves which correspond to 4 different loading levels; i.e. loading level needed to reach about total strain of about 1%, 2%, 3% and 4%. As described before, each specimen was loaded by increments of about 0.09 kN (20 pounds), each loading level sustained for at least 3 days so as to allow creep to develop, and when the target

total strain was approximately achieved, the load was removed. It noted that before unloading, the total strain that developed included a creep component. The asymptotic portions of the curves demonstrate the evolution of creep. In general the results are very consistent. As seen, the same loading steps applied to different specimens of the same type are overlapping as long as the sustained load is in the same magnitude. Once larger load increments are applied, the subsequent development of total strain appears reasonable when one considers the measured previous values.

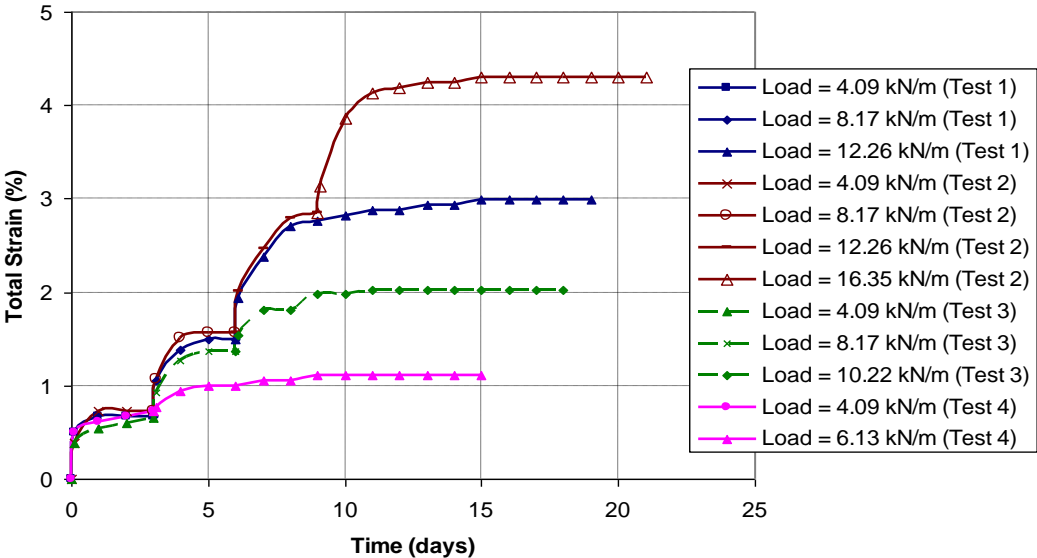


**Figure 4.1 Total strain due to various sustained load increments (UX1400HS).**

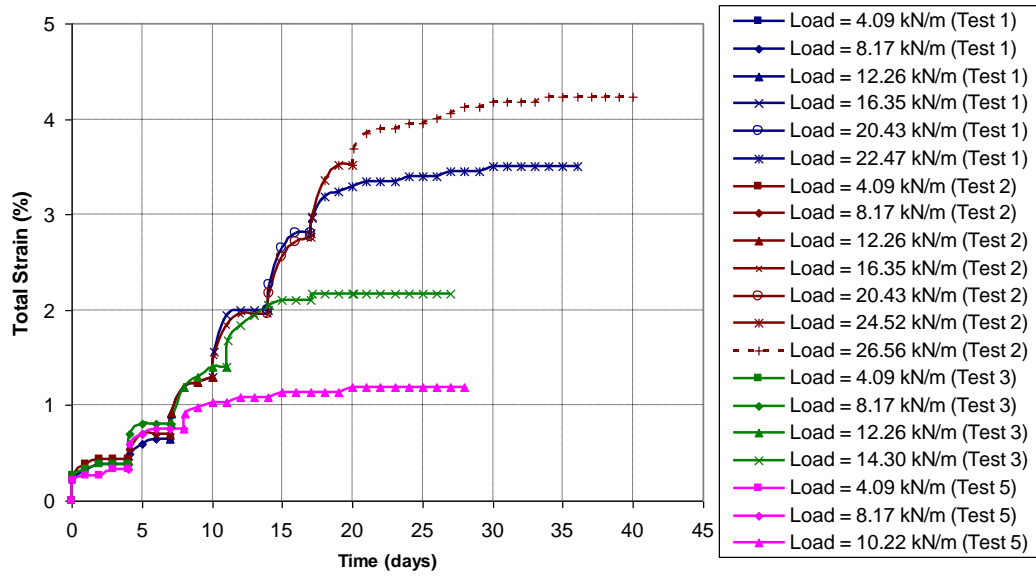


Figure 4.2 Total strain due to various sustained load increments (UX1500HS).

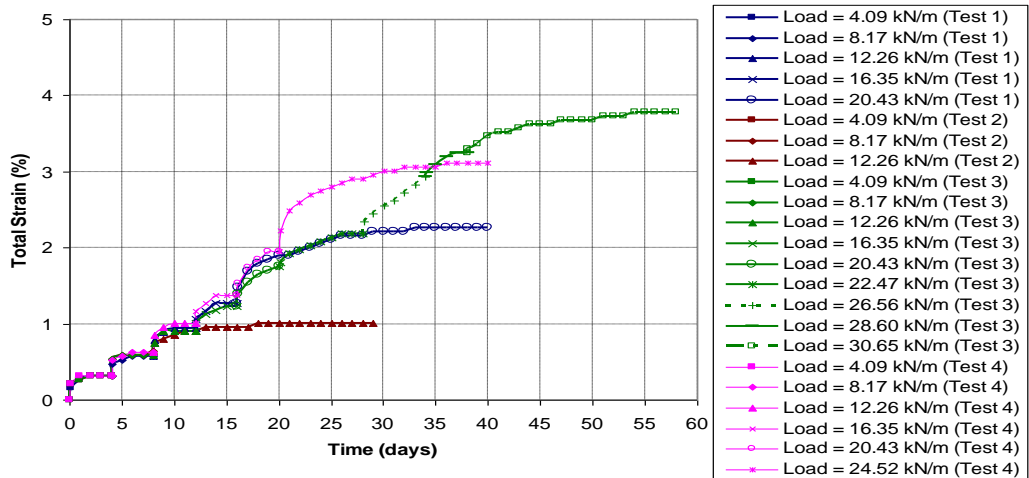
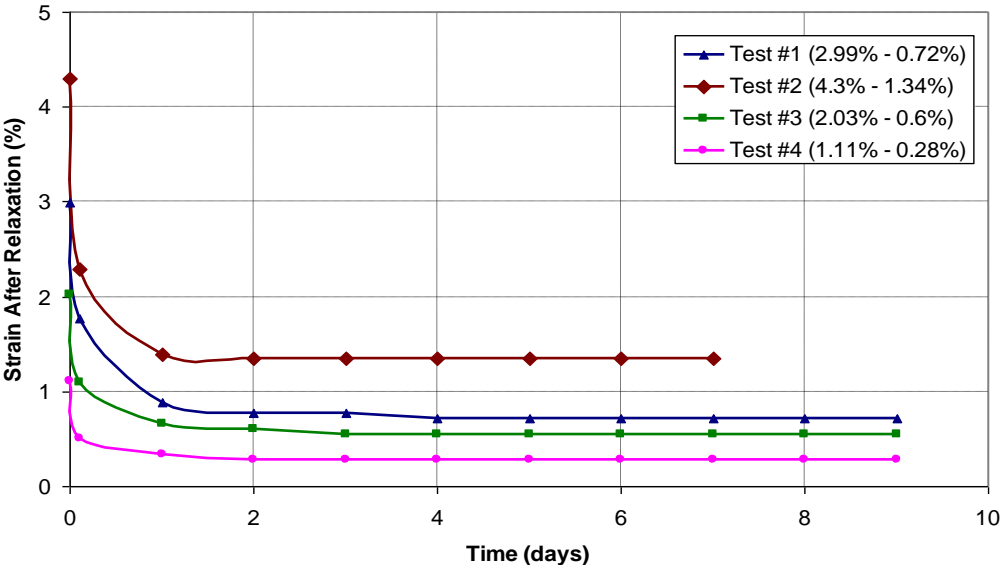


Figure 4.3 Total strain due to various sustained load increments (UX1600HS).

The second set of graphs (Figures 4.4 through 4.6) presents the relaxation process following the unloading of each specimen. The data shown are the measured residual strains versus time, with the curves starting from the total strain which was reached during the last sustained loading phase. The asymptotic portions of the curves indicate the completion of the relaxation process. The residual strain ( $\epsilon_r$ ) value is the measured strain at the end of relaxation. The numerical values of the residual strains versus the respective total strains that were measured prior to unloading are provided in the legend of each graph. As shown, completion of the creep process took longer for UX1500HS and UX1600HS than for UX1400HS geogrid, as these specimens were loaded to higher loads due to their stiffer structural cross-sectional properties.



**Figure 4.4 Residual strain developments during relaxation (UX1400HS).**

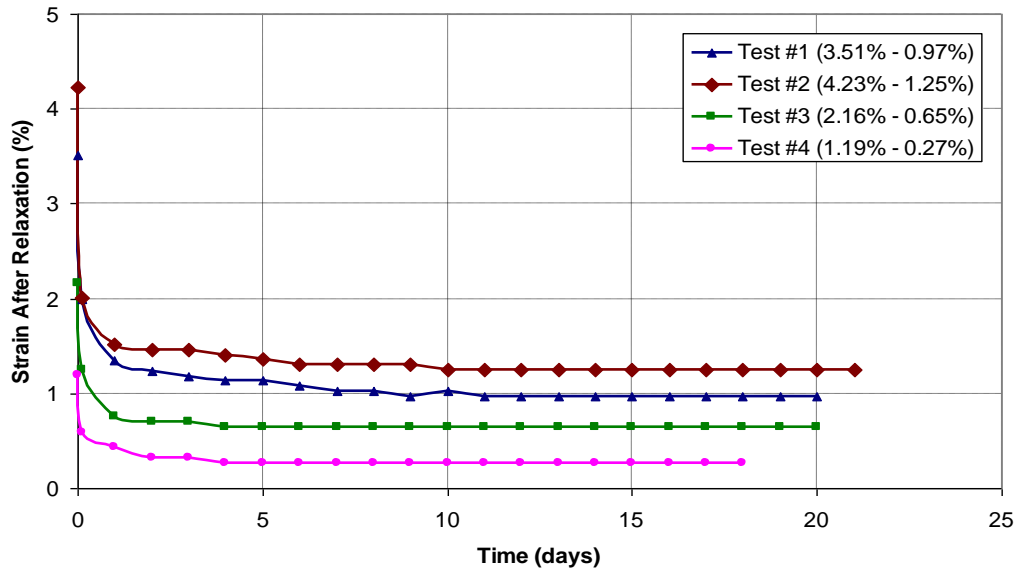


Figure 4.5 Residual strain developments during relaxation (UX1500HS).

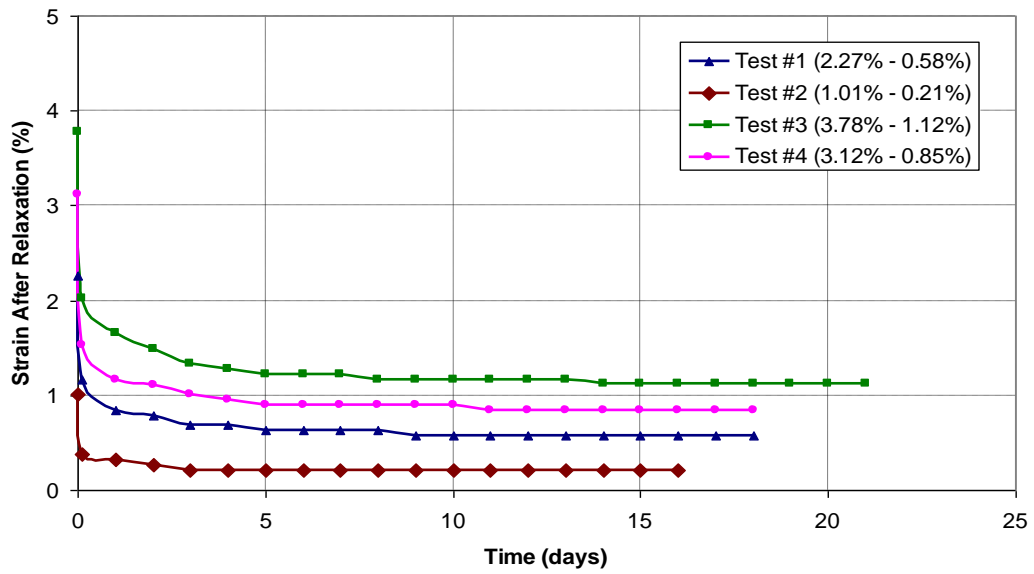
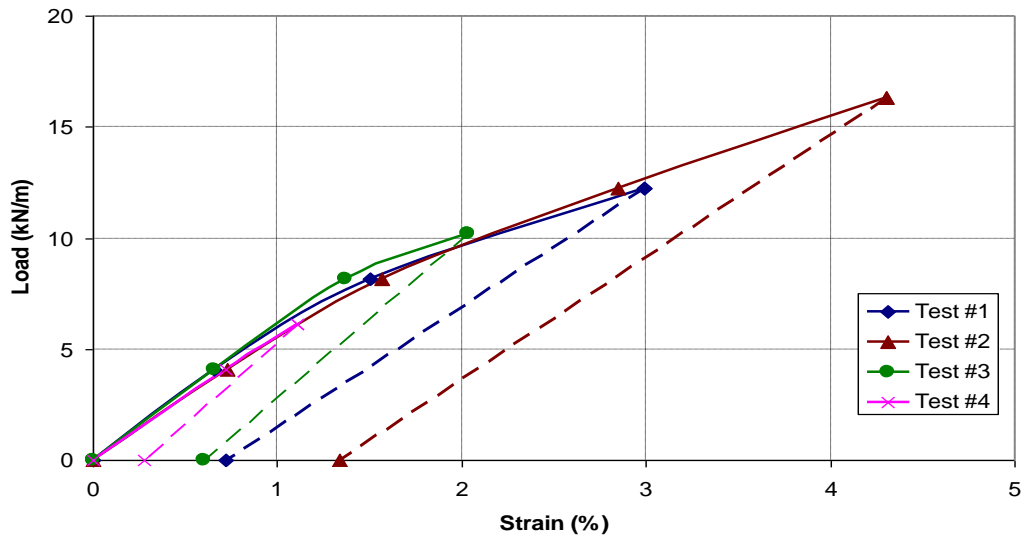
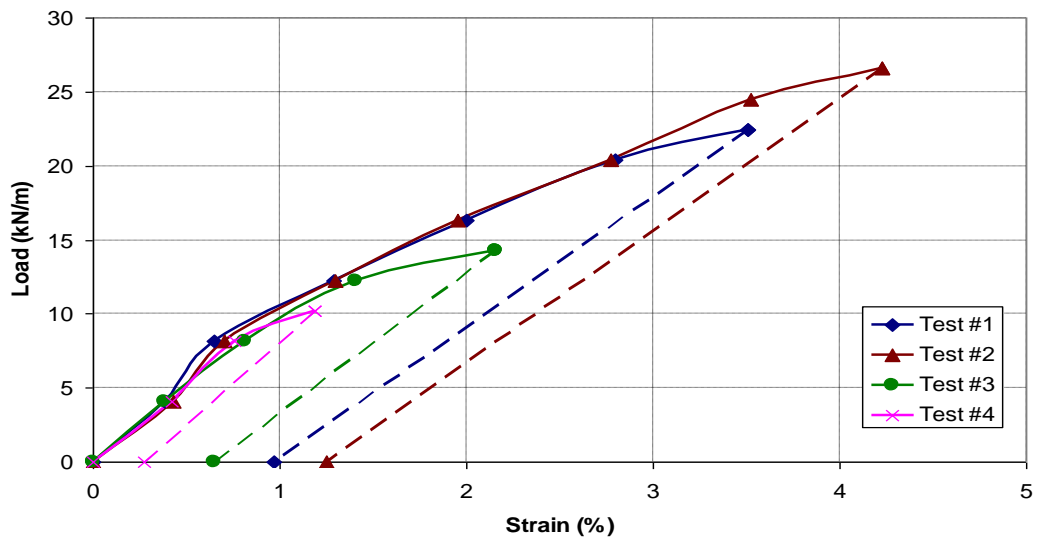


Figure 4.6 Residual strain developments during relaxation (UX1600HS).

Figures 4.7 through 4.9 were prepared using the previous results. These figures show the relationships between the sustained load and the total strain developed in the geogrid. They also show the final strain after relaxation, the residual strain as one would measure after exhumation and proper relaxation. The end of the solid lines presents the final applied load in a particular test and the corresponding total strain. The dashed lines in the graph start at the maximum total strain and extend to the relaxed strain value following unloading. Time is not shown in these figures; only the final values of strains or loads. In general, the results are very consistent. As shown in Figures 4.7 through 4.9, the loading and the corresponding total strain for each specimen coincide with those for other specimens (as long as the sustained load is in the same range). The dashed lines which represent unloading to residual strain are nearly parallel to each other.



**Figure 4.7** Sustained force versus total strain and residual strain after relaxation (UX1400HS).



**Figure 4.8** Sustained force versus total strain and residual strain after relaxation (UX1500HS).

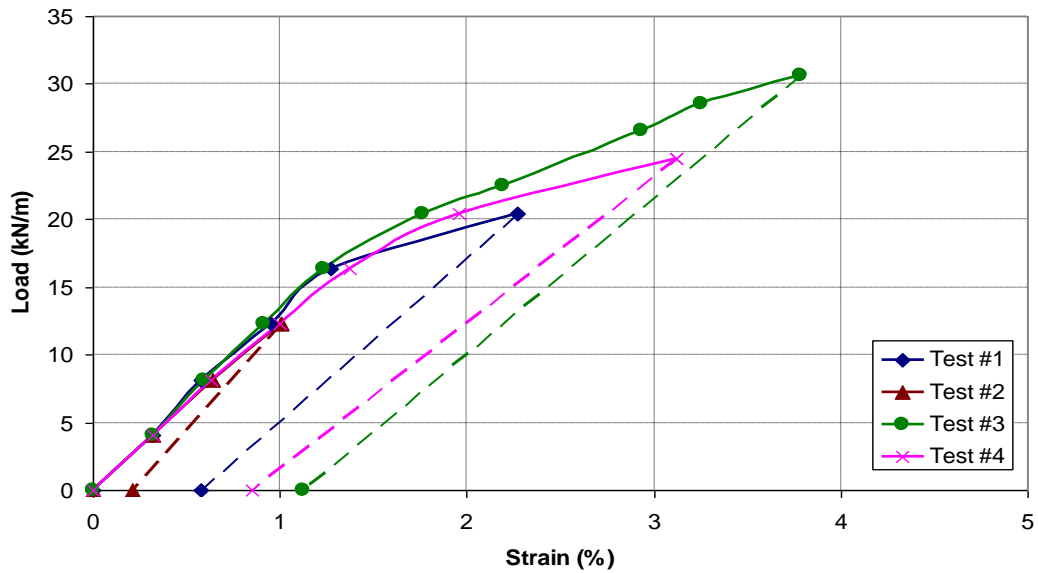


**Figure 4.9 Sustained force versus total strain and residual strain after relaxation (UX1600HS).**

The fourth sets of graphs (Figures 4.10 through 4.12) show the percent total strain versus percent strain after relaxation (residual strain). Using these graphs, the measured percent residual strain (i.e. the strains which are measured after exhumation) can be transformed into percent total strain in the field. A 2<sup>nd</sup> order polynomial equation was developed for UX1400HS & UX1500HS and a 3<sup>rd</sup> order polynomial equation was developed for UX1600HS to determine the total strain as a function of the residual strain. The residual strain served as the independent variable,  $\epsilon_r$ , in the polynomial equation. Solving this equation yields the insitu total strain ( $\epsilon_t$ ) in percent. Total strains obtained from Equation 4.1 for the UX1400HS geogrid,

Equation 4.2 for the UX1500HS geogrid, and Equation 4.3 for the UX1600HS geogrid are:

$$\text{(UX1400HS) Total Strain } (\epsilon_t)\text{-(\%)} = -1.0635 \epsilon_r^2 + 4.698 \epsilon_r - 0.0563 \quad (4.1)$$

$$\text{(UX1500HS) Total Strain } (\epsilon_t)\text{-(\%)} = -0.2705 \epsilon_r^2 + 3.6989 \epsilon_r + 0.0573 \quad (4.2)$$

$$\text{(UX1600HS) Total Strain } (\epsilon_t)\text{-(\%)} = 0.7158 \epsilon_r^3 - 2.3176 \epsilon_r^2 + 5.0706 \epsilon_r + 0.0114 \quad (4.3)$$

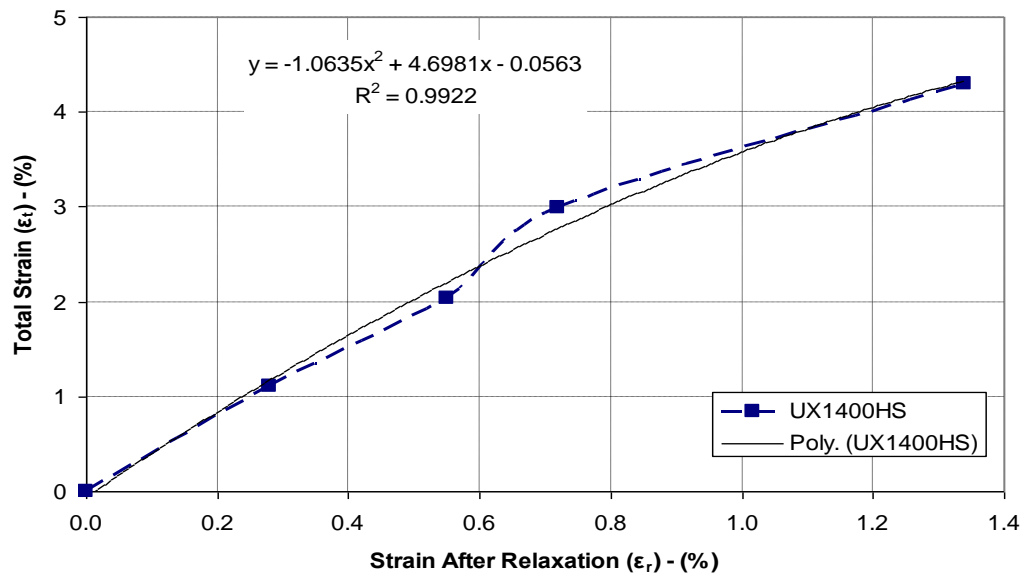


**Figure 4.10** Curve-fitted second order polynomial relating the measured residual strain to the in situ geogrid total strain (UX1400HS).

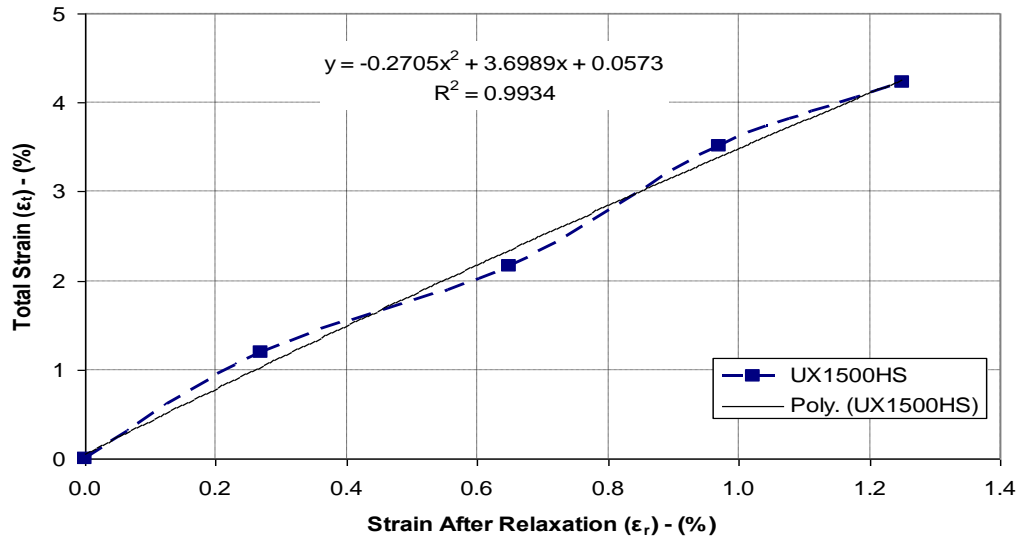


**Figure 4.11** Curve-fitted second order polynomial relating the measured residual strain to the in situ geogrid total strain (UX1500HS).

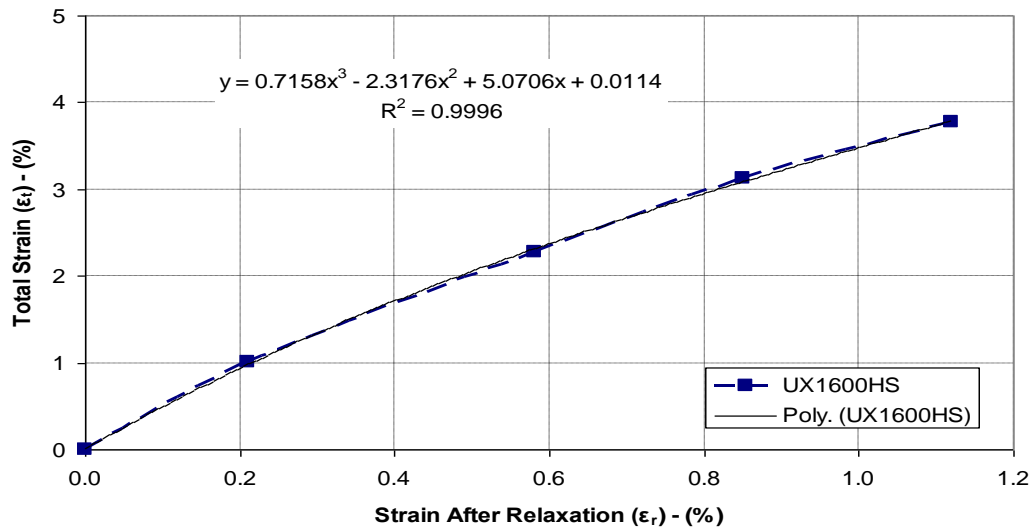


**Figure 4.12** Curve-fitted third order polynomial relating the measured residual strain to the insitu geogrid total strain (UX1600HS).

Finally, Figures 4.13 through 4.15 characterize the load versus total strain response for each of the three geogrid types. Each graph includes four curves for the load versus total strain ( $\epsilon_t$ ), as well as the average curve for load versus total strain. Using the average curves, the total strain in the field can be inferred from residual strain measurements, and can then be transformed into the corresponding total load in the geogrid reinforcement in the field. A 3<sup>rd</sup> order polynomial equation was developed for each curve to determine the load corresponding to total strain. The total strain served as the independent variable,  $\epsilon_t$ , in the polynomial equation developed from the average load versus total strain curve. Solving this equation yields the load in the geogrid. Loads (tensile strengths) are presented in Equation 4.4 for the UX1400HS geogrid, Equation 4.5 for the UX1500HS geogrid, and Equation 4.6 for the UX1600HS geogrid:

$$\text{(UX1400HS) Load (kN/m)} = 0.1483 \epsilon_t^3 - 1.434 \epsilon_t^2 + 7.2412 \epsilon_t - 0.107 \quad (4.4)$$

$$\text{(UX1500HS) Load (kN/m)} = 0.1771 \epsilon_t^3 - 2.0458 \epsilon_t^2 + 11.815 \epsilon_t - 0.0089 \quad (4.5)$$

$$\text{(UX1600HS) Load (kN/m)} = 0.4245 \epsilon_t^3 - 3.7975 \epsilon_t^2 + 16.438 \epsilon_t - 0.35 \quad (4.6)$$

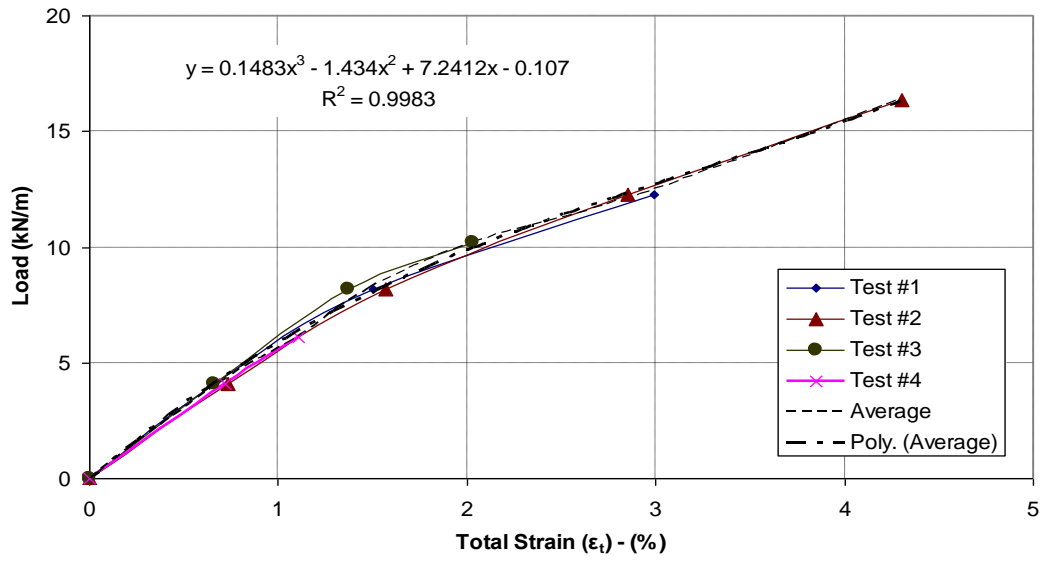


**Figure 4.13 Load versus total strain (UX1400HS).**

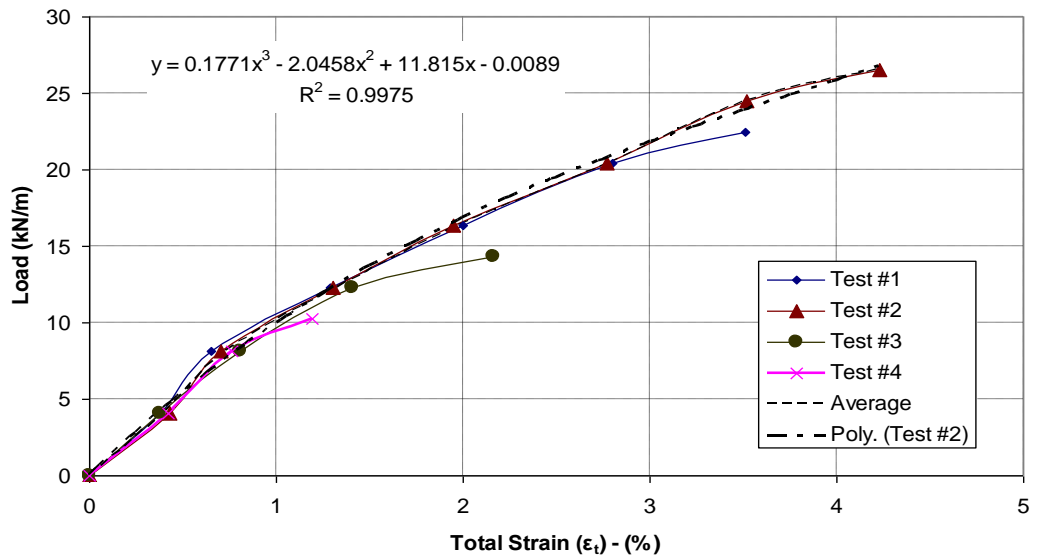


**Figure 4.14 Load versus total strain (UX1500HS).**

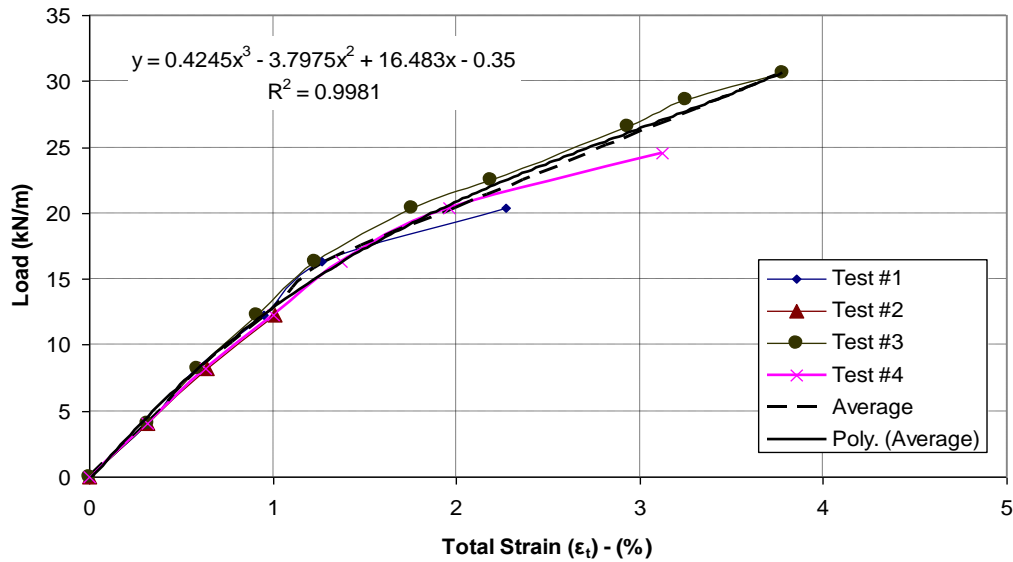


**Figure 4.15 Load versus total strain (UX1600HS).**

## 4.2 Summary of Test Results

The curve-fitted results of total strain versus residual strain for the three different types of geogrid are summarized in Figure 4.16. After measuring the residual strain, the in situ total strain can be calculated either using this chart (Figure 4.16) or using Equations 4.1 through 4.3. As shown in Figure 4.16, it is clear that the curves are very close to each other. That is, it is interesting to note that the three different types of geogrid exhibit practically the same total strain versus residual strain behavior. However, this does not imply that the corresponding field loads exhibit the same behavior, as the load carrying capacity of the geogrid at a given strain is related

to the stiffness of the material, implying that the same strain will correspond to different loads for different geogrid types.

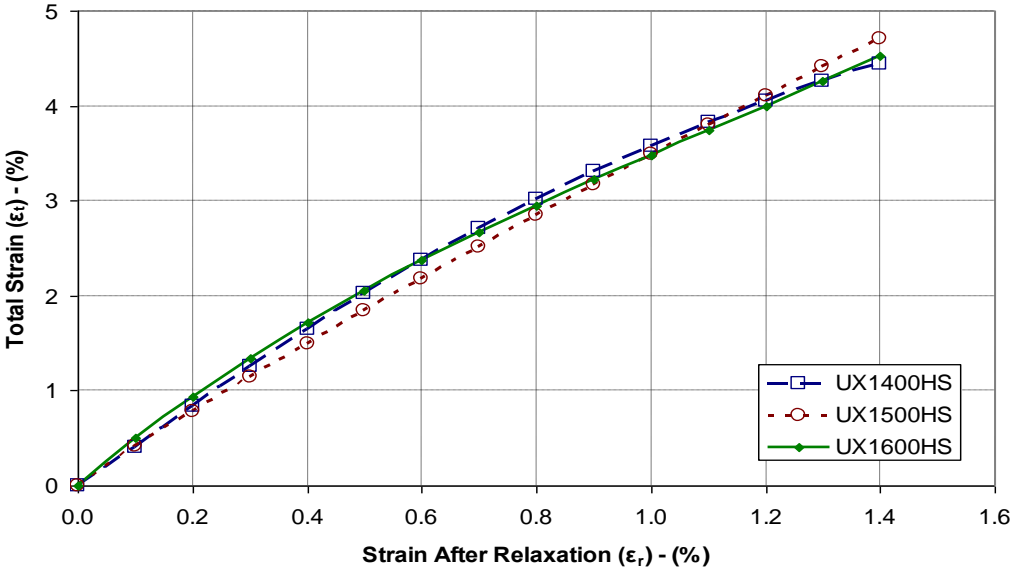


**Figure 4.16 Summary chart of total strain versus residual strain.**

The curve-fitted results of load versus total strain are summarized in Figure 4.17. Clearly, the same strain values for the different geogrids correspond to different tensile loads, as discussed above. After determination of the total strain from the measured residual strain, the predicted in situ geogrid load can be calculated either following this chart (Figure 4.17) or using Equations 4.4 through 4.6.

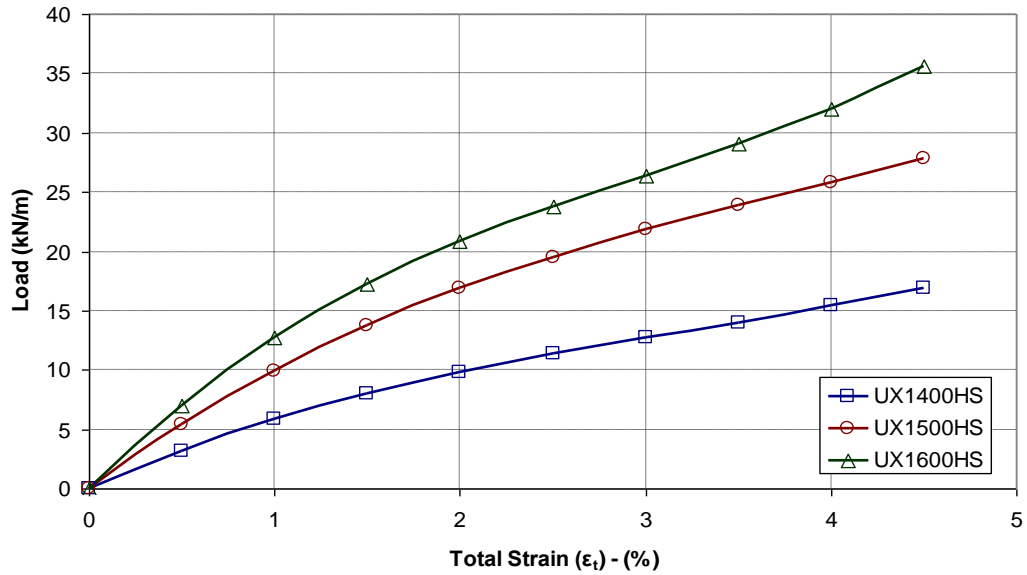


**Figure 4.17 Summary chart of load versus total strain.**

The average residual strain values were determined from the exhumed geogrids as described in Chapter 3 and the results for the in situ wall at the IRIB are presented in Chapter 5. The average residual strain values were converted to total strain values (i.e. which correspond to the strain values in the field) using Figure 4.16. Once the average total strain values were defined, the insitu loads were calculated using Figure 4.17. The interpretation of results is presented in Chapter 5.

## Chapter 5

### INTERPRETATION OF MEASURED RESIDUAL STRAINS ON EXHUMED GEOGRIDS

#### 5.1 Measured Residual Strains

Strain gages were installed on geogrid panels and monitored by Scott A. Berkheimer (2007). Upon Berkheimer's graduation, the Author continued with gage monitoring until the removal of the embankment. Resistance readings of the gages were taken on site and then converted to strains and forces based on calibration factors established by Berkheimer (2007).

As the embankment was removed, the instrumented geogrids were exhumed and transferred to University of Delaware (Chapter 3). The length changes of the exhumed geogrids were measured and converted to the corresponding strain values. These strains are the residual strains (the strains after relaxation), as described in Chapter 3. The conversion from aperture lengths to strain values utilized the average virgin aperture lengths shown in Table 3.1, Chapter 3. It should be noted that inherent variability in the average virgin aperture lengths that were used to calculate the average strain values can lead to variations in the actual total strains within a range of about  $\pm 1\%$  strain. As an example, an estimated strain value of 3% may actually be anywhere between 2% and 4% since the installed aperture length used to calculate the residual strain may vary a little from the average value used to calculate the strains. The variation of initial aperture lengths is shown in Table 3.1.

The resulting residual strain values were then converted to the total strain values (i.e. in-situ strain values before the removal of the embankment) and to tensile force using the charts which were presented in Chapter 4.

In addition to assessing the residual strain of the exhumed geogrid panels, the strain gages attached prior to field installation were examined for each of the instrumented panels. This was an important opportunity to conduct such an examination, as many of the gages stopped functioning over time and one could only speculate as to the reasons for this poor performance. Also, even those gages that “performed well” could be assessed to examine the physical condition of the gage (whether they were intact, still well-bonded to the geogrid, etc.).

For each instrumented geogrid layer, 3 sets of figures and a table were prepared to summarize the measured and back calculated data (i.e. strain and force distribution) as well as the condition of each strain gage after exhumation. Each set of table and figures corresponds to an exhumed geogrid panel; these sets are presented in Sections 5.1.1 through 5.1.9. For each geogrid layer, the first figure presents the strain gages output as measured in-situ (the last field measured value of strain is shown), residual (relaxed) strains measured in the laboratory after exhumation, and back calculated field (in-situ) strains based on interpretation of the relaxed strains using the calibration charts developed in Chapter 4. Also, a table which includes information about the observed condition of the exhumed strain gages is presented for each layer. Following the tables shown are figures displaying the development of recorded strain extending from installation to exhumation. Finally, shown are figures of the force distribution along the instrumented geogrid layer that corresponds to the total strains (calculated using the approach described in Chapter 4).

It is noted that some of the geogrid panels were partially damaged during excavation. Data from these damaged parts are not presented. Some of the strain gages stopped functioning early; the last day these gages produced a reading is stated in the legends of the graphs.

As to timelines, construction of station 289+00 (where field monitoring was conducted) started on 02/20/2006 and it was completed on 12/01/2006. Due to the excessive settlements, the owner (DelDOT) decided to remove the embankment. The removal started on 04/20/2008 and was completed three months later.

### 5.1.1 Layer # 23 (UX1400HS)

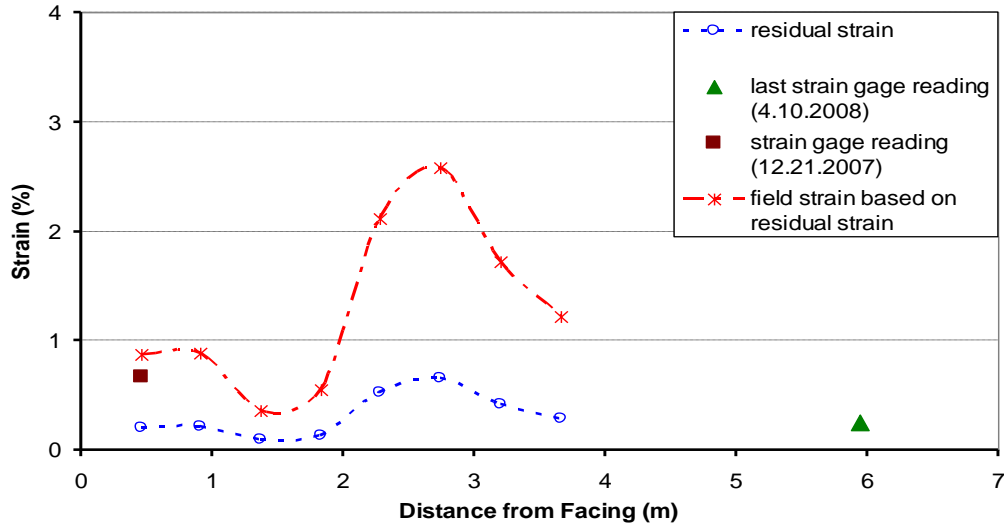
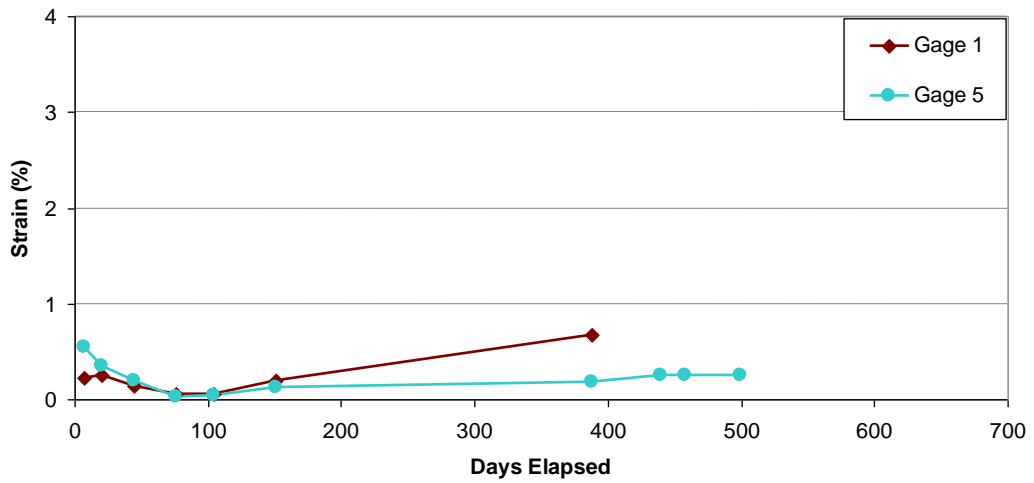


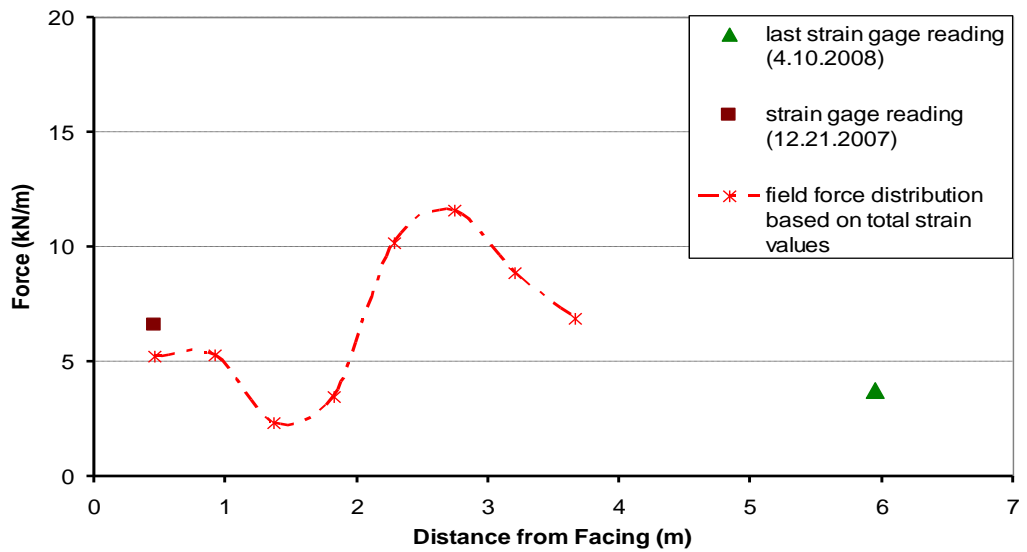
Figure 5.1 Strain distribution of the exhumed geogrid (Layer #23).

Table 5.1 Strain gage observed condition (Layer #23)

Layer 23	last reading	after excavation	Observation
Gage # 1	0.67 (12.21.07)	-	The gage system seems solid. Probably inadequate gage installation because it debonded from the grid as a whole. This gage stopped working by 12.21.2007.
Gage # 2	0.0 (4.10.08)	-	Has not worked since installation. Could be due to cable strain gage connection failure.
Gage # 3	0.0 (4.10.08)	-	Has not worked since installation. Could be due to cable strain gage connection failure.
Gage # 4	-	-	Has not worked since installation. Gage not found, probably detached during removal of the geogrid.
Gage # 5	0.26 (4.10.08)	-	Gage not found, probably detached during removal of the geogrid. Last reading was taken on 4.10.2008.



**Figure 5.2** Field strain gage measurements from the installation date to the removal date (end of construction coincides with installation of this final layer 12/01/2006) (modified after Berkheimer, 2007) (Layer #23).



**Figure 5.3** Tensile force distribution based on total strain values (Layer #23)

### 5.1.2 Layer # 22 (UX1400HS)

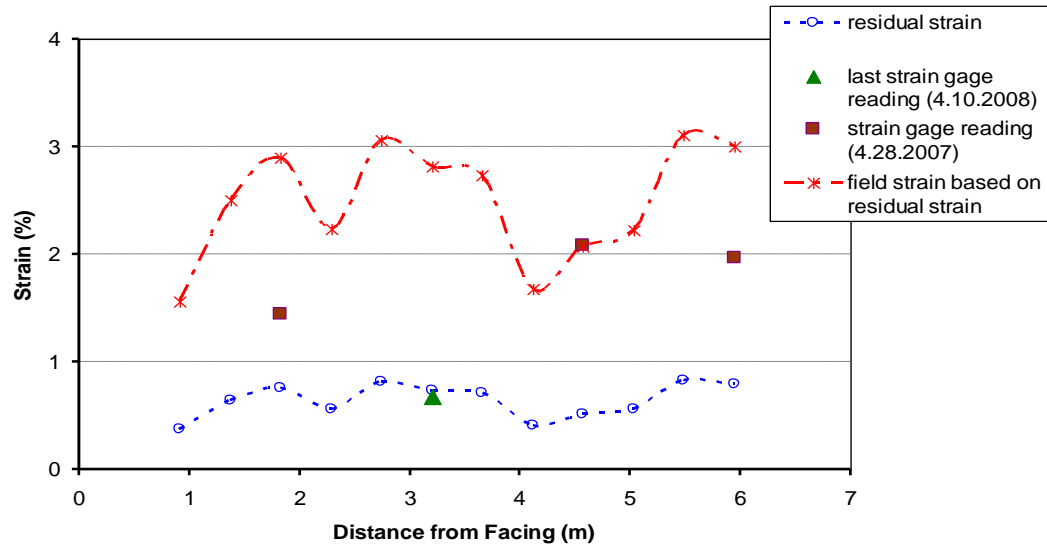
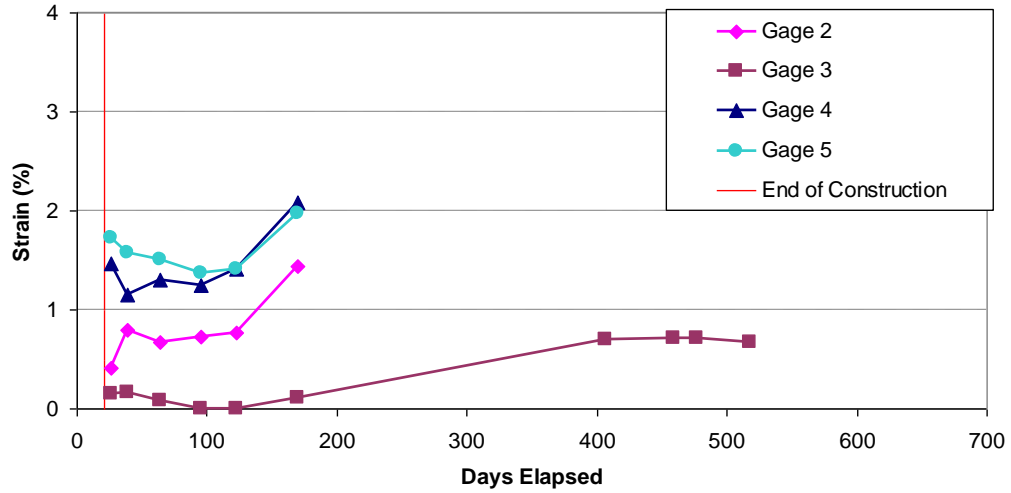


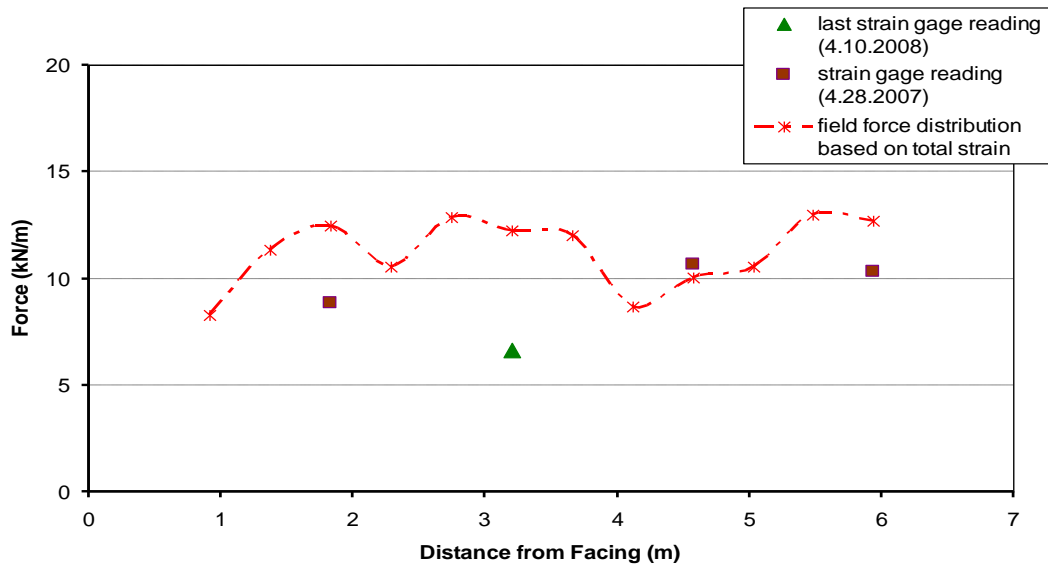
Figure 5.4 Strain distribution of the exhumed geogrid (Layer #22).

Table 5.2 Strain gage observed condition (Layer #22)

Layer 22	last reading	after excavation	Observation
Gage # 1	-	-	Has not worked since installation. Could be due to cable strain gage connection failure.
Gage # 2	1.44 (4.28.07)	-	Well bonded. This gage stopped working by 4.28.2007.
Gage # 3	0.68 (4.10.08)	-	Well bonded. Last reading was taken on 4.10.2008.
Gage # 4	2.08 (4.28.07)	-	Well bonded. This gage stopped working by 4.28.2007.
Gage # 5	1.97 (4.28.07)	-	The gage system seems solid. Probably inadequate gage installation because it debonded from the grid as a whole. This gage stopped working by 4.28.2007.



**Figure 5.5** Field strain gage measurements from the installation date to the removal date (modified after Berkheimer, 2007) (Layer #22).



**Figure 5.6** Tensile force distribution based on total strain values (Layer #22)

### 5.1.3 Layer # 19 (UX1400HS)

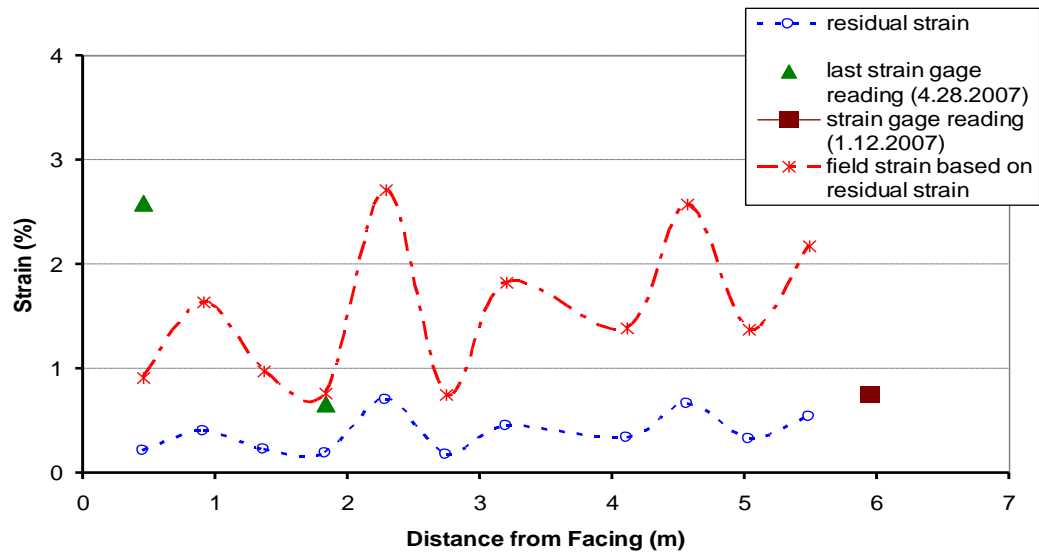
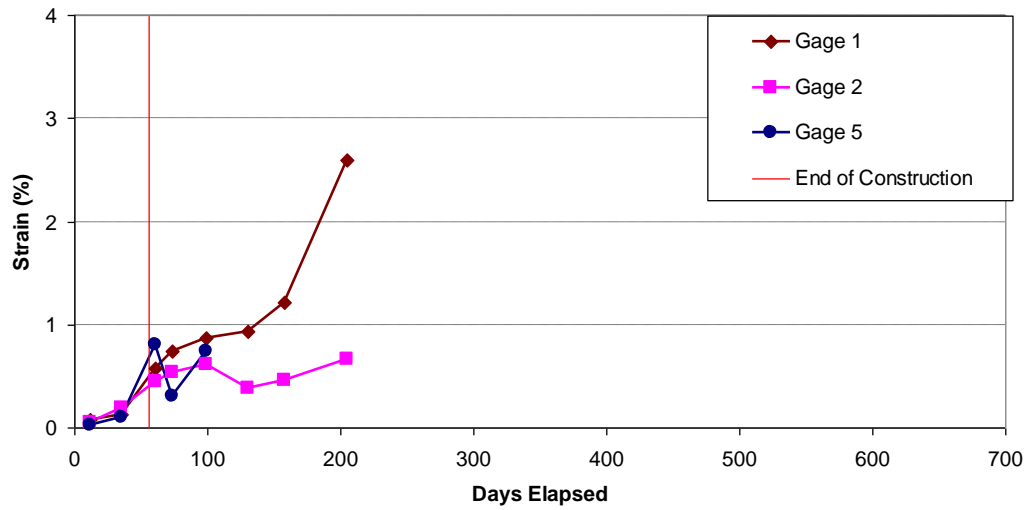


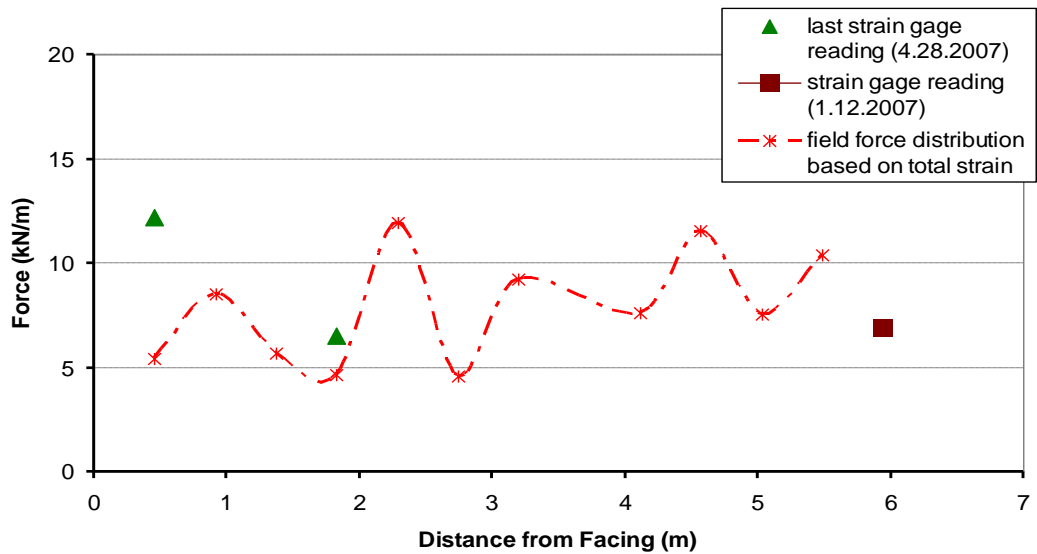
Figure 5.7 Strain distribution of the exhumed geogrid (Layer #19).

Table 5.3 Strain gage observed condition (Layer #19)

Layer 19	last reading	after excavation	Observation
Gage # 1	2.59 (4.28.07)	-	Well bonded. This gage stopped working by 4.28.2007.
Gage # 2	0.66 (4.28.07)	-	Well bonded. This gage stopped working by 4.28.2007.
Gage # 3	-	-	Has not worked since installation. Could be due to cable strain gage connection failure.
Gage # 4	-	-	Has not worked since installation. Could be due to cable strain gage connection failure.
Gage # 5	0.74 (1.12.07)	-	Well bonded. This gage stopped working by 1.12.2007.



**Figure 5.8** Field strain gage measurements from the installation date to the removal date (modified after Berkheimer, 2007) (Layer #19).



**Figure 5.9** Tensile force distribution based on total strain values (Layer #19)

### 5.1.4 Layer # 17 (UX1400HS)

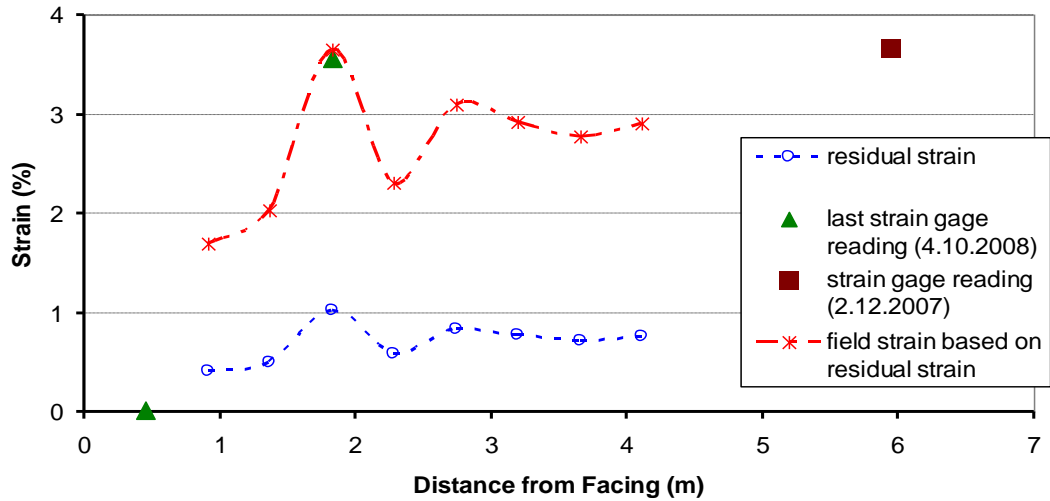
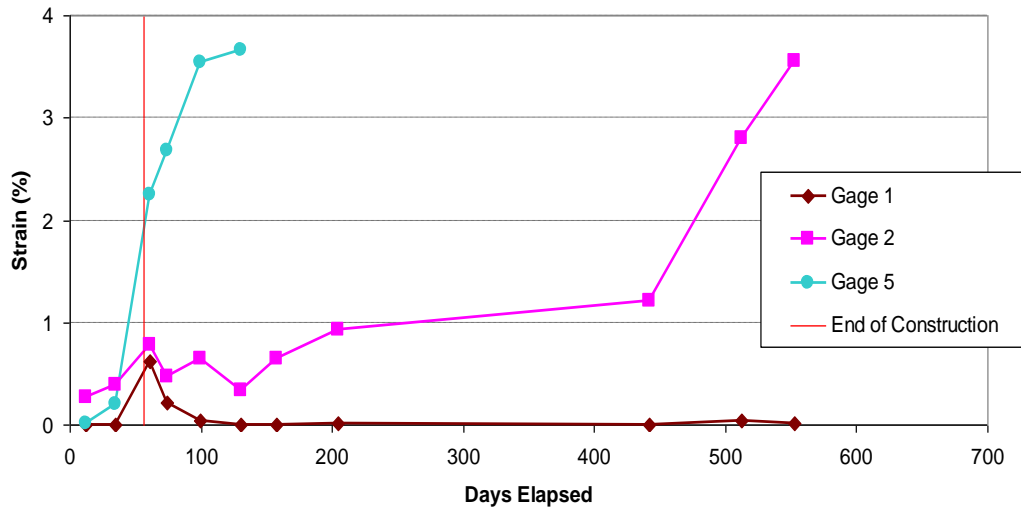


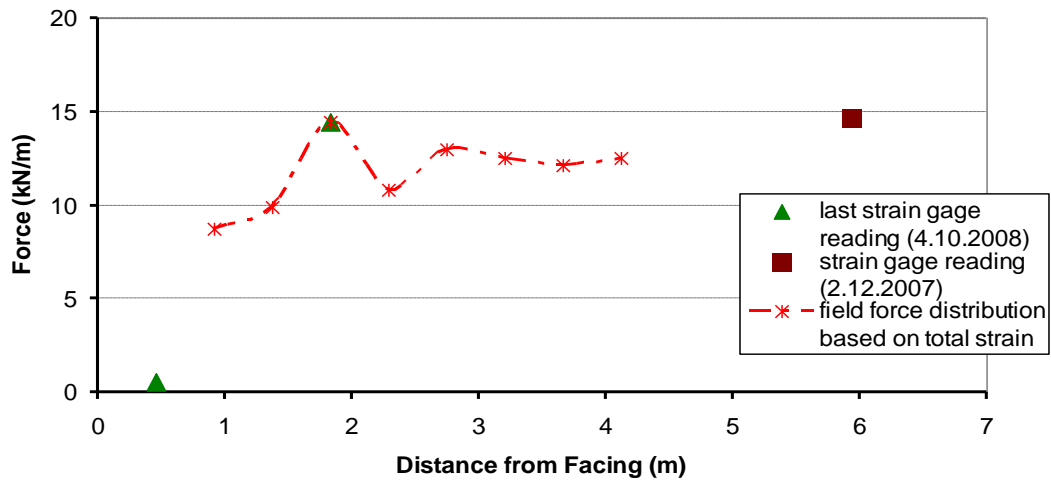
Figure 5.10 Strain distribution of the exhumed geogrid (Layer #17).

Table 5.4 Strain gage observed condition (Layer #17)

Layer 17	last reading	after excavation	Observation
Gage # 1	0.02 (4.10.08)	-	Gage not found, probably detached during removal of the geogrid. Last reading was taken on 4.10.2008.
Gage # 2	3.56 (4.10.08)	-	Gage not found, probably detached during removal of the geogrid. Last reading was taken on 4.10.2008.
Gage # 3	-	-	Gage not found, probably detached during removal of the geogrid.
Gage # 4	-	-	Gage not found, probably detached during removal of the geogrid.
Gage # 5	3.67 (1.12.07)	-	Gage not found, probably detached during removal of the geogrid. This gage stopped working by 1.12.2007.



**Figure 5.11** Field strain gage measurements from the installation date to the removal date (modified after Berkheimer, 2007) (Layer #17).



**Figure 5.12** Tensile force distribution based on total strain values (Layer #17)

### 5.1.5 Layer # 15 (UX1500HS)

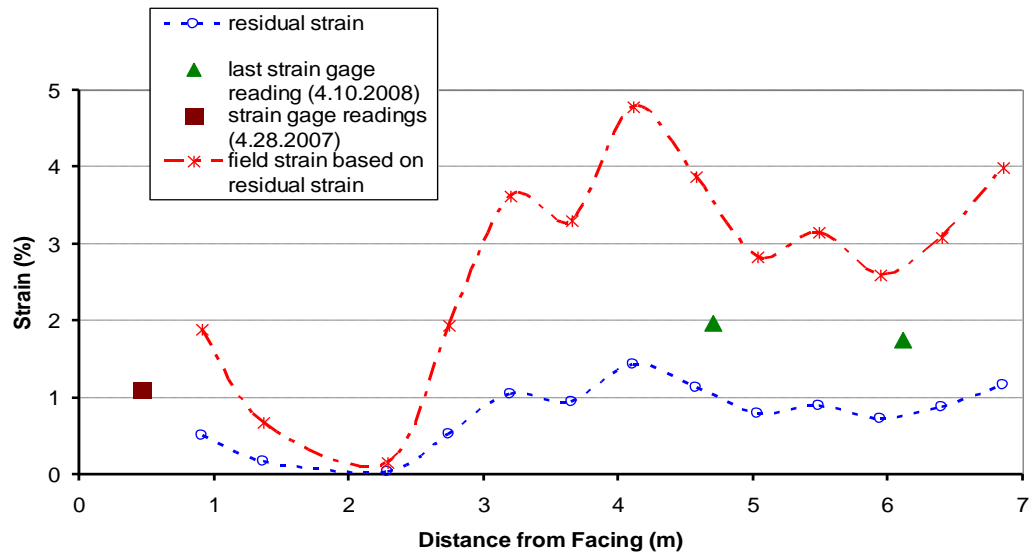


**Figure 5.13 Strain distribution of the exhumed geogrid (Layer #15).**

**Table 5.5 Strain gage observed condition (Layer #15)**

Layer 15	last reading	after excavation	Observation
Gage # 1	1.09 (4.28.07)	-	Well bonded. This gage stopped working by 4.28.2007.
Gage # 2	-	-	Has not worked since installation. Could be due to cable strain gage connection failure.
Gage # 3	-	-	Has not worked since installation. Could be due to cable strain gage connection failure.
Gage # 4	1.97 (4.10.08)	-	Gage not found, probably detached during removal of the geogrid. Last reading was taken on 4.10.2008.
Gage # 5	1.75 (4.10.08)	-	Well bonded. Last reading was taken on 4.10.2008.

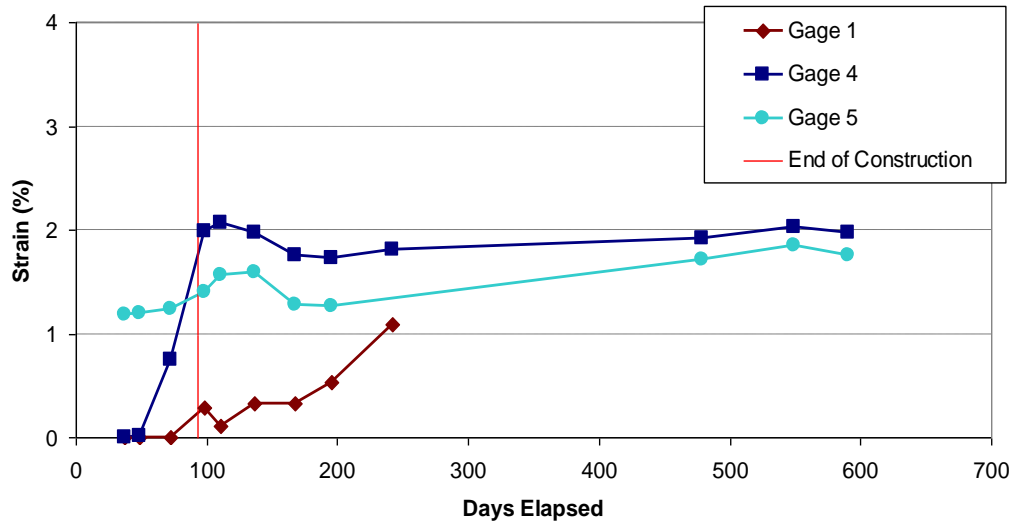


**Figure 5.14** Field strain gage measurements from the installation date to the removal date (modified after Berkheimer, 2007) (Layer #15).

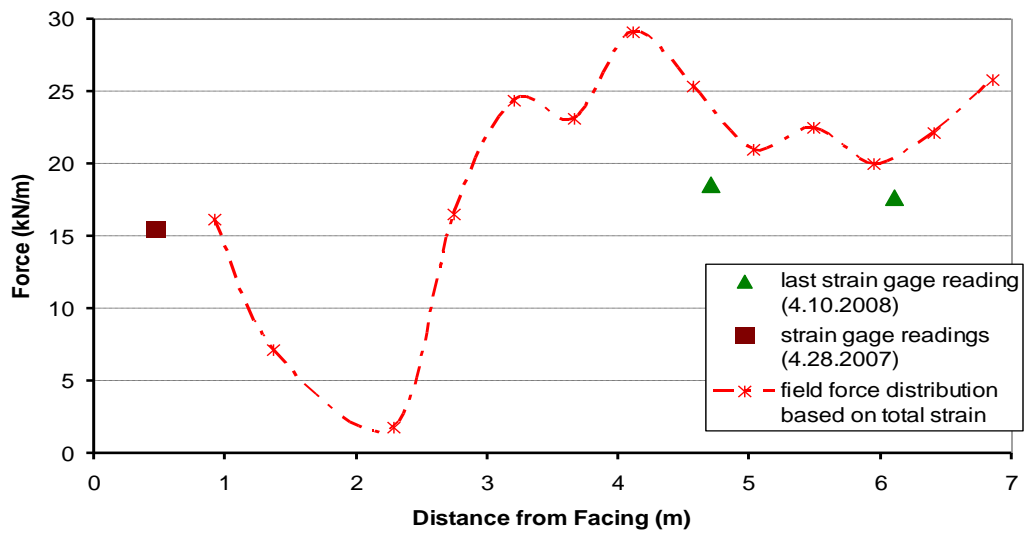


**Figure 5.15** Tensile force distribution based on total strain values (Layer #15)

### 5.1.6 Layer # 13 (UX1500HS)

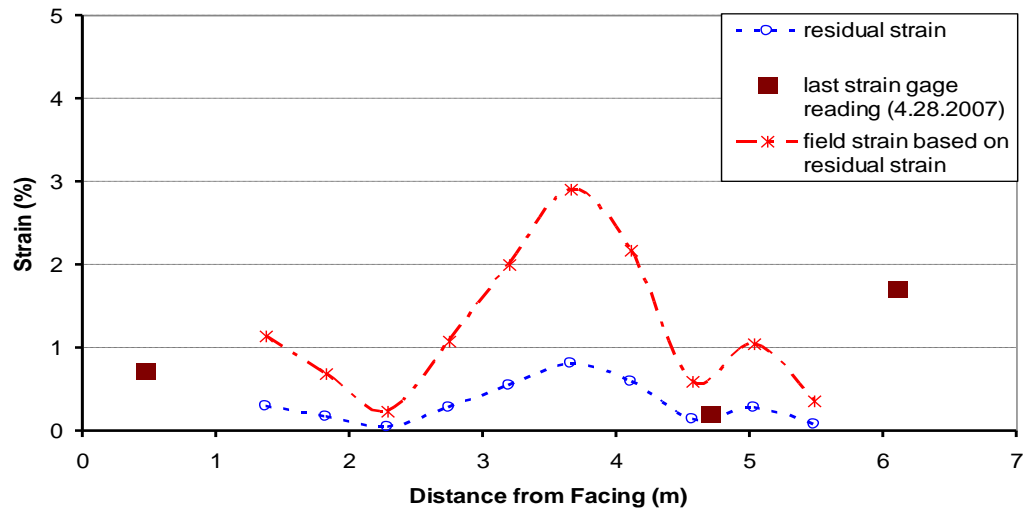
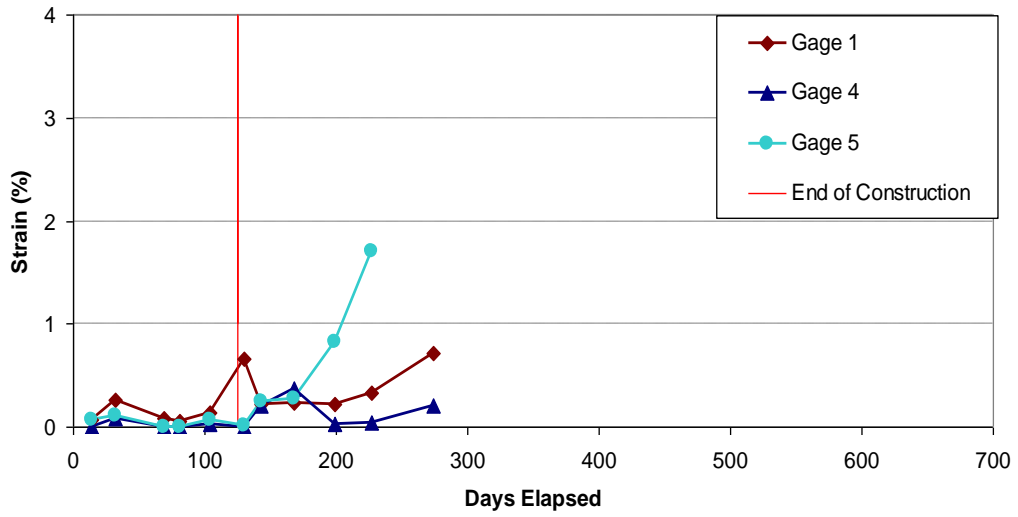


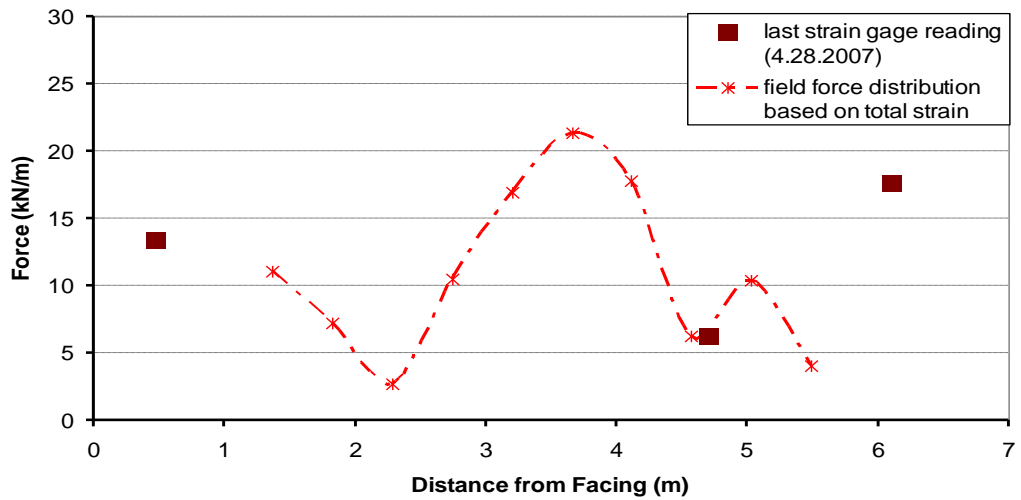
Figure 5.16 Strain distribution of the exhumed geogrid (Layer #13).

Table 5.6 Strain gage observed condition (Layer #13)

Layer 13	last reading	after excavation	Observation
Gage # 1	0.72 (4.28.07)	-	Gage not found, probably detached during removal of the geogrid. This gage stopped working by 4.28.2007.
Gage # 2	-	-	Has not worked since installation. The gage system seems solid. Probably inadequate gage installation because it debonded from the grid as a whole.
Gage # 3	-	-	Has not worked since installation. Could be due to cable strain gage connection failure.
Gage # 4	0.2 (4.28.07)	0.14	No particular damaged observed, the gage system seems solid and still working. Well bonded. This gage stopped working by 4.28.2007.
Gage # 5	1.7 (3.12.07)	-	Well bonded. This gage stopped working by 3.12.2007.



**Figure 5.17** Field strain gage measurements from the installation date to the removal date (modified after Berkheimer, 2007) (Layer #13).



**Figure 5.18** Tensile force distribution based on total strain values (Layer #13)

### 5.1.7 Layer # 11 (UX1500HS)

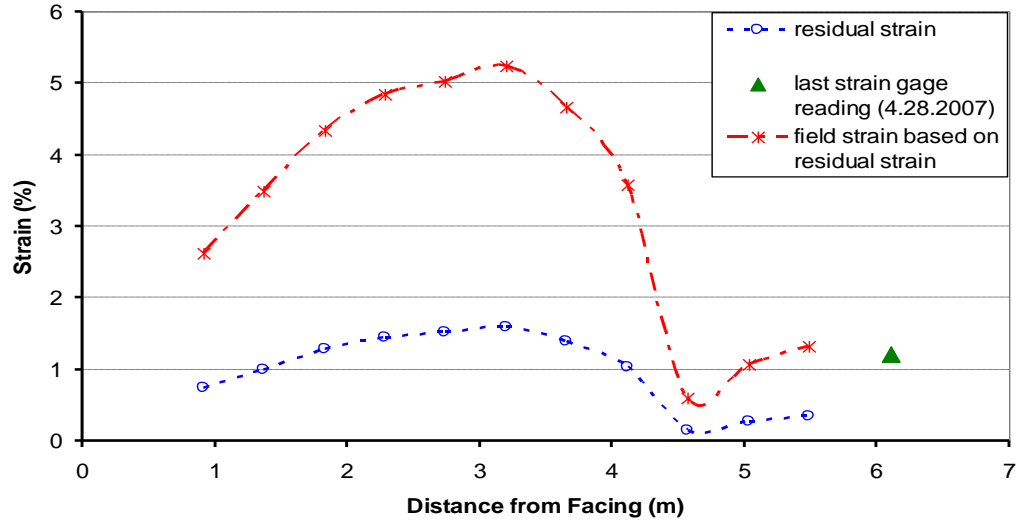
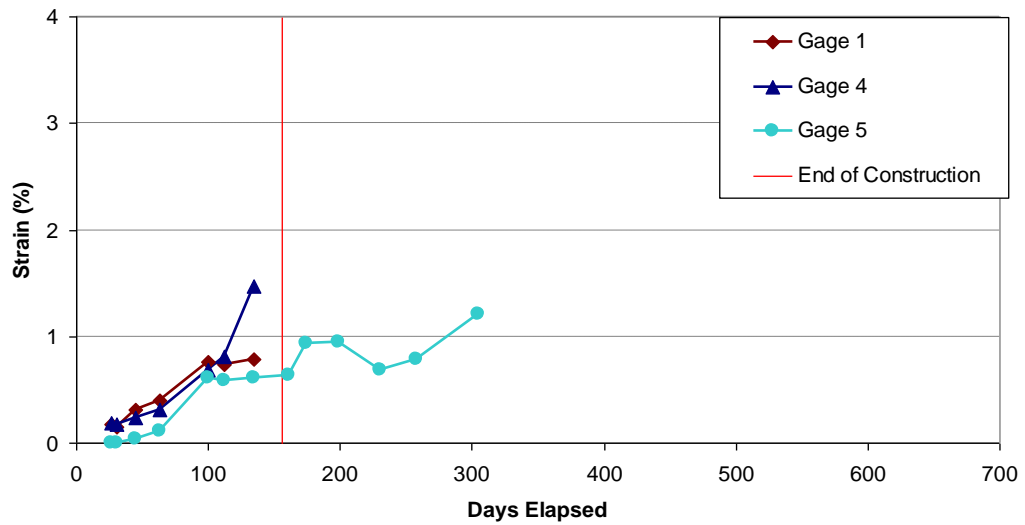


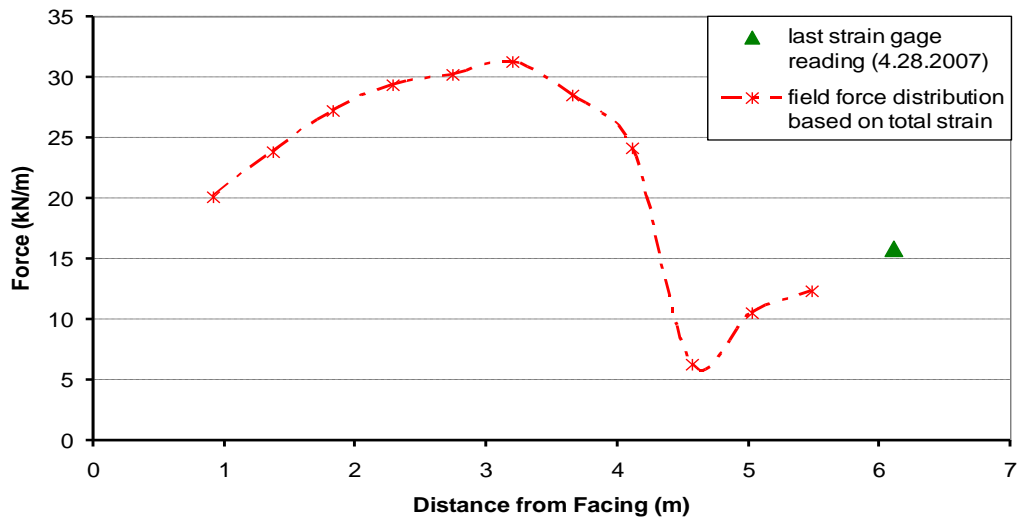
Figure 5.19 Strain distribution of the exhumed geogrid (Layer #11).

Table 5.7 Strain gage observed condition (Layer #11)

Layer 11	last reading	after excavation	Observation
Gage # 1	0.79 (11.9.06)	-	The gage system seems solid. Probably inadequate gage installation because it debonded from the grid as a whole. This gage stopped working by 11.9.2006
Gage # 2	-	-	Has not worked since installation. Could be due to cable strain gage connection failure.
Gage # 3	-	-	Has not worked since installation. Could be due to cable strain gage connection failure.
Gage # 4	1.48 (11.9.06)	-	Well bonded. This gage stopped working by 11.9.2006.
Gage # 5	1.21 (4.28.07)	-	Well bonded. This gage stopped working by 4.28.2007.



**Figure 5.20** Field strain gage measurements from the installation date to the removal date (modified after Berkheimer, 2007) (Layer #11).



**Figure 5.21** Tensile force distribution based on total strain values (Layer #11)

### 5.1.8 Layer # 10 (UX1600HS)

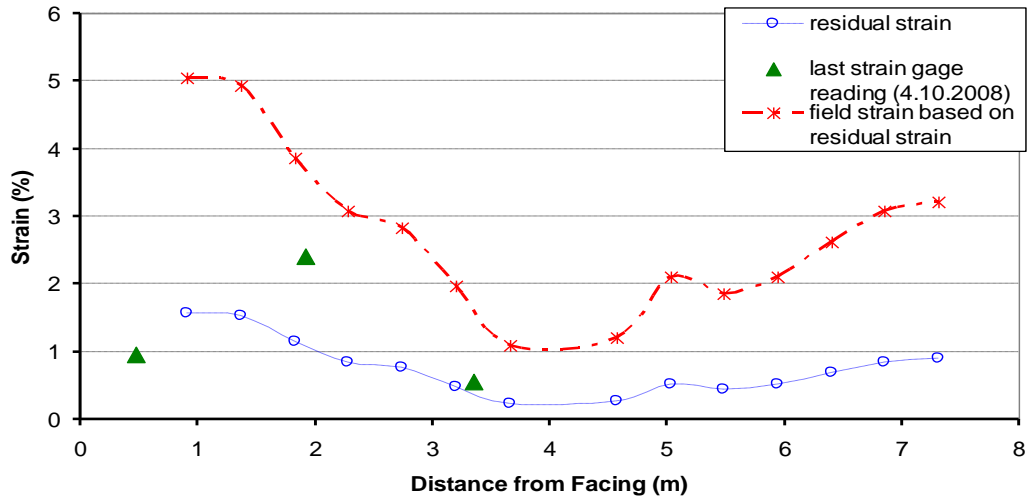
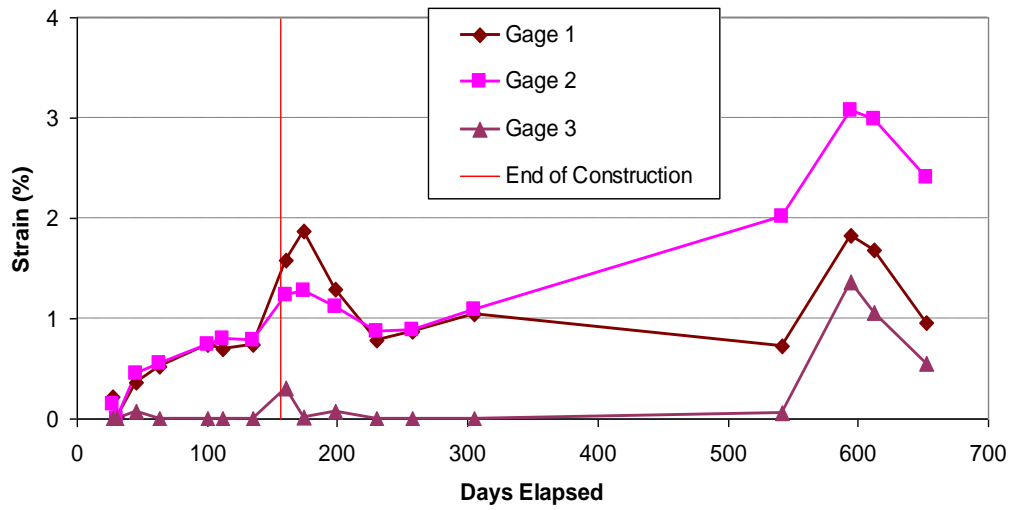


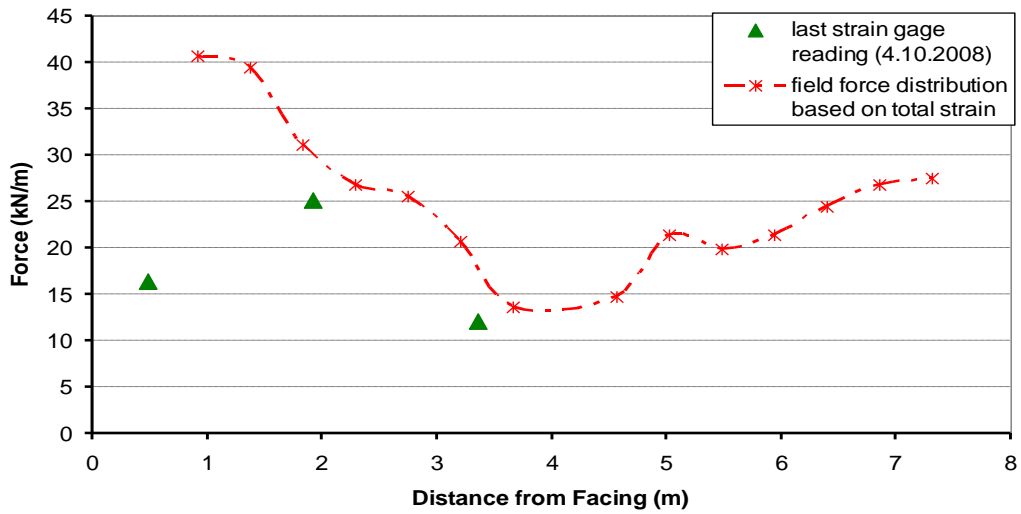
Figure 5.22 Strain distribution of the exhumed geogrid (Layer #10).

Table 5.8 Strain gage observed condition (Layer #10)

Layer 10	last reading	after excavation	Observation
Gage # 1	0.95 (4.10.08)	-1.69	No particular damaged observed, the gage system seems solid and still working. Well bonded. Last reading was taken on 4.10.2008.
Gage # 2	2.41 (4.10.08)	0.54	No particular damaged observed, the gage system seems solid and still working. Well bonded. Last reading was taken on 4.10.2008.
Gage # 3	0.56 (4.10.08)	-1.23	No particular damaged observed, the gage system seems solid and still working. Well bonded. Last reading was taken on 4.10.2008.
Gage # 4	0.00 (4.10.08)	0.00	Has not worked since installation. Could be due to cable strain gage connection failure.
Gage # 5	0.00 (4.10.08)	-	Has not worked since installation. Could be due to cable strain gage connection failure.



**Figure 5.23** Field strain gage measurements from the installation date to the removal date (modified after Berkheimer, 2007) (Layer #10).



**Figure 5.24** Tensile force distribution based on total strain values (Layer #10)

### 5.1.9 Layer # 8 (UX1600HS)

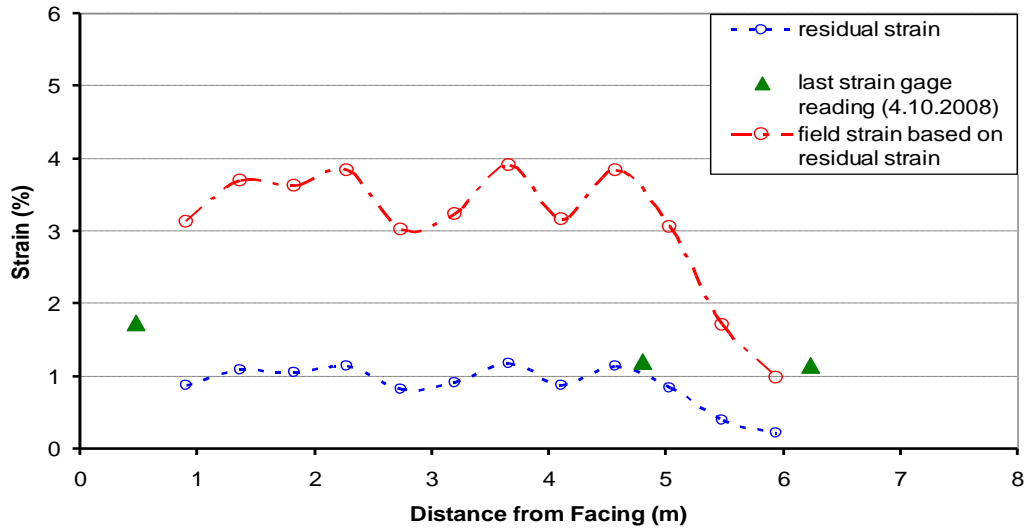
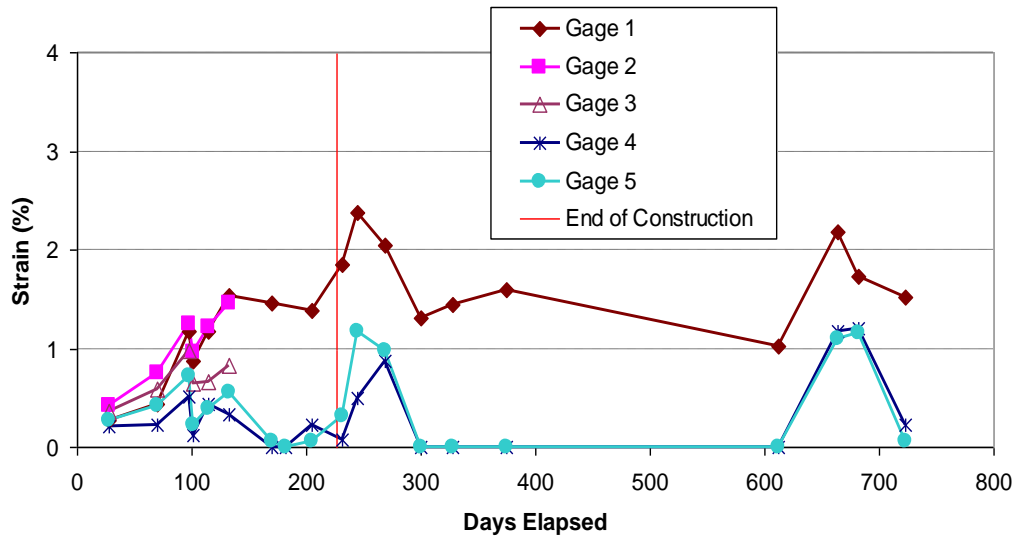


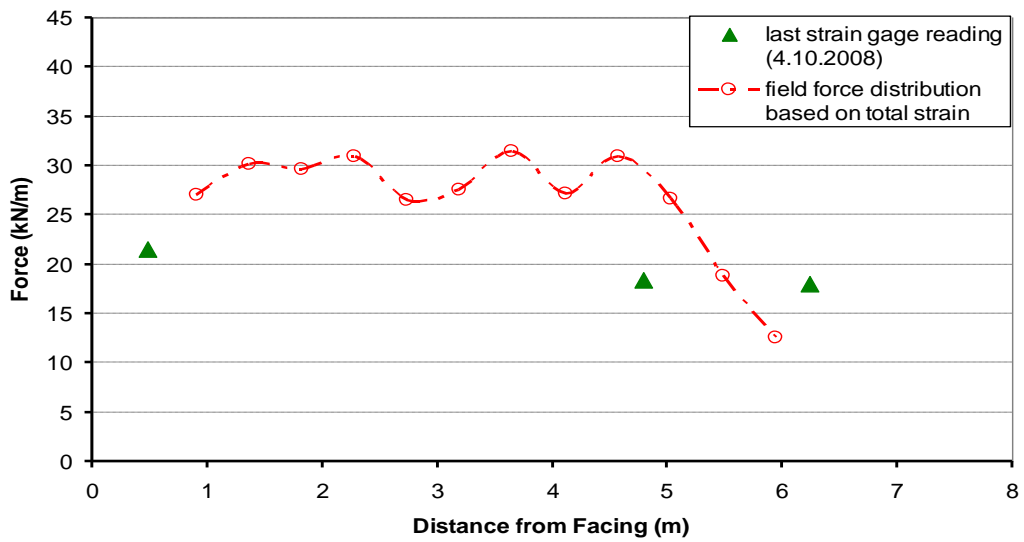
Figure 5.25 Strain distribution of the exhumed geogrid (Layer #8).

Table 5.9 Strain gage observed condition (Layer #8)

Layer 8	last reading	after excavation	Observation
Gage # 1	1.52 (4.10.08)	-1.33	No particular damaged observed, the gage system seems solid and still working. Well bonded. Last reading was taken on 4.10.2008.
Gage # 2	1.46 (8.29.06)	-	The gage system seems solid. Probably inadequate gage installation because it debonded from the grid as a whole. This gage stopped working by 8.29.2006.
Gage # 3	0.83 (8.29.06)	-	The gage system seems solid. Probably inadequate gage installation because it debonded from the grid as a whole. This gage stopped working by 8.29.2006.
Gage # 4	1.21 (4.10.08)	-4.57	No particular damaged observed, the gage system seems solid and still working. Well bonded. Last reading was taken on 4.10.2008.
Gage # 5	1.16 (4.10.08)	-5.35	No particular damaged observed, the gage system seems solid and still working. Well bonded. Last reading was taken on 4.10.2008.



**Figure 5.26** Field strain gage measurements from the installation date to the removal date (modified after Berkheimer, 2007) (Layer #8).



**Figure 5.27** Tensile force distribution based on total strain values (Layer #8)

### 5.1.10 Strain Gage Inspection

After exhumation, strain gages were inspected in the geotechnical laboratory at the University of Delaware. The observations made about the respective condition of these gages are summarized in Tables 5.1 through 5.9. One significant observation is that most of the strain gages were fully or partially debonded from the geogrid. Complete debonding of the gage from the geogrid is shown in Figure 5.28. Some gages appeared to be well-bonded and still functioning after exhumation (e.g. Figure 5.29). However, for many of the gages that appear to be “well-bonded”, there is a strong possibility that some of them were in fact partially debonded, yielding erroneous strain measurement results. Another gage failure mechanism that was observed was a break at connection of the electrical wire cable to the strain gage itself (e.g. Figure 5.30). There is no evidence that this connection failure happened during exhumation or due to the high stresses that were applied by the wall while the gage was embedded in the soil. All of these observations support the conclusion that attachment of strain gages to HDPE geogrids is an extremely challenging process, even under well-controlled laboratory conditions. This study points out general weaknesses (limitations) of strain gage geogrid attachments which, due to complete or partial debonding, may yield lower strains than actually existed.

As a general observation, most of the strain gages that were installed in the field at IRIB failed. Generally, the functioning gages yielded strains that indicate that the geogrids were stressed. The strain distribution among the exhumed geogrids indicates that the recorded strain gage data obtained from properly functioning gages was approximately in the range of the back calculated values following exhumation. This supports the back calculated values following measurements of the measured residual strains. It is unfortunate that many of the gages failed, mainly due to

debonding; however, exhumation and the strain calculation technique described in Chapter 4 have helped tremendously in complementing the missing data.



**Figure 5.28** Poorly-bonded strain gage completely debonded from the geogrid (layer #8, gage #3).



**Figure 5.29 Well-bonded strain gages (layer #10, gage #2).**



**Figure 5.30 Cable connection failure (layer #15, gage #2).**

## 5.2 Interpretation of the Results

Due to the excessive settlement that was observed at IRIB (i.e., settlement was such that 6 layers changed position from being above grade to below grade elevation) the location of the toe and the wall height, both defined by the grade elevation, varied as shown in Figure 2.3 (Chapter 2). The wall height just before the removal of the embankment as well as the analyzed strain and force distribution of the instrumented layers are presented in Figures 5.31 and 5.32, respectively. The strain and force distribution were presented in detail in Section 5.1 for each geogrid layer individually. Figures 5.31 and 5.32 provide a visual representation of the strains and force measured in each layer of geogrid along the height of the wall. It is noted that the strain distributions are in the range of about  $\pm 1.0\%$ . The strain values in Figure 5.31 are converted to tensile strength using the graphs presented in Chapter 4 and the associated results are presented in Figure 5.32 (i.e. tensile force distributions of the instrumented geogrid layers). The scale of y axis for individual layers is 0 to 5% strain for strain distribution and 0 to 40 kN/m for force distribution. The x axis represents the length of the geogrids (i.e. distance from the wall facing).

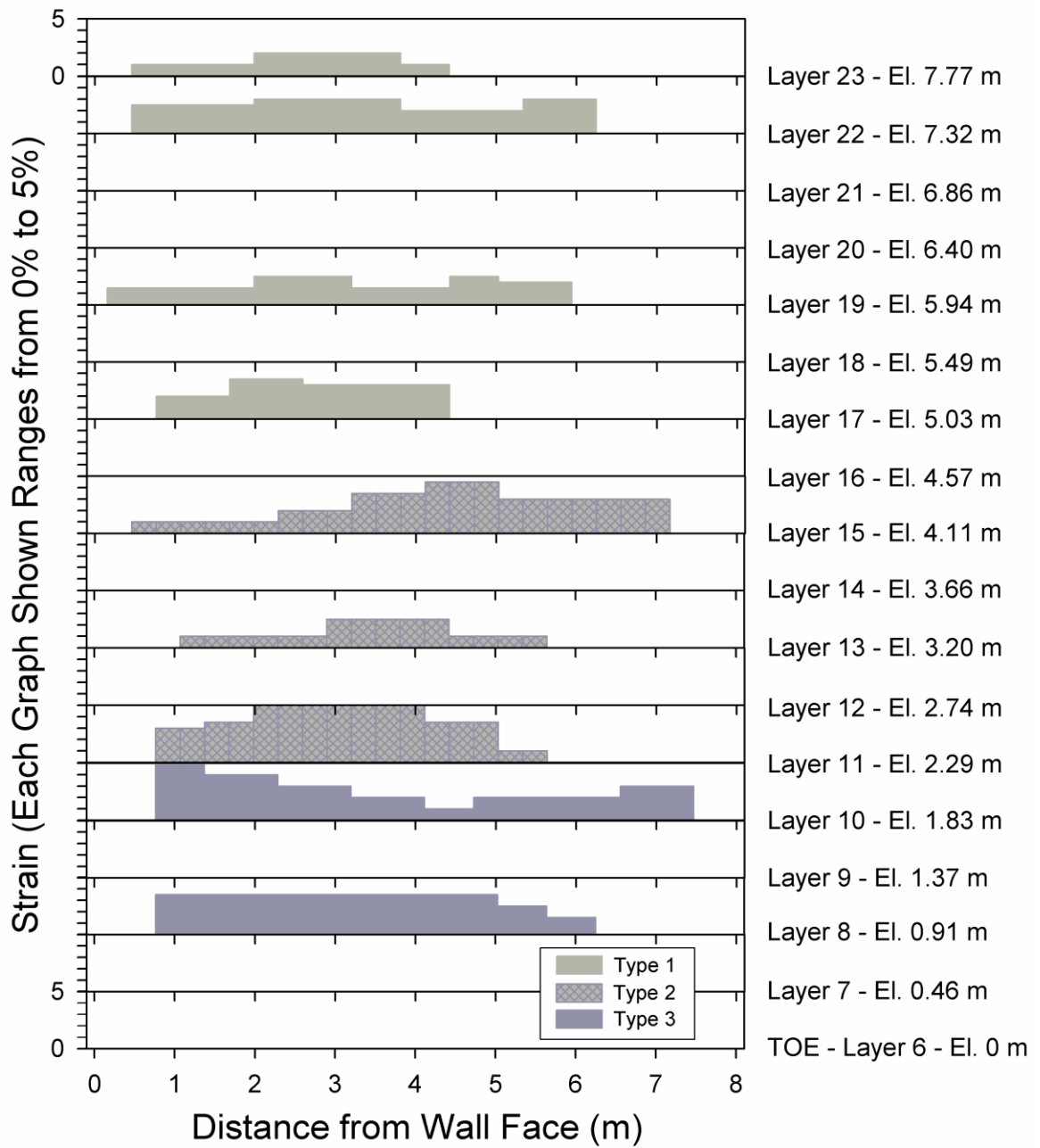


**Figure 5.31** Back-calculated total strain distributions on the instrumented geogrid layers.

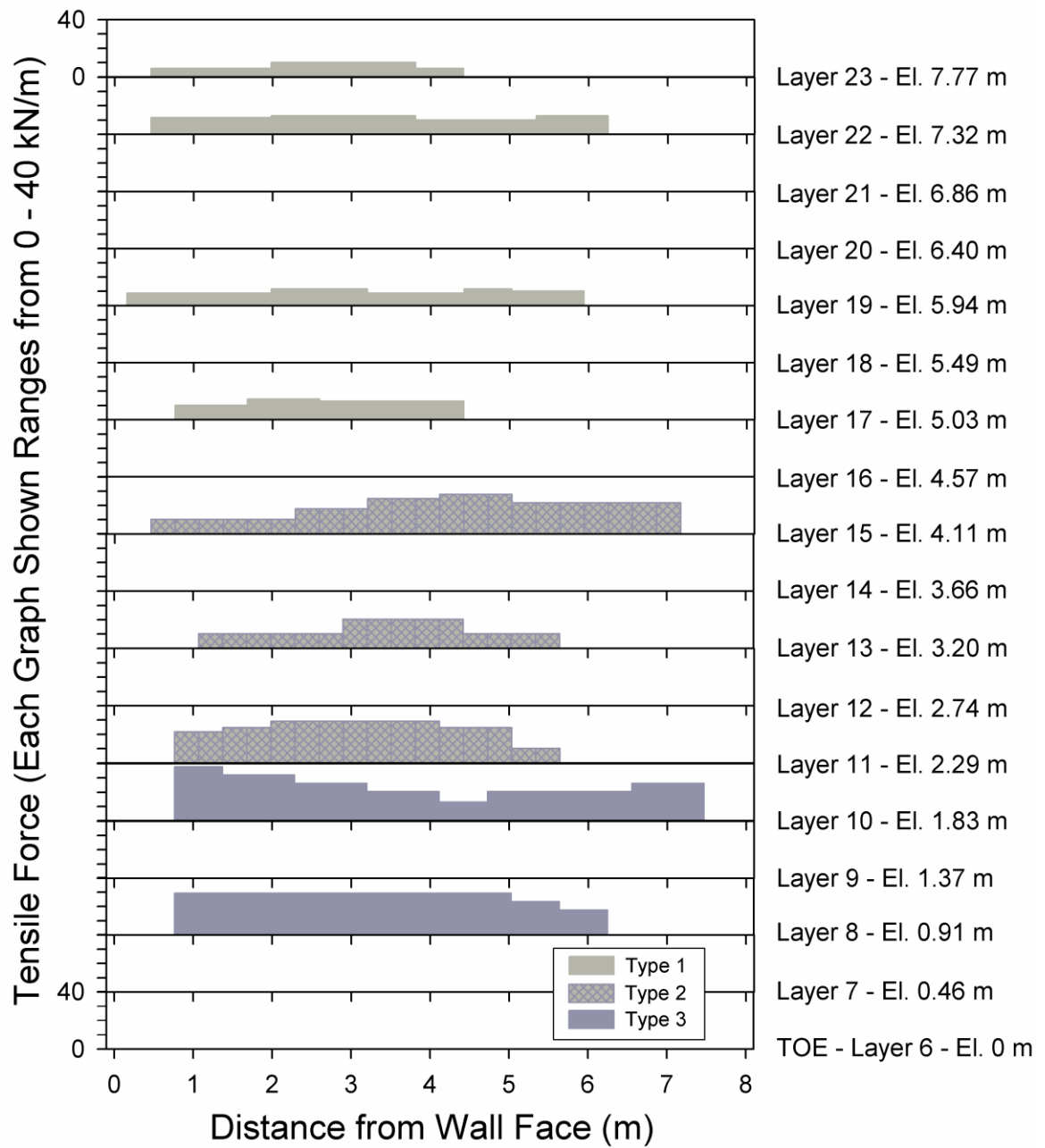


Figure 5.32 Tensile force distributions of the instrumented geogrid layers.

The measured  $T_{\max-i}$  (maximum tensile force for reinforcement layer  $i$ ) with depth can be normalized by dividing it by the measured  $\max (T_{\max})$  i.e.,  $[T_{\max-i} / \max (T_{\max})]$ . Similarly the elevation ( $Z$ ) is normalized by dividing it by the wall height ( $H$ ). The measured  $\max (T_{\max})$  is in units of kN/m and  $H$  is in units of meters. The resulting normalized values of  $T_{\max}$  as a function of the resulting normalized elevation values ( $Z/H$ ) are presented in Figure 5.33. This non-dimensional approach relates the force in reinforcement layer  $i$  to the maximum force that is mobilized amongst all the layers. This measured normalized distribution is approximated by a line as shown in Figure 5.34.

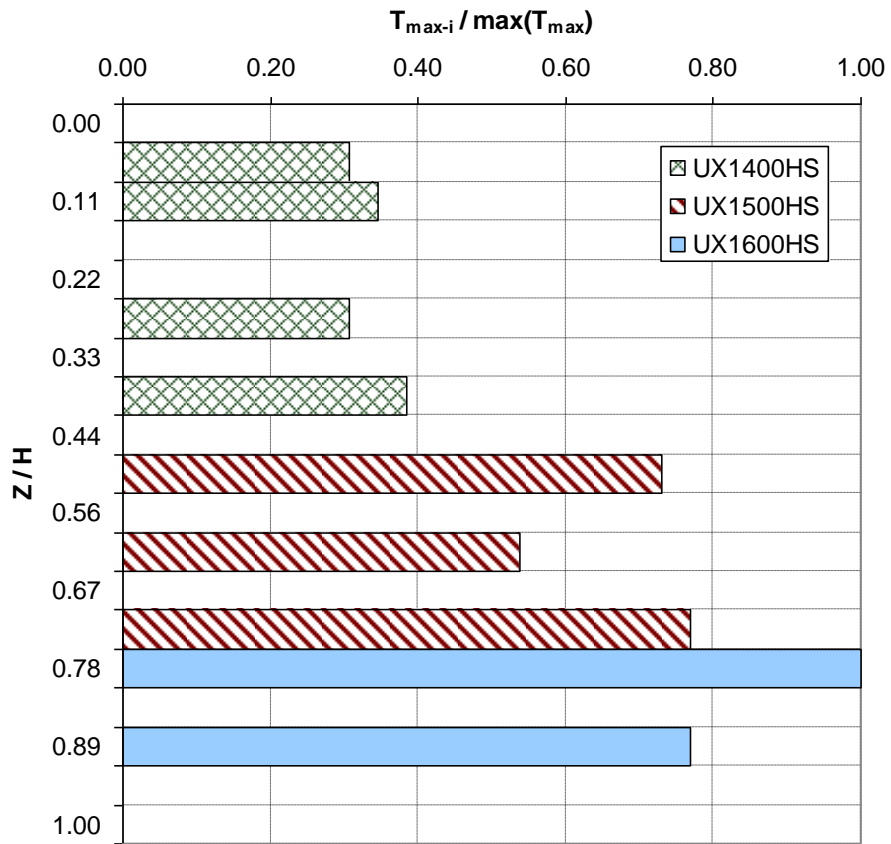
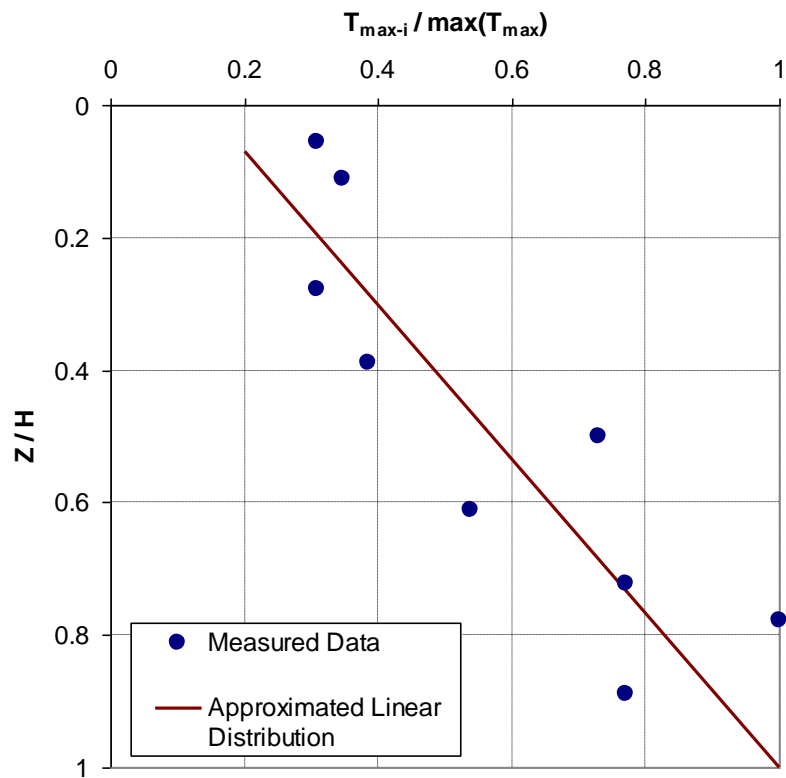


Figure 5.33 Measured normalized  $T_{\max}$  for each layer.



**Figure 5.34** Distribution of the measured data and the approximated linear distribution.

Product properties for the three Tensar structural geogrids used at IRIB are presented in Table 5.10. To check the internal stability of the wall, the maximum tensile forces of each instrumented geogrid layer were determined, and the resulting factor of safety values on geogrid strengths are presented in Table 5.11. Assuming Z notation (i.e. assuming the zero elevation starts from the crest) up to elevation 4.11 m, where the type of the geogrid changed from UX1400HS to UX1500 HS, the factor of

safety values are higher than 1.5. At increased depths from the crest (lower in the wall), the factor of safety drops to approximately 1.4.

**Table 5.10 Tensar structural geogrid product properties (product specification Tensar structural geogrid 2007)**

Structural Geogrid	$T_{ult}$ [kN/m]	$RF_{ID}$	$RF_{CR}$	$RF_D$	$T_{LTDS}$ [kN/m]
UX1400HS	70	1.05	2.60	1.00	26
UX1500HS	114	1.05	2.60	1.00	42
UX1600HS	144	1.05	2.60	1.00	53
$T_{ult}$ = Ultimate Tensile Strength					
$RF_{ID}$ = Minimum Reduction Factor for Installation Damage					
$RF_{CR}$ = Reduction Factor for Creep for 120-year Design Life					
$RF_D$ = Minimum Reduction Factor for Durability					
$T_{LTDS}$ = Long Term Design Strength (for 120-year Design Life)					

**Table 5.11 Calculated Factor of safety on geogrid strength**

Layers	H (m)	Z (m)	Structural Geogrid	T <sub>ult</sub> [kN/m]	RF <sub>ID</sub>	RF <sub>CR</sub>	RF <sub>D</sub>	T <sub>LTDS</sub> [kN/m]	Measured T <sub>max-i</sub> [kN/m]	F <sub>s</sub> = T <sub>LTDS</sub> / T <sub>max-i</sub>
Crest	8.23	0.00	N/A	N/A	N/A	N/A	N/A	N/A	N/A	N/A
23	7.77	0.46	UX1400HS	70	1.05	2.60	1.00	26	12	2.20
22	7.32	0.91	UX1400HS	70	1.05	2.60	1.00	26	13	1.96
21	6.86	1.37	UX1400HS	70	1.05	2.60	1.00	26	N/A	N/A
20	6.40	1.83	UX1400HS	70	1.05	2.60	1.00	26	N/A	N/A
19	5.94	2.29	UX1400HS	70	1.05	2.60	1.00	26	12	2.20
18	5.49	2.74	UX1400HS	70	1.05	2.60	1.00	26	N/A	N/A
17	5.03	3.20	UX1400HS	70	1.05	2.60	1.00	26	15	1.76
16	4.57	3.66	UX1400HS	70	1.05	2.60	1.00	26	N/A	N/A
15	4.11	4.11	UX1500HS	114	1.05	2.60	1.00	42	28	1.51
14	3.66	4.57	UX1500HS	114	1.05	2.60	1.00	42	N/A	N/A
13	3.20	5.03	UX1500HS	114	1.05	2.60	1.00	42	20	2.04
12	2.74	5.49	UX1500HS	114	1.05	2.60	1.00	42	N/A	N/A
11	2.29	5.94	UX1500HS	114	1.05	2.60	1.00	42	29	1.43
10	1.83	6.40	UX1600HS	144	1.05	2.60	1.00	53	38	1.39
9	1.37	6.86	UX1600HS	144	1.05	2.60	1.00	53	N/A	N/A
8	0.91	7.32	UX1600HS	144	1.05	2.60	1.00	53	29	1.81
7	0.46	7.77	UX1600HS	144	1.05	2.60	1.00	53	N/A	N/A
Toe	0.00	8.23	N/A	N/A	N/A	N/A	N/A	N/A	N/A	N/A

## **Chapter 6**

### **CONCLUSIONS AND RECOMMENDATIONS**

DelDOT has determined that the bridge on Delaware Route 1 over the Indian River Inlet in Sussex County, Delaware needs to be replaced. Approach embankments for the replacement bridge were constructed and were supported on either side by MSE walls. Because of the poor foundation soils, an extensive instrumentation program consisting of inclinometers, settlement plates, piezometers and wall targets was used to monitor the performance of the embankments during and after construction. The MSE Wall 1 at Station 289+00 was also instrumented by the University of Delaware with strain gages, to monitor the strains in the geogrid reinforcement.

Construction at Station 289+00 started on 02/20/2006 and it was completed on 12/01/2006. Due to significantly higher settlements than expected, DelDOT decided to remove the embankments on 04/20/2008. The deconstruction process was completed in three months. This deconstruction process provided an opportunity to exhume the strain gaged geogrid layers.

The objectives of this research were: (1) to examine directly the status of the strain gages that were attached to the geogrid and to verify the reliability of their output, (2) to develop a procedure to assess the in-situ strains in the exhumed geogrid based on its plastic deformation after exhumation, and (3) to assess the force in the geogrid layers and verify whether there was excessive stress.

## 6.1 Conclusions

Strain gages were installed on geogrid panels and monitored by Scott A. Berkheimer (2007) at the IRIB south abutment Wall 1. The Author continued monitoring the output of these strain gages following Berkheimer's graduation until the removal of the embankment. The embankment removal created the opportunity to exhume geogrid panels, most notably those with strain gages. The strain gages were examined visually to verify their state. The geogrid panels were examined in the lab to assess their residual or plastic strain. The length changes of the exhumed geogrids were measured and converted to the corresponding strain values. These strains are the residual strains (the strains after relaxation). A test method (simulating field conditions) was developed to verify the in-situ strains and loads. The assessed strains for all three different types of geogrid exhibit practically the same total strain versus residual strain behavior. However, this does not imply that the corresponding field loads exhibit the same behavior, as the load carrying capacity of the geogrid at a given strain is related to the stiffness of the material, implying that the same strain will likely correspond to different loads. Using calibration charts, the residual strain values were then converted to strain and load corresponding to the values while in-service (in-situ total strains and forces).

In general, most of the strain gages failed. The main mode of failure was gage debonding. The functioning gages yielded some strain values. Some of the functioning strain gages were partially debonded, thus yielding lower strains than the actual values. Fully bonded strain gages yielded strains that were approximately within the range of the assessed values following exhumation. Indirectly, this supports the procedure used to assess strain values following the measured residual strains. The

assessed maximum strains approximately varied from 3% to 5%, a rather similar value for all layers.

The maximum tensile force in each instrumented geogrid panel was determined. Subsequently, the resulting factor of safety on the strength of each panel, considering the long-term allowable strength, was directly calculated. In the upper portion of the wall, where the types of the geogrid were UX1400HS and UX1500 HS, the factor of safety values were higher than 1.5. In the lower portion of the wall, the factor of safety was approximately 1.4.

## **6.2 Recommendations**

It is recommended that more accurate lab simulation of the time-history loading of the geogrid panels in the field be done. It is believed that the simulation used in this work (i.e., about 1 month of loading and unloading versus about 2 years in the field) is quite accurate since loads within the long-term strength do not overstress the geogrids. That is, the creep component in geogrids that are not overstressed is rather small and therefore, the lab simulation could be done at an accelerated rate. However, it would be interesting to create a calibration curve for various simulated time-histories and identify the threshold when it becomes significant. Such a study will have to be conducted over a period of several years. The insight from such a study can be instructive.

## REFERENCES

- Bay, James, Loren Anderson, Aaron Budge, and Mark Goodsell. (2003). Instrumentation and Installation Scheme of a Mechanically Stabilized Earth Wall on I-15 with Results of Wall and Foundation Behavior. Utah State University, Logan, UT.
- Koerner, R.M. (2005). Designing with Geosynthetics, Fifth Ed., Pearson Prentice Hall, Upper Saddle River, NJ.
- Leshchinsky, D. and Fowler, J. (1990). Laboratory Measurement of Load-Elongation Relationship of High-Strength Geotextiles. Geotextiles and Geomembranes, 9(2), 145-164.
- Slope Indicator. (2006a). Digitilt Inclinometer Probe. Mukilteo, WA: Durham Geo Slope Indicator.
- Slope Indicator. (2006b). Vibrating Wire Piezometer. Mukilteo, WA: Durham Geo Slope Indicator.
- Sluimer, G. and Risseuw, P. (1982). A Strain-Gauge Technique for Measuring Deformations in Geotextiles. Proc., Second International Conference on Geotextiles, Las Vegas, USA, 835 – 838.
- Soong, T.-Y. and Koerner, R. M. (1998). Laboratory Study of HDPE Geomembrane Waves. Proceedings 6 ICG (pp.301-306). Atlanta: IFAI.
- Thomas, R. W. and Verschoor, K. L. (1990). Thermal Analysis of Nonwoven Polyester Geotextiles. Geosynthetics: Microstructure and Performance, ASTM STP 1076, J. D. Peggs, Ed., American Society for Testing and Materials, Philadelphia, pp. 4-16.
- Won, M-S. and Y-S Kim. (2006). Application of strain gauges to measure nonwoven geotextile deformation in reinforced soil wall. In J. Kuwano and J. Koseki (Eds.), Proceedings of the 8<sup>th</sup> International Conference on Geosynthetics (pp. 945-948). Rotterdam: Millpress.

# Delaware Center for Transportation University of Delaware Newark, Delaware 19716

## **AN EQUAL OPPORTUNITY/AFFIRMATIVE ACTION EMPLOYER**

The University of Delaware is committed to assuring equal opportunity to all persons and does not discriminate on the basis of race, creed, color, gender, age, religion, national origin, veteran or handicapped status, or sexual orientation in its educational programs, activities, admissions or employment practices as required by Title IX of the Educational Amendments of 1972, Section 504 of the Rehabilitation Act of 1973, Title VII of the Civil Rights Act of 1964, and other applicable statutes. Inquiries concerning Section 504 compliance and information regarding campus accessibility should be referred to the Americans with Disabilities Act (ADA) Coordinator, 831-4643, located at 413 Academy Street. Inquiries concerning Title VII and Title IX should be referred to the Office of the Assistant Vice President for Affirmative Action, 831-8735, located at 124 Hullihen Hall.

